Dynamics of vortex fronts in type II superconductors

Chiara Baggio

In the front cover:
image from a photo taken by Alvise De Col, isola di Caprera, Italy.

Dynamics of vortex fronts in type II superconductors

proefschrift

ter verkrijging van
de graad van Doctor aan de Universiteit Leiden,
op gezag van de Rector Magnificus Dr. D. D. Breimer,
hoogleraar in de faculteit der Wiskunde en
Natuurwetenschappen en die der Geneeskunde,
volgens besluit van het College voor Promoties
te verdedigen op dinsdag 22 November 2005
te klokke 14.15 uur

door

Chiara Baggio

geboren te Bassano del Grappa (Italië) in 1978

Promotor:	Prof. dr. ir. W. van Saarloos
Referent:	Prof. dr. P. H. Kes
Overige leden:	Prof. dr. J. Aarts
	Prof. dr. A. Achúcarro
	Prof. dr. C. W. J. Beenakker
	dr. R. J. Wijngaarden (Vrije Universiteit Amsterdam)

ad Alvise

Contents

Chapter 1

Introduction

1.1 Perspective

Superconductors are materials characterized not only by a perfect conductance below a critical temperature, as was first discovered by Kamerlingh Onnes in 1911 in Leiden, but also by the diamagnetic property of expelling an external magnetic field, the so called Meissner-Ochsenfeld effect [1]. In type II superconductors for external fields between the two temperature-dependent values H_{c1} and H_{c2}, flux penetration occurs in the form of quantized flux lines or vortices, with a quantum flux $\phi_0 = hc/2e$ [2]. These are elastic and interacting objects, whose fascinating physics has attracted many scientists in the last decades. After the discovery of the high-T_c superconductors, the richness of the phenomenology of vortices, both in their static and dynamical properties, has led to the introduction of the new concept of "vortex matter" as a new state of matter [3]. From the technological point of view, the intense research activity on type II superconductors was also stimulated and motivated by the fact that, when vortices move they induce dissipation, due to the normal nature of the cores, and therefore the superconducting property of perfect conductivity is lost.

The properties of type II superconductors have been studied extensively in the past decades. The interplay of pinning and fluctuation effects gives

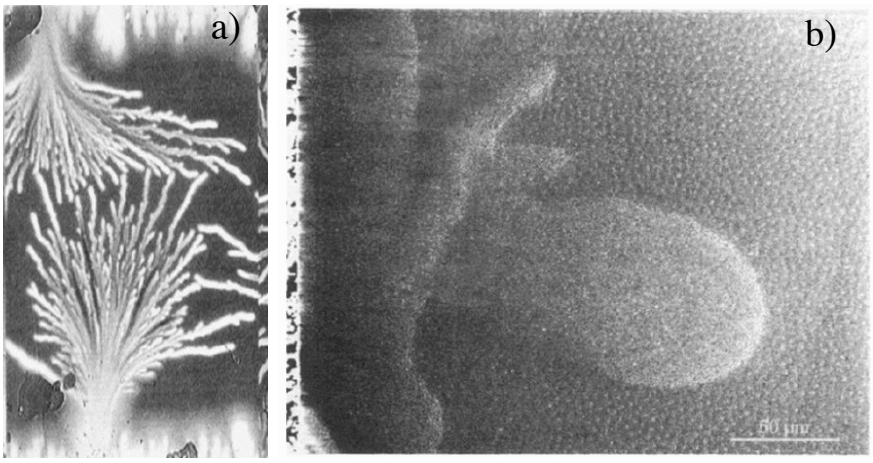

Figure 1.1: Examples of vortex patterns in type II superconductors. a) On the left dendritic patterns of vortices with branchlike structures in a Nb film of 0.5 μm. The sample is at a temperature of 5.97 K and the external field is 135 Oe. After [10]. b) On the right droplet-like patterns observed with the decoration technique in a $NbSe_2$ single crystal at 5 mT. Inside the droplet the density of vortices is higher, whereas in the outer region, where vortices are more visible, the density is lower. After [17, 18].

rise to a rich variety of phases whose main features are by now rather well understood [3–6]. In comparison with the equilibrium state, however, our understanding of the dynamics of vortices, and, in particular, of their collective behavior is less well developed.

Recently, experiments with magneto-optical techniques on flux penetration in thin films have revealed the formation of a wide variety of instabilities. When vortices penetrate from the edge of a superconductor, the pinning, due to material imperfections, leads, in a idealised situation, to a flux gradient and thus to a linear profile for the magnetic induction inside the sample. This state (corresponding to the conventional picture of a so-called Bean state [7]), is only marginally stable. In reality, flux penetration can occur in the form of a more complex distribution. Beyond phenomena such as avalanches and flux jumps [8, 9], recent experiments have revealed interest-

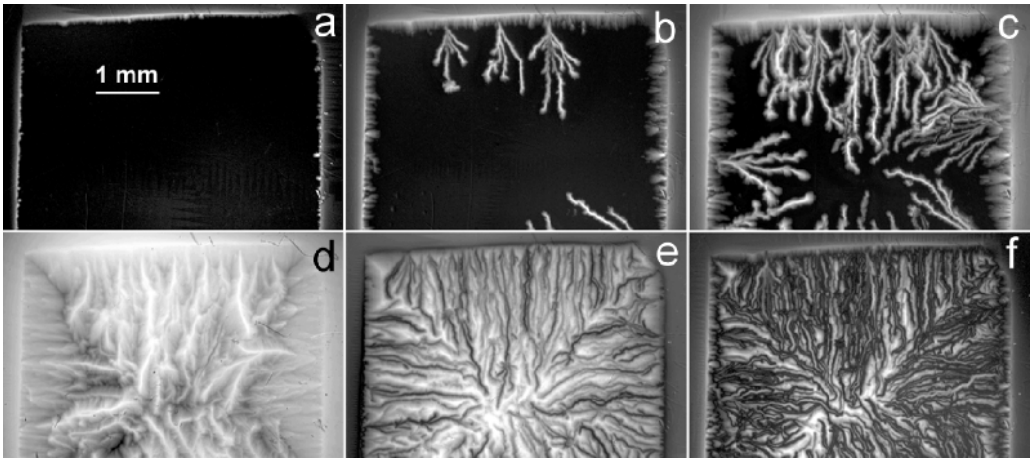

Figure 1.2: Images of flux penetration (bright areas) into a superconducting state (dark areas) at 5 K in a MgB_2 film of 0.4 μm. From a) to d): images taken at an applied field of 3.4 mT, 8.5 mT, 17 mT, and 60 mT, respectively. From e) to f) Images taken at 21 mT and 0 mT during the field reduction. The one-dimensional structures of vortices at the initial stage develop into dendritic patterns with a more complex morphology. After [11].

ing out-of-equilibrium patterns involving the formation of ramified dendritic or finger-shaped domains of vortices, both in low-T_c materials, like in Nb and MgB_2 thin films [10–15], and high-T_c materials, like $YBa_2Cu_3O_{7-\delta}$ [16]. Examples of patterns presenting the morphology of dendrites, are represented in Fig. 1.1(a) and Fig. 1.2 [10,17,18]. Figure 1.1(a), which refers to experiments performed with magneto-optical techniques in a Nb thin film, represents the magnetic flux distribution of the sample at a temperature of 5.97 K; the brightness corresponds to the different density of magnetic flux. The same type of patterns could be reproduced in MgB_2, as one can see in Fig. 1.2, for different magnetic fields. At lower temperatures the magnetic flux penetrates instead through the nucleation of one-dimensional structures (fingers of vortices) that propagate with a very well defined shape as we will show later in this Chapter, in Sec. 1.8.

Generally, it is accepted now that these patterns, which propagate ex-

tremely fast and are found only in a certain temperature window, are instabilities of thermo-magnetic origin, due to the local overheating induced by the vortex dynamics, but properties like their characteristic shape or the velocity of propagation are still poorly understood [8, 9, 19–21].

Likewise, flux penetration in the form of droplets have been observed in $NbSe_2$ single crystals [17, 18]. Figure 1.1(b) illustrates a droplet-like pattern with a higher density of vortices inside and a lower density in the region outside, where individual vortices are more visible. One can notice the high degree of order of the vortex lattice inside the droplet and the sharp transition zone between the two regions of vortices.

Furthermore, an other type of instability was observed at the boundaries between flux and anti-flux in $YBa_2Cu_3O_{7-\delta}$ samples. By applying an external field of opposite sign to a remanent state, for a certain temperature interval, the front between vortices and antivortices exhibits a "turbulent" behavior [22–25], as we will see at the end of this Chapter. The mechanism that underlies this phenomenon has been object of dicussions in the literature; from this debate, the question about the relevance of the coupling of the vortex mobility with the temperature for the instability has emerged [26–28]. Several attempts to describe the phenomenon have been made, but there are still open issues to investigate in order to give a clear picture of such a behavior.

A first question on all these out-of-equilibrium patterns in type II superconductors is which is the mechanism that generates the instability and leads to the final distribution of nonuniform magnetic flux. Moreover, a second issue is understanding the features of these structures, like their characteristic shape and size. In this thesis we will focus on these topics, by addressing two examples of propagating fronts between phases of different densities of vortices. As we will discuss, these types of phenomena present analogies with interfacial instabilities in other physical systems like, for example, dendrites in crystal growth or fingering at the interface between two liquids of different viscosity [29–31]. These similarities have been well known

for the case of superconductor-normal interfaces in type I superconductors, but the connection between these patterns and the ones observed in type II superconductors has not been explored in depth. This is partly because dealing with this analogy turns out to be a quite delicate issue. Firstly, the systems with which we deal are strongly out-of-equilibrium, due to the repulsive long-range interactions between the flux lines, expecially in thin films; thus equilibrium properties, like the surface tension at the interface between two states, are not properly defined. Secondly, systems of vortices are characterised by properties which are not standard: their dynamics is strongly nonlinear, and temperature dependent, and, moreover, inhomogeneities due to pinning defects and temperature fluctuations play an important role.

On the other hand, some techniques that are usually employed in the analysis of front propagation are useful tools to investigate these instabilities, like, for example, the description of the interface between two phases as a sharp transition zone. In our work, we will study some patterns in type II superconductors, by combining the ideas derived from the general perspective of a pattern formation background with the theory of vortex dynamics. This analysis requires also accommodating the description of the contour dynamics of a domain of vortices, into a macroscopic picture, where the density of vortices is a continuum coarse-grained field.

This thesis has the following structure. The remaining part of this chapter introduces basic concepts on superconductivity and vortex patterns to give the reader the necessary background for the comprehension of this work and to offer a general view on the types of dynamical instabilities that we will analyse. We will first start from a brief description of the phenomenological Ginzburg-Landau and London theories; then we will define type II superconductors and the quantised fluxoid. The properties of Abrikosov vortices, like the energy of interaction for a slab and a film will then be discussed. Since in this thesis we are interested mainly in the dynamics of vortices and their collective behavior, we will focus thereafter on the dynamical regimes of these interacting strings. Finally, in the last two sections we will concentrate

on the thermo-magnetic instabilities that are observed in the intermediate state by presenting some examples of patterns in type II superconductors regarding some recent experiments.

In Chapter 2 we will deal with finger-like patterns in Nb [13,14]. We will analyse these instabilities by building a model that takes into account the coupling with the local temperature of the sample and formulate a novel type of approach based on a sharp interface description. The main purpose of this study is to derive features like the well defined finger shape, the width and their dependence with the substrate temperature. This theoretical model is the first example that clearly exhibits this type of fingered-shape patterns.

In Chapter 3, instead, we will examine the dynamics of a front between flux and anti-flux in the presence of an in-plane anisotropy. In this work we aim to understand the origin of the turbulence that was observed at the boundaries between regions with vortices and antivortices in $YBa_2Cu_3O_{7-\delta}$, that we have mentioned above [24].

Finally, in Chapter 4 we will summarize the main ideas and add some remarks on the dynamics of vortex fronts which are discussed in the previous chapters.

1.2 Ginzburg-Landau and London theories

The Ginzburg-Landau theory provides a very effective tool for a phenomenological description of the properties of vortices [4, 5, 32]. Also within the general perspective of the theory of front propagation, the Ginzburg-Landau equations are often used to analyse the formation of patterns. In particular, in the study of pattern-forming systems, like e.g. in the Rayleigh-Bénard convection, the Ginzburg-Landau equations are studied in the form of amplitude equations for traveling waves [33,34]. Within the framework of the more specific problem of front propagation in superconductors, the Ginzburg-Landau equations provide a phenomenological method to analyse the dynamics and the stability of interfaces between the normal and superconducting states.

This approach has generally restricted to type I superconductors [35–38], whereas for type II superconductors only few cases in the literature are encountered [39].

While the surface energy at the interface between the normal and superconducting states in a type I superconductor is positive, for a type II superconductor this is negative; therefore normal domains are unstable and subdivide until this process is limited by a microscopic length ξ, determined by the balance of the tendency to break up and the penalty of having too rapid variations in the superconducting properties.

Therefore, the reason why the Ginzburg-Landau method is not so directly used for a description of patterns in type II superconductors is that one needs to go beyond the microscopic scale ξ and adopt a more macroscopic approach, where the density of vortices is a continuum coarse-grained field.

In order to present the basic concepts to understand this thesis, we will here summarise briefly the main points of this formalism.

The Ginzburg-Landau theory is based on the postulate that the free energy functional $\mathcal{F}$ for the superconducting state can be expressed through an expansion of the complex order parameter $\psi(\mathbf{r}) = |\psi(\mathbf{r})| \exp(i\varphi(\mathbf{r}))$, that is assumed to be small near the critical temperature T_c and vary slowly in space. This functional is derived by imposing that it must be analytical and real, as

$$\mathcal{F} = \int d\mathbf{r} \left[\alpha|\psi|^2 + \frac{\beta}{2}|\psi|^4 + \frac{1}{2m^*} \left| \left(\frac{\hbar}{i}\nabla - \frac{e^*}{c}\mathbf{A} \right) \psi \right|^2 + \frac{(\nabla \times \mathbf{A})^2}{8\pi} \right], \quad (1.1)$$

where $\mathbf{A}$ is the vector potential of the microscopic magnetic field $\mathbf{h} = \nabla \times \mathbf{A}$. Here the fields are measured in Gaussian units. The effective charge is given by $e^* = 2e$, according to the BCS [40] microscopic theory of Cooper pairs, while for the effective mass m^* we assume the value $m^* = 2m$, where m is the mass of the electron. From equation (1.1) in the absence of magnetic fields, one can easily see that the constant coefficient β must be positive, otherwise the free energy would not be bounded from below. Moreover, depending on the sign of α, the minimum of the free energy functional occurs at $|\psi| = 0$

($\alpha > 0$) or at

$$|\psi|^2 = |\psi_\infty|^2 = -\frac{\alpha}{\beta}, \quad (\alpha < 0).$$

The difference of the minimum in the free-energy density between the superconducting ($\psi = \psi_\infty$) and normal states ($\psi = 0$), by definition, is equal to the opposite of the condensation energy, which is expressed through the critical thermodynamic magnetic field as [5]

$$f_\mathrm{s} - f_\mathrm{n} = -\frac{\alpha^2}{2\beta} = -\frac{H_c^2}{8\pi}. \tag{1.2}$$

A material becomes superconductor below the critical temperature T_c, where $|\psi|^2 \neq 0$, thus α changes sign at T_c; expanding the coefficient α near T_c yields

$$\alpha(T) = \alpha' \left(T/T_c - 1\right). \tag{1.3}$$

With the use of standard variational techniques, by minimizing the free energy with respect to the order parameter $\psi^*(\mathbf{r})$ and applying also the Maxwell equation $\mathbf{j}_\mathrm{s} = c/4\pi \, (\nabla \times \mathbf{h})$, the Ginzburg-Landau equations are obtained

$$\alpha\psi + \beta|\psi|^2\psi + \frac{1}{2m^*}\left(\frac{\hbar}{i}\nabla - \frac{e^*}{c}\mathbf{A}\right)^2 \psi = 0, \tag{1.4}$$

$$\mathbf{j}_\mathrm{s} = \frac{e^*}{m^*}\left(\hbar\nabla\varphi - \frac{e^*}{c}\mathbf{A}\right)|\psi|^2, \tag{1.5}$$

where the second equation gives the supercurrent density $\mathbf{j}_\mathrm{s}$ as a diamagnetic response of the superconductor. The Ginzburg-Landau approach provides a phenomenological description for temperatures sufficiently near T_c and spatial variations of ψ and $\mathbf{A}$ which are not too rapid. The equations are governed by the two characteristic lengths for a superconductor: the coherence length ξ and the penetration depth λ. The meaning of these fundamentals parameters can be understood easily from the equations (1.4). In a situation with no current or fields, we can restrict the analysis to the real function $f(r) = \psi(r)/\psi_\infty$, so the equation becomes

$$\frac{\hbar^2}{2m^*|\alpha(T)|}\nabla^2 f + f - f^3 = 0. \tag{1.6}$$

The linearisation of (1.6) around the superconducting state $f(r) = 1$, leads to the following equation in terms of $g(r) = 1 - f(r)$,

$$\xi^2 \nabla^2 g - 2g = 0, \quad \xi^2 = \frac{\hbar^2}{2m^*|\alpha(T)|} = \frac{\xi^2(0)}{1 - T/T_c}. \tag{1.7}$$

The relation above shows that the order parameter decays with a length of the order of the coherence length ξ which diverges at T_c, as expected for a critical phase transition. Similarly, the penetration depth λ, is derived from the second equation for the current density, when a weak field is considered. By approximating the order parameter for a homogeneous superconductor, $\psi = \psi_\infty$ and using Maxwell's equation, $\nabla \times \mathbf{h} = 4\pi \mathbf{j_s}/c$, we derive

$$\nabla \times (\nabla \times \mathbf{h}) = -\frac{16\pi e^2}{m^* c^2} |\psi_\infty|^2 \mathbf{h}. \tag{1.8}$$

Equation (1.8) shows, by using the relation $\nabla \cdot \mathbf{h} = 0$, that the magnetic field is screened by the diamagnetic currents and decays exponentially in the superconducting material (the so called Meissner effect). The decaying length λ is defined by

$$\lambda^2(T) = \frac{m^* c^2}{16\pi e^2 |\psi_\infty(T)|^2} = \frac{\lambda^2(0)}{1 - T/T_c}, \tag{1.9}$$

where the relation (1.3) for the temperature variation is considered. Equation (1.8), together with (1.9), is written as,

$$\lambda^2 \nabla \times (\nabla \times \mathbf{h}) + \mathbf{h} = 0, \tag{1.10}$$

which can be derived also in the framework of the London theory [42] by considering the energy functional

$$\mathcal{E} = \mathcal{E}_0 + \frac{1}{8\pi} \int d^3 r \, \left[\mathbf{h}^2 + \lambda_{\mathrm{L}}^2 (\nabla \times \mathbf{h})^2 \right]. \tag{1.11}$$

Here $\mathcal{E}_0$ is the condensation energy, $\mathbf{h}$ is the microscopic magnetic field, and λ_{L} is the London penetration depth, which is defined by

$$\lambda_{\mathrm{L}}^2 = \frac{mc^2}{4\pi n_{\mathrm{s}} e^2}, \tag{1.12}$$

where n_s is the density of superconducting electrons. The first term in the integral is the magnetic field energy, while the second term is the kinetic energy due to the supercurrents, where the relations $\mathbf{j}_s = n_s e \mathbf{v}_s$ and the Maxwell's equation $\nabla \times \mathbf{h} = 4\pi \mathbf{j}_s / c$ have been used.

The London theory is based on the fact that the wavefunction of the superconducting electrons is constant, with density given by $n_s = |\psi_\infty|^2$. As a consequence, the equation above for the supercurrent $\mathbf{j}_s$ yields the relation

$$\mathbf{j}_s = n_s e \mathbf{v}_s = -\frac{n_s e^2}{mc} \mathbf{A}, \tag{1.13}$$

and, taking the time derivative and using Ampere's equation, the first London equation is derived

$$\frac{d\mathbf{j}_s}{dt} = \frac{n_s e^2}{m} \mathbf{E}. \tag{1.14}$$

If we vary $\mathcal{E}$ with respect to $\mathbf{h}$, we obtain the second London equation, which has the same form of (1.10), with λ_L instead of λ. Near the regime for temperatures closed to T_c, the two theories must give the same description, and thus these two lengths coincide, $\lambda_L = \lambda$.

1.3 Type II superconductors

The ratio of the two characteristic lengths that have been introduced in the previous sections,

$$\kappa = \frac{\lambda}{\xi}, \tag{1.15}$$

called the Ginzburg Landau parameter, defines the distinction between type I and type II superconductors. One feature for which these two types of superconducting materials differ, as we have anticipated, is given by the surface energy of a domain wall between the normal and superconducting phases; this can be calculated from equations (1.4) and (1.5). The surface energy is determined in particular by the excess of the Gibbs energy due to the presence of the superconducting-normal interface over what it would be if its density was the one corresponding to an homogeneous superconducting

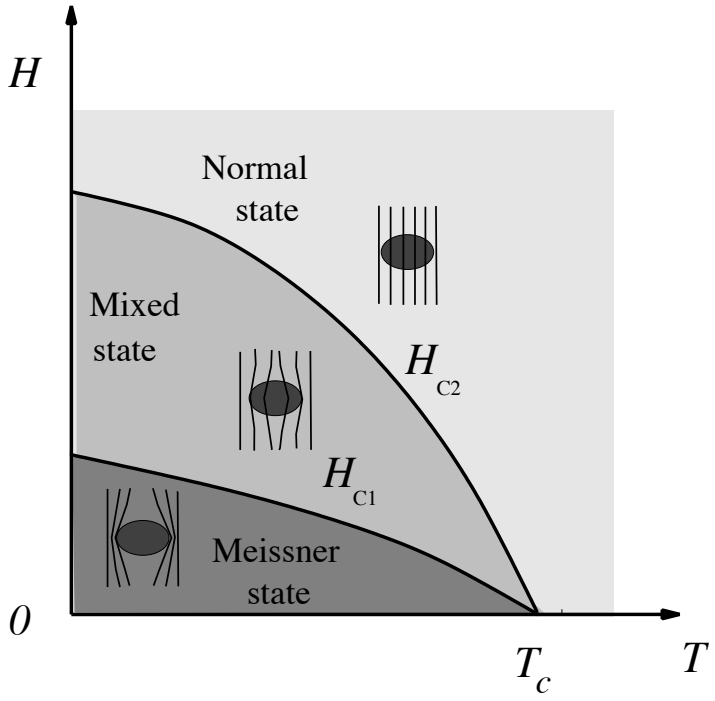

Figure 1.3: Mean-field phase diagram for a type II superconductor. Below the critical field $H_{c1}(T)$, the material in the Meissner-Ochsenfeld phase an external magnetic field is totally expelled. Between $H_{c1}(T)$ and $H_{c2}(T)$ in the intermediate state, the magnetic field penetrates by forming a regular array of vortices. At $H_{c2}(T)$ the material undergoes a second order phase transition from the mixed to the normal phase.

state. Numerical evaluations have shown that this energy is negative for values $\kappa > 1/\sqrt{2}$, corresponding to type II superconductors [5, 32].

The existence of vortices in type II superconductors was predicted by Abrikosov [2] in 1957, who solved the Ginzburg-Landau equations for the case $\kappa > 1/\sqrt{2}$ and showed that an equilibrium situation, between two critical fields $H_{c1}(T)$ and $H_{c2}(T)$, is characterised by a regular array of flux tubes. At each site of the lattice, a vortex of supercurrent encircles a quantised amount of magnetic flux $\phi_0 = hc/2e$.

Flux quantisation can be derived in the framework of the Ginzburg-

Landau formalism using the fact that the complex superconducting order parameter ψ must be a single-valued function. As a consequence, the phase φ must change by integral multiples of 2π for a closed integral path

$$\oint \nabla\varphi \, d\mathbf{s} = 2\pi n. \tag{1.16}$$

By considering a loop that encloses a vortex, and integrating for example through a circular path $\gamma(R)$ of radius R, it is easy to see that the fluxoid ϕ', defined by London [42, 43] as

$$\phi' = \phi(R) + \frac{4\pi}{c} \oint_{\gamma(R)} \lambda^2 \mathbf{j}_\mathrm{s} \, d\mathbf{s} = \oint_{\gamma(R)} \left(\mathbf{A} + \frac{4\pi\lambda^2}{c} \mathbf{j}_\mathrm{s} \right) \cdot d\mathbf{s}, \tag{1.17}$$

is quantised. Using indeed equations (1.5) and (1.9) for the supercurrent density $\mathbf{j}_\mathrm{s}$ and the penetration depth λ, one can verify that

$$\phi' = n\frac{hc}{e^*} = n\phi_0, \tag{1.18}$$

with $\phi_0 = hc/2e \sim 2.07 \times 10^{-7}$ G/cm^2. If the radius R of the contour is large enough, $R \gg \lambda$, the supercurrent density $\mathbf{j}_\mathrm{s}$ through the loop of integration decays to zero and the second term on the right of (1.17) can be neglected. Thus, the total flux trapped by a vortex is also quantised and for $n = 1$,

$$\phi = \phi_0. \tag{1.19}$$

At a finite magnetic field $H > H_{c1}$, the vortices penetrate the system. The array of vortices was later proven to be hexagonal, with the inter-vortex distance given by [44]

$$a = \left(\frac{4}{3}\right)^{1/4} \sqrt{\frac{\phi_0}{B}}. \tag{1.20}$$

As the mean-field phase diagram of Fig. 1.3 shows, at the critical field $H_{c2}(T)$, there is a second order phase transition from the mixed state with vortices, called also intermediate state or Schubnikov state, to the normal phase. Below the critical field $H_{c1}(T)$ the material becomes superconducting and, because of the Meissner-Ochsenfeld effect, an external magnetic field H is expelled. In the intermediate state, the magnetic field is partly expelled due to

the demagnetisation currents, thus the field penetrates in the form of quanta of flux, but the local internal magnetic field B is less than the applied one. The density of vortices increases with the magnetic field, also according to (1.20), till the cores of vortices overlap and $a \sim \xi$ at $H \sim H_{c2}(T)$.

It is important to stress that the diagram of phase represented in Fig. 1.3 is valid only in a mean field approximation, outside of the critical region in which the fields fluctuations are important. A measure to estimate the temperature window in which thermal fluctuations are relevant is given by the Ginzburg criterion [4]

$$|T_c - T| < T_c\, Gi, \quad Gi = \frac{1}{2}\left(\frac{T_c}{H_c^2(0)\xi^3(0)}\right), \tag{1.21}$$

where the Ginzburg number Gi defined above provides a measure of the relative size of the minimal condensation energy $H_c^2(0)\xi^3(0)$ within a volume set by the coherence length $\xi(0)$ at $T = 0$. In this thesis we will consider temperature effects for the phenomena of pattern formation by referring only to experiments in low-T_c superconductors, like Nb, for which the Ginzburg number is very low, $Gi \sim 10^{-8}$ and thus, according to (1.21), fluctuations can been neglected [4]. For high-T_c materials, instead, the fundamental Ginzburg parameter is much larger, e.g. $Gi \sim 10^{-2}$ for $YBa_2Cu_3O_{7-\delta}$, and thermal fluctuations give rise to a richer phase diagram, characterised also by new phase transitions, e.g. the melting transition of the vortex lattice. [4] .

1.4 Magnetic properties of vortices

Since in this thesis we focus on the non-equilibrium patterns of vortices, at the purpose of understanding their collective behavior and the mutual forces that act on these interacting strings, we will introduce here the microscopic magnetic field related to a vortex and the interaction energy between two magnetic flux lines. This is important to understand some issues for this thesis, for example, why vortices of the same sign tend to repel each other, leading to the expansion of a finite size domain. As a consequence, also

the surface tension that plays an important role at the interface with two different phases, e.g. between a normal solid and a liquid [49], cannot be defined for a domain of vortices, because of the absence of attractive forces. The form of the magnetic field associated with a vortex is needed also to derive how the currents decay with respect to the distance from the cores. Moreover, as we will see, while the interaction between vortices is screened for a slab, in a thin film these are long-range. The strength of the currents is crucial for the formation of the type of dendritic and finger-like patterns that we want to analyse, since they have been observed only in thin films [11].

1.4.1 Magnetic field of a flux line

In Sec. 1.2 we have introduced the London theory. This approach is based on the approximation that neglects the variation of the order parameter and thus is not capable to describe the vortex core. It is only valid therefore on scales larger than the coherence length ξ. However, for type II superconductors with a Ginzburg-Landau parameter $\kappa \gg 1$, defined by (1.15), the London theory provides a good phenomenological description for the spatial variation of the internal magnetic field.

In the presence of vortices Eq. (1.10) is modified and a source term on the right hand side must be included, so that we have

$$\lambda^2 \nabla \times (\nabla \times \mathbf{h}(\mathbf{r})) + \mathbf{h}(\mathbf{r}) = \phi_0 \sum_{i=1}^{N} \hat{\mathbf{t}}_i(s) \delta(\mathbf{r} - \mathbf{r}_i(s)), \tag{1.22}$$

where ϕ_0 is the flux quantum and $\hat{\mathbf{t}}_i(s)$ is the tangent vector along the i-th vortex. Here we assume that the vortices are straight and point along the field direction, which we will take as the $\mathbf{z}$-axis. Let us determine first the solution for the microscopic magnetic field $h(\mathbf{r})$ for one isolated vortex. Using $\nabla \cdot \mathbf{h} = 0$, we find that Eq. (1.22) becomes

$$\left(-\lambda^2 \nabla^2 + 1\right) \mathbf{h}(\mathbf{r}) = \hat{\mathbf{z}} \phi_0 \delta(\mathbf{r}). \tag{1.23}$$

The solution of this equation is given by the zero order Bessel function

$$h(r) = \frac{\phi_0}{2\pi\lambda^2} K_0(r/\lambda), \tag{1.24}$$

which has the asymptotic form of a logarithmic behavior at short distances from the core, and decaying as $\sqrt{1/r}\exp(-r/\lambda)$ for $r \to \infty$

$$h(r) \sim \frac{\phi_0}{2\pi\lambda^2}\ln(\lambda/r), \;\; \xi < r \ll \lambda, \tag{1.25}$$

$$h(r) \sim \frac{\phi_0}{2\pi\lambda^2}\sqrt{\frac{\pi\lambda}{2r}}e^{-r/\lambda}, \;\; r \gg \lambda. \tag{1.26}$$

As we have pointed out, the spatial variation of the magnetic field inside the core can not be considered within the framework of the London theory. The inferior limit of the relation (1.25) therefore comes from the limitations of this approach. One should use the Ginzburg Landau formalism to go beyond the limit $r < \xi$.

1.4.2 Vortex-line Energy

From the form of the microscopic magnetic field $\mathbf{h}$, the energy of an isolated vortex line can be calculated straightforwardly. By considering indeed the total energy

$$\mathcal{E}_1 = \int \frac{1}{8\pi}\left(h^2 + \lambda^2|\nabla \times \mathbf{h}|^2\right), \tag{1.27}$$

using the vectorial relation $\nabla\cdot(\mathbf{h}\times(\nabla\times\mathbf{h})) = |\nabla\times\mathbf{h}|^2 - \mathbf{h}\cdot|\nabla\times(\nabla\times\mathbf{h})|$, and neglecting the core this relation can be written as [5, 6]

$$\frac{\lambda^2}{8\pi}\oint \mathbf{h}\times(\nabla\times\mathbf{h})\cdot d\mathbf{s}. \tag{1.28}$$

Integrating in a loop around the core, the asymptotic logarithmic form that we have found for the magnetic field of a vortex (1.25) yields for $\xi < r \ll \lambda$

$$|\nabla\times\mathbf{h}| \sim \frac{\phi_0}{2\pi\lambda^2}\frac{1}{r}. \tag{1.29}$$

Using espression and the relation $h(0) \sim h(\xi)$, since the magnetic field for $r < \xi$ is approximately constant, the energy of a vortex line is determined as

$$\mathcal{E}_1 = \frac{\phi_0^2}{4\pi\lambda^2}\ln\left(\frac{\lambda}{\xi}\right) = \frac{\phi_0^2}{4\pi\lambda^2}\ln\kappa, \tag{1.30}$$

where κ is the Ginzburg-Landau parameter.

1.4.3 Interaction between vortices

Let us consider two interacting vortices. Since the total local magnetic field at a point $\mathbf{r}$ can be written, in view of the linearity of (1.22), as a superposition of the two magnetic fields corresponding to the two vortex cores at a position $\mathbf{r_1}$ and $\mathbf{r_2}$ respectively, $h(\mathbf{r}) = h_1(\mathbf{r}) + h_2(\mathbf{r})$ and substituting into the (1.28), the total magnetic energy can be written as

$$\mathcal{E} = 2\mathcal{E}_1 + 2\mathcal{E}_{12}. \tag{1.31}$$

The first term in the expression above is the energy of one vortex lines calculated in the previous section and derives from the self-interaction due to the coupling between the magnetic field of each vortex and the supercurrent encircling the core. The second term expresses instead the energy of interaction between the two vortices and is given by

$$\mathcal{E}_{12} = \oint \mathbf{h_1} \times (\nabla \times \mathbf{h_2}) \cdot d\mathbf{s_2}, \tag{1.32}$$

where the integration is meant for a loop encircling the vortex at position $\mathbf{r_2}$. Therefore, by following the same type of calculation of the previous section, this is written as

$$\mathcal{E}_{12} = \frac{\phi_0}{4\pi} h(|\mathbf{r_1} - \mathbf{r_2}|) = \frac{\phi_0^2}{8\pi^2\lambda^2} K_0\left(\frac{|\mathbf{r_1} - \mathbf{r_2}|}{\lambda}\right), \tag{1.33}$$

which shows that the interaction energy between the vortices is proportional to the magnetic field $h(|\mathbf{r_1} - \mathbf{r_2}|) = h(r_{12})$, so it has a logarithmic dependence for $\xi \ll r_{12} < \lambda$ and behaves as as $1/\sqrt{r_{12}}\exp(-r_{12}/\lambda)$ for $r_{12} > \lambda$. The interaction between vortices is *repulsive*.

The fact that vortices of the same sign repel each other has an important consequence also for their collective dynamics, on which we want to focus in this thesis. Unless these interacting strings are in the stable configuration of an hexagonal array that minimises the free energy of the system or inhomogeneities prevent their motion, a domain of vortices tends therefore to expand. On the other hand vortices of opposite charge do attract each other, since the two magnetic fields of a vortex and an anti-vortex have also

opposite sign and the interaction is negative as a consequence of (1.32) and (1.33), as we will see also in the Chapter 3.

1.4.4 Interactions in a thin film

As we have seen, at large distances the interaction between vortices is screened by the supercurrents. This screening effect is reduced in a thin film, for which the thickness $d < \lambda$, and interactions are thus long-range. The out-of-equilibrium patterns that we want to describe in this thesis have been observed mainly in thin films, for which the strong interactions play an important role for the formation of these instabilities. The details of the derivation of these interactions which was done by Pearl, can be found in [47] and also in [48]. As a result of the analysis the vortex interaction between two vortices at distance r_{12} given by

$$\mathcal{E}_{12}(r_{12}) = \frac{\phi_0}{8\pi\Lambda}[H_0(r_{12}/\Lambda) - Y_0(r_{12}/\Lambda)], \tag{1.34}$$

where H_0 and Y_0 are Hankel functions and the $\Lambda = 2\lambda^2/d$ is an effective penetration depth for a thin film. The asymptotic behavior of this energy is logarithmic at short distances, like in the case of a slab, for $\xi < r_{12} \ll \Lambda$

$$\mathcal{E}_{12}(r_{12}) \sim \frac{\phi_0^2}{4\pi\Lambda} \ln\left(\frac{\Lambda}{r_{12}}\right), \tag{1.35}$$

and at large distances, $r_{12} \gg \Lambda$, decays as

$$\mathcal{E}_{12}(r_{12}) \sim \frac{\phi_0^2}{4\pi^2 r_{12}}. \tag{1.36}$$

1.5 The Lorentz force

From the interaction energy between vortices that we have introduced in the previous sections one can compute the force that acts on each magnetic flux line due to the coupling with the supercurrent density $\mathbf{j}$ of the other vortices. Deriving for example the interaction energy $\mathcal{F}_{12}$ in (1.33) in the direction x

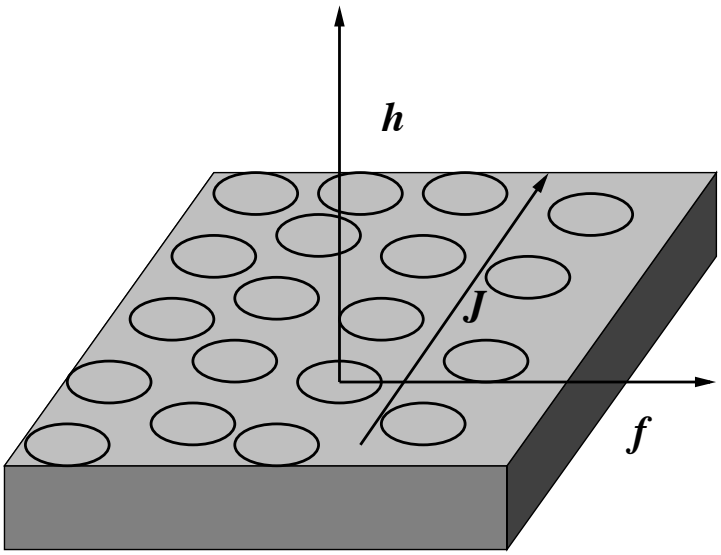

Figure 1.4: Schematic representation of the origin of the Lorentz force acting on a vortex, due to the coupling between the local magnetic field **h** and a macroscopic current **J** due to a gradient in the density of vortices.

of the x-y plane of a slab one gets

$$f_{2x}(\mathbf{r}_2) = \frac{\partial F_{12}}{\partial x_2} = -\frac{\phi_0}{4\pi}\frac{\partial h_1(\mathbf{r}_2)}{\partial x_2} = \frac{\phi_0}{c} j_{1y}(\mathbf{r}_2), \tag{1.37}$$

where the Maxwell equation $\nabla \times \mathbf{h} = 4\pi\mathbf{j}/c$ has been used. Extending the result to the vectorial form, we derive

$$\mathbf{f}_2 = \mathbf{j_1} \times \frac{\phi_0}{c}, \tag{1.38}$$

which is the force acting on a vortex at position $\mathbf{r_2}$, due to the vortex at $\mathbf{r_1}$. Generalizing the problem for an array of vortices, the total force is given by

$$\mathbf{f} = \mathbf{J} \times \frac{\phi_0}{c}, \tag{1.39}$$

where **J** is the total macroscopic current density acting on a flux line, due to the presence of the other vortices. Unless the total current vanishes, a vortex moves thus under the effect of this force, called Lorentz force, or, Magnus force. The reason why it is often referred as Magnus force, in analogy

with the hydrodynamical force in a fluid, is represented in Fig. 1.4: in a non-equilibrium situation, the non-homogeneous vortex density leads to a gradient in the phase of the superconducting parameter $\nabla\varphi$ at a point in the space, and, consequentely, for (1.5), to a macroscopic current density $\mathbf{j}_s$ that is responsible for the motion of the vortices. The Lorentz force in (1.39) is generated also for any externally imposed transport current.

1.6 The dynamics of vortices

In this section we will discuss the different regimes that characterise the dynamics of vortices. When vortices move with a velocity $\mathbf{v}$, they induce an electromagnetic field [3–6]

$$\mathbf{E} = \mathbf{B} \times \frac{\mathbf{v}}{c}, \tag{1.40}$$

parallel to $\mathbf{j}$, that acts as a resistive voltage, due to the fact that the magnetic flux trapped in a superconductor decreases. The motion of vortices is thus accompanied by dissipation, leading to a resistance that destroys the persistent currents. The motion of vortices can be prevented, however, by pinning forces due to inhomogeneities. Depending on the relative strength of these forces with respect to the driving Lorenz force, we can distinguish different regimes. For low currents the dynamics is dominated by the so called *creep* regime, in which vortices hop from one pinning center to an other. This motion is thermally activated, as we will see in more detail. If the pinning instead is weak in comparison to the Lorentz force, vortices move with a steady viscous motion, in which the driving force is balanced by a friction force. This regime is referred as *flux flow*. The response of the superconducting material to a macroscopic transport current density $\mathbf{j}$, is represented by the electric field-current characteristic, as shown in Fig. 1.5. While for a current density $j \gg j_c$, where j_c is the critical pinning current density, this relation is linear, in the regime for $j \leq j_c$, the response in nonlinear and strongly temperature dependent. In an idealised E-j characteristic, one can assume a sharp behavior with a linear function $E(j)$ for $j \geq j_c$ and $E(j) = 0$,

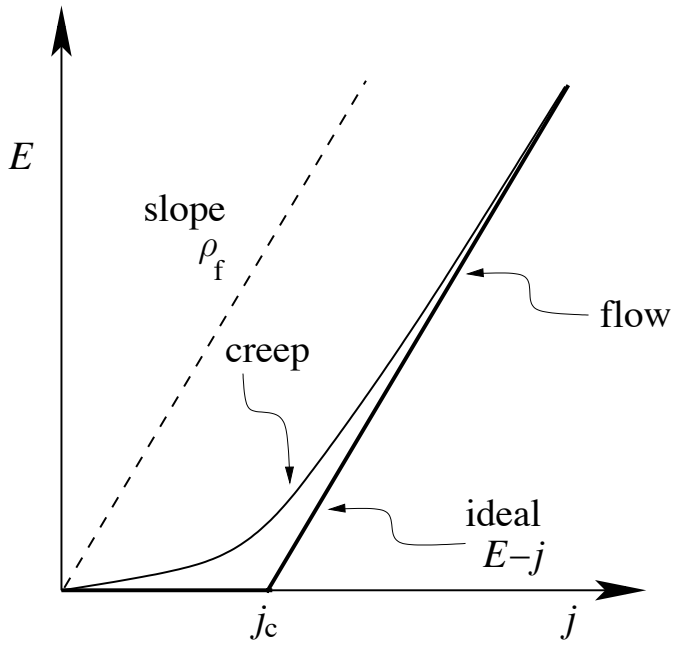

Figure 1.5: This figure represents the form of the electric-field current characteristic for the intermediate state of a type II superconductor. For currents $j \gg j_c$, the dependence is linear, and the E-j relation is dominated by the flux flow regime, whereas for $j < j_c$ the E-j relation is strongly nonlinear and dominated by the creep regime. The idealised E-j characteristic, which is linear above j_c and equal to zero below j_c, is also represented.

for $j \leq j_c$.

An important consideration to underline for our study in the collective dynamics of vortices is that, except for the regime of very high fields and currents, as a consequence of the strong mutual repulsive interactions between flux lines, vortices do not move individually, but tend to form bundles corresponding to several units of flux quantum. This behavior is enhanced expecially in the creep regime, in which a pinning barrier has to be overcome. While discussing the dynamics of vortices, we will thus not refer to the microscopic field of a single vortex line, but we will focus on the macroscopic average internal magnetic field $\mathbf{B}$.

1.6.1 The flux flow regime

If pinning is weak, for a vortex that moves with a velocity $\mathbf{v}$, the phenomenological equation that governs the dynamics of vortices is

$$\mathbf{F}_{\mathrm{L}} = \eta \mathbf{v} = \mathbf{j} \times \frac{\phi_0}{c} \hat{\mathbf{z}}, \tag{1.41}$$

where η is a viscosity coefficient that we will define later in this section. The power which is dissipated in this motion can be expressed in terms of the viscosity as

$$W = \mathbf{F}_{\mathrm{L}} \cdot \mathbf{v} = \eta v^2. \tag{1.42}$$

The simplest approximation for this regime was derived by Bardeen and Stephen [50], which is based essentially on the two fluid model, according to which the total electron density can be divided in two parts: the superconducting component with density n_{s} and the normal component with density n_{n}. While for the normal electrons, we can apply Ohm's law and the relation $\mathbf{j}_{\mathrm{n}} = (n_{\mathrm{n}} e^2 \tau_{\mathrm{n}}/m)\mathbf{E}$, where τ_{n} is the relaxation time due to the scattering with the impurities, for the superconducting component, the approximation based on the perfect conductivity $\tau_{\mathrm{s}} = \infty$ is made, like in the London theory [42]. The Bardeen-Stephen model is derived thus by assuming that inside the core of a vortex, for $r < \xi$ there is only the normal component, while outside the London equation applies. By imposing the continuity of the field and the relation (1.42) for the rate of energy which is dissipated, the viscosity coefficient η is derived

$$\eta = \frac{\phi_0 H_{c2}}{\rho_{\mathrm{n}} c^2}. \tag{1.43}$$

The resistivity for the flux flux regime, which relates the supercurrent density $\mathbf{j}$ to the electric field $\mathbf{E}$, is defined as

$$\rho_{\mathrm{f}} = \frac{E}{j} = \frac{B\phi_0}{\eta c^2}, \tag{1.44}$$

where the expression (1.40) and (1.41) have been used. Combining this last relation with the result for the Bardeen-Stephen viscosity (1.43), leads to the rate between the flux flow resistivity ρ_{f} and the normal resistivity ρ_{n}

$$\frac{\rho_{\mathrm{f}}}{\rho_{\mathrm{n}}} \sim \frac{B}{H_{c2}} \sim \frac{\pi \xi^2}{a^2}, \tag{1.45}$$

that equals the ratio between the area occupied by the normal core and the area per vortex. For $B \to H_{c2}$ the flux flow resistivity tends continuously to the one of a normal metal, as expected, since there is a second order transition. In reality, as well as this longitudinal viscosity, one can define a transversal viscosity given by a Hall effect and the equation for the balance of the forces is generalised to [3, 4]

$$\frac{\phi_0}{c}\mathbf{j} \times \hat{\mathbf{z}} = \eta\mathbf{v} + \alpha_0\mathbf{v} \times \hat{\mathbf{z}}, \tag{1.46}$$

where $\alpha_0 \ll \eta$ for a dirty superconductor with a rather short electronic mean free path. Usually, the second term due to the transverse Hall effect is thus neglected in most of type II materials.

In a material characterised by an in-plane anisotropy, as we will see in Chapter 3, the effective viscous drag coefficient depends on the direction of propagation of the vortices. More precisely, the mobility defined in (1.41) becomes a non-diagonal tensor. As a consequence, there is a non-zero component of the velocity $\mathbf{v}$ perpendicular to the driving Lorentz force. In Chapter 3 we will examine the problem of the dynamics of a boundary between flux and anti-flux and the possible role that the non-collinearity between the velocity and the force could have on the instability of the front.

1.6.2 The creep regime

For low current densities, $j \leq j_c$, the pinning forces due to inhomogeneities and defects in the lattice play a relevant role in the dynamics of vortices. In this regime the current-voltage characteristic is highly nonlinear and temperature dependent. For a driving Lorentz force weaker than the pinning barrier, the vortex lines move because of thermal activation; their motion is small but finite and a weak dissipation is present.

When the magnetic flux penetrates into a superconducting material, the macroscopic field $\mathbf{B}$ inside the material drops from a finite value to zero. According to Maxwell's law, the macroscopic current density is, for an external

field in the $\hat{\mathbf{z}}$ direction and that propagates in the $\hat{\mathbf{x}}$ direction,

$$j = \frac{c}{4\pi}\frac{dH}{dx} \approx \frac{c}{4\pi}\frac{dB}{dx}. \tag{1.47}$$

where in the last relation the approximation $\mathbf{B} \approx \mathbf{H}$ that neglects the magnetisation of the sample has been made; this is quite appropriate for a type II superconducting material with a Ginzburg-Landau parameter $\kappa \gg 1/\sqrt{2}$ [5]. Since a Lorentz force given by

$$\mathbf{F}_{\mathrm{L}} = \mathbf{j} \times \frac{\phi_0}{c}\hat{\mathbf{z}} \tag{1.48}$$

acts on the vortices, the magnetic flux tends to penetrate further, reducing the gradient of the magnetic field and therefore the current, for (1.47), till the Lorentz force per unit volume is less than a critical value, determined by the pinning barrier

$$F_{\mathrm{L}} \leq F_c. \tag{1.49}$$

This situation suggests that flux penetration can be described in terms of a *critical state*, in which the magnetic field enters the superconducting material with a linear profile with slope $4\pi j_c/c$, according to the Bean model [7]. This picture, in which the current density j_c is assumed to be constant and independent on the external magnetic field, represents a metastable state, which could develop into instabilities like flux jumps and avalanches. From the general perspective of critical phenomena, this state has been the object of studies that have focused on the kinetic roughening of the front and the determination of the scaling behavior of the front fluctuations [46].

As was shown by Kim *et al.* [51], the critical state decays logarithmically with time at finite temperatures. This phenomenon was explained with the creep theory, formulated by Anderson and Kim [52], which is based on the assumption that vortices jump from one pinning center to an other with a rate in terms of a thermal activated barrier given by [52]

$$R = \omega_0 e^{-U_0/T}, \tag{1.50}$$

where U_0 is is the activation barrier due to the pinning, and ω_0 is the frequency of vibration for flux jumps, and T is the temperature (the Boltzmann

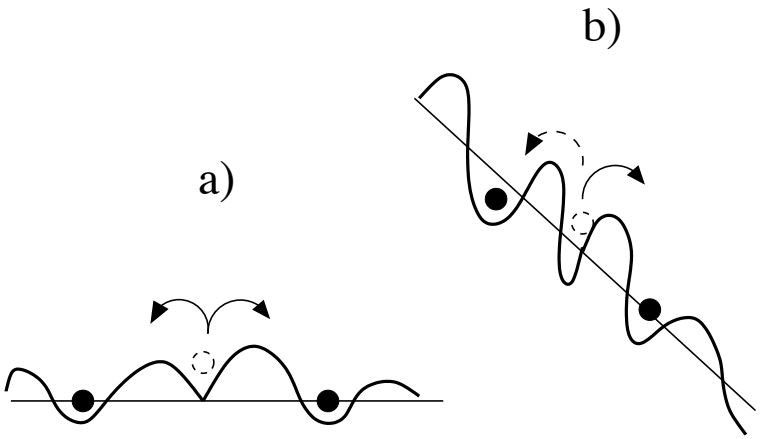

Figure 1.6: Schematic representation of the creep state. a) In the absence of a net force, vortex bundles jump with unbiased probability to the next valleys of the pinning potential. b) The presence of a driving force favors jumps in a "downhill" direction.

coefficient has been omitted here). In the absence of a net force acting on the vortex bundle, the probability for a jump to a pinning site is independent on the direction. The situation clearly change when a finite transport current makes favorable jumps which are in the "downhill" direction of the driving force. This situation is represented schematically in Fig. 1.6. The net jump rate is thus determined by

$$R = \omega_0 e^{-U_0/T} \left(e^{\Delta U/T} - e^{-\Delta U/T} \right) \tag{1.51}$$

where ΔU is the work done to move a flux bundle and is therefore proportional to the Lorentz driving force. This leads to a net creep velocity of

$$\nu = 2\nu_0 e^{-U_0/T} \sinh \frac{\Delta U}{T}. \tag{1.52}$$

For a large driving force, $\sinh(\Delta U/T) \sim \exp(\Delta U/T)$, the velocity of the bundle is given by

$$\nu = \nu_0 e^{-U(j)/T}, \tag{1.53}$$

where the energy $U(j)$ is the total activation barrier that the vortices have to overcome and depends on the current density j through the Lorentz force.

Since the barrier $U(j)$ vanishes at the critical current j_c, for currents sufficiently close to j_c, $U(j)$ can be simplified as

$$U(j \to j_c) \approx U_c \left(1 - \frac{j}{j_c}\right)^{\alpha}, \tag{1.54}$$

where U_c is the pinning activation barrier [4]. In this thesis we will consider the Anderson's original proposal of equation (1.54) with the coefficient $\alpha = 1$. For conventional low-T_c materials, to which we will restrict in our study while considering the creep regime, the typical values for the activation energy U_c are very large, $T/U_c \approx 10^{-3}$ [4, 53].

As we will in the next Chapter, the steepness of the velocity-current relation, plays a crucial role in the conflict between the heat generation and loss in the material. It is thus very important for the formation of thermomagnetic instabilities.

1.7 Thermomagnetic instabilities

As a consequence of the Joule heating effect induced by the electromagnetic field (1.40), a thermal instability can develop if the amount of heat that is generated can not be transfered fast enough to the substrate. We will discuss and underline here the main ideas of the theory of bistability in superconductors that constitute the starting point to carry our analysis on fingers patterns in Chapter 2. In this section we will refer in particular to the reviews of [8, 9]. The Joule self-heating effect in type II superconductors, is given by the coupling of the electromagnetic field $\mathbf{E}$ in (1.40) and the current density $\mathbf{j}$. By indicating with $Q(T, j)$ the power density which is dissipated, we have

$$Q(T, j) = E(T, j)j. \tag{1.55}$$

For a thin film of thickness d, in contact with a substrate that is kept at the bottom at a fixed temperature T_0, in the heat balance we take into account also the amount of energy that is transfered to the substrate; this is given by

$$W(T) = \frac{h}{d}(T - T_0), \quad (T - T_0) \ll T_0, \tag{1.56}$$

where h is the heat transfer coefficient of the substrate. Equation (1.56) holds if the temperature change along the thickness of the film can be ignored, [8]

$$d \ll d_{\mathrm{c}} \sim \frac{K}{h}, \tag{1.57}$$

where K is the thermal conductivity of the film. By considering the different contributions in the equation for the temperature and neglecting the heat diffusion, we derive

$$C\frac{\partial T}{\partial t} = Q(T, j) - W(T), \tag{1.58}$$

where C is the heat capacitance of the film. The condition of steady-state balance for a fixed current density $\mathbf{j}$ is satisfied for a temperature T such that

$$Q(T, j) = W(T). \tag{1.59}$$

Linearising (1.58) around the stable point, with respect to small perturbations of the temperature field, leads to the stability criterion

$$\frac{\partial W}{\partial T} > \frac{\partial Q}{\partial T}. \tag{1.60}$$

As the grafic solution of Fig. 1.7 shows, for a steep enough current-voltage characteristic, the curve that represents the heat generated $Q(T, j)$ intersects the curve corresponding to the heat loss $W(T)$ in three points, for current density j in a certain range $j_* < j < j^*$. The states corresponding to T_1 and T_3 are stable, whereas the one at T_2 is unstable, according to the relation (1.60). In order to understand better the conditions in which a thermal instability can develop, let us consider the idealised E-j characteristic, that we have explained in Sec. 1.6, so that

$$E = \rho_{\mathrm{f}}(j - j_c(T)), \quad (j > j_c(T)), \tag{1.61}$$

where ρ_{f} is the flux flow resistivity. Therefore, by indicating with T^* the temperature at which $j = j_0(T^*)$, $Q(T, j)$ has the form of a stepped function, given by the following set of equations

$$Q(T, j) = 0, \quad T < T^* \tag{1.62}$$

$$Q(T, j) = \rho_{\mathrm{f}} j(j - j_c(T)), \quad T^* < T < T_c \tag{1.63}$$

$$Q(T, j) = \rho_{\mathrm{n}} j^2 = Q(T_c, j), \quad T > T_c, \tag{1.64}$$

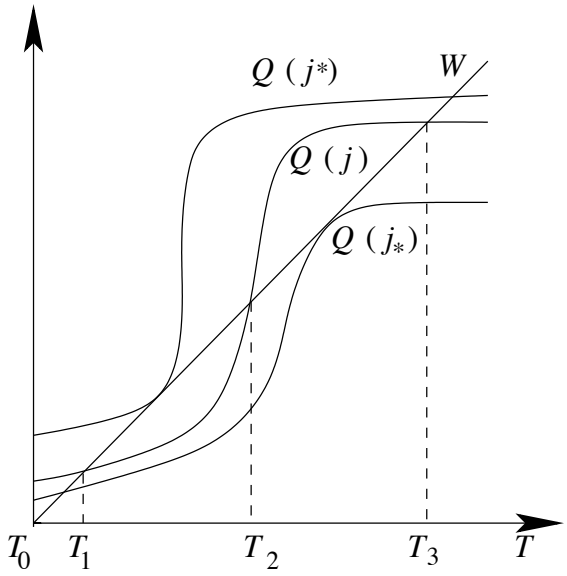

Figure 1.7: Grafic solution of the heat balance. For a current density in a certain interval $j_* < j < j^*$, the curves that represent the heat generated $Q(T, j)$ and the heat loss to the substrate intersect in three points. The states corresponding to T_1 and T_3 are stable, whereas the one at T_2 is unstable.

where the last relation follows from the E-j relation for a normal metal. By using the condition of steady state (1.59) and expressing it in the dimensionless form, with $\theta = (T - T_0)/(T_c - T_0)$ and $i = j/j_0$, $j_0 = j_c(T_0)$, we find two intersection points for $W(\theta)$ and $Q(\theta)$

$$\theta_2(i) = \frac{\alpha i(i-1)}{1-\alpha i}, \qquad \theta_3(i) = \alpha i^2, \tag{1.65}$$

where we have considered a linear temperature dependence of the critical current with respect to the dimensionless variables as $j_c(\theta) = j_0(1-\theta)$. The dimensionless parameter α, defined also as Stekly parameter, is equal to the ratio between the heat generated for $j = j_0$, $\rho_{\rm f} j_0^2$ and the heat transfered to the substrate, $(T_c - T_0)h/d$

$$\alpha = \frac{\rho_{\rm f} j_0^2 d}{h(T_c - T_0)}. \tag{1.66}$$

The critical current j_0 and the flux flow resistivity do depend on the mag-

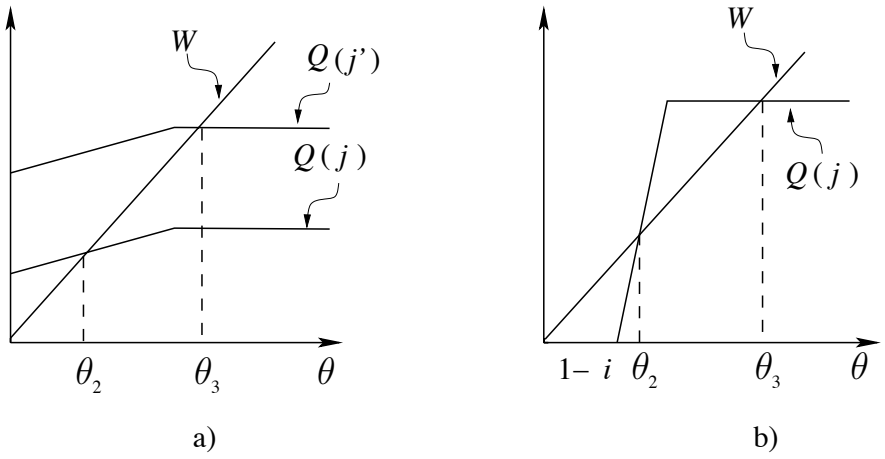

Figure 1.8: Graphic solution of the heat balance for an idealised current-voltage characteristic in two cases a) for $j > j_0$ and $\alpha < 1$ b) for $j < j_0$ and $\alpha > 1$.

netic field B and thus on its spatial variations in the sample. However, here and in the model that we will develop in Chapter 2 we will consider a constant magnetisation and neglect therefore spatial dependences of the critical current. Therefore we consider α as a constant. Our approximation is justified by the fact that an almost constant induction was measured inside finger-like and dendritic patterns in the experiments of [11, 12]. Depending on the relative strength between j and j_0, we have two different cases for the existence of θ_2: for $j > j_0$ and $\alpha < 1$, or $j < j_0$ and $\alpha > 1$. This situation is represented schematically in Fig. 1.8, which shows that a thermal instability due to self-heating can develop only in the second case. The intersection θ_2, for the superconducting state, corresponding to (1.65) is a stable point for the first case, and unstable point for the second case.

By substituting (1.65) in (1.61), one finds

$$j = \frac{j_0 + \rho_{\mathrm{f}}^{-1} E}{1 + \alpha E / \rho_{\mathrm{f}} j_0}, \tag{1.67}$$

which shows that the conductivity is decreased due to self-heating. Moreover, in the limit for superconductors with high critical current density $j_0 \gg E\rho_{\mathrm{f}}^{-1}$,

the conductivity

$$\sigma(E) = \frac{\partial j}{\partial E} = (1-\alpha)\rho_{\mathrm{f}}^{-1} \tag{1.68}$$

is obtained. Therefore, from (1.68), one can easily see that $\sigma(E)$ becomes negative for $\alpha > 1$. This clearly points out a thermal instability. For $j < j_0$, and $\alpha > 1$ therefore, self-heating is relevant.

Moreover, a thermal bistability develops for a certain range of current densities $j_{\mathrm{m}} < j < j_0$, for which the heat balance is satisfied in three points, like represented in Fig. 1.7. This is derived by imposing the heat balance $\rho_{\mathrm{f}} j_{\mathrm{m}}^2 = (T_c - T_0)h(T_c)/d$, j_{m} as $j_{\mathrm{m}} = \alpha^{-1/2} j_0$. As it follows from (1.66), the parameter α decreases with the temperature; as a consequence the thermal instability is observed in a certain window $T_c - \Delta T < T_0 < T_c$, outside of which $\alpha < 1$ and self-heating is negligibly small [8]. By considering for example a temperature dependence of the critical pinning current density of the type $j_c(T) = j_0(1 - T/T_c)$, and substituting it in (1.66), the interval ΔT is estimated as

$$\frac{\Delta T}{T_c} = \frac{hT_c}{\rho_{\mathrm{f}} d j_0^2}. \tag{1.69}$$

The facts that the dendritic and finger-shape patterns that we will analyse are observed in a certain temperature window and that the magnetic distribution does not extrinsically depend on the inhomogeneities of the sample, support the interpretation of this phenomenon in terms of this bistable character due to the Joule self-heating effect.

1.8 Out-of-equilibrium vortex patterns

In the study of fronts in type II superconductors, in this thesis, we will concentrate in particular on two different examples of dynamical instabilities: finger-like patterns and turbulence at the boundary between flux and anti-flux. By using a high-resolution magneto-optical technique, the development of an initially flat front into finger-like or dendritic patterns was first observed by Duran et al. [10] for a Nb thin film. This technique works by

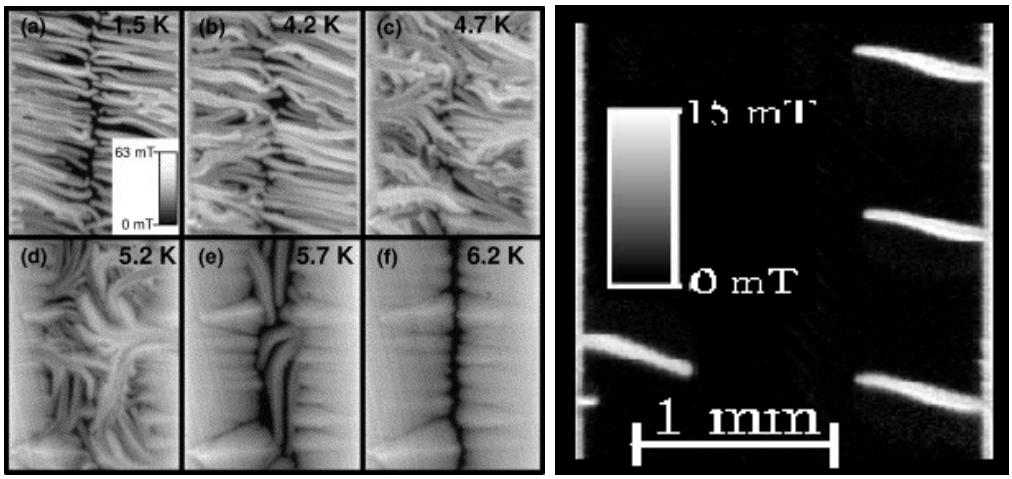

Figure 1.9: On the left: magnetic flux distribution of a Nb thin film of thickness 0.5 μm after zero-field cooling and for a magnetic field of 40 mT and different temperatures. The critical temperature is $T_c \sim 9.2K$. On the right: finger-like patterns in a 0.5 μm film of Nb at $T = 4.2$ K and a field of 6.8 mT. After [14].

placing a magneto-optical thin film near a superconducting material and using polarised light to measure the local magnetic field. The nucleation of these patterns ranges from one-dimensional structures at 3-4 K, that we will indicate with "fingers", to a more complex magnetic flux distribution with "sea-weed-like" branches, which are referred as "dendrites", at 6-7 K. These instabilities were found only in a temperature window, outside which the magnetic flux penetrates uniformly; in these experiments, in particular, they were observed between $T/T_c \sim 0.35$ and $T/T_c \sim 0.65$, for a critical temperature $T_c = 9.2$ K. Dendrites nucleate and propagate very fast, independently of the rate at which the external magnetic field is increased, and the velocity of propagation is sometimes not even measurable with the resolution of a standard magneto-optical technique. Finger-like patterns were studied also in detail by Welling et al. [13, 14]. In Fig. 1.9, taken from the experiments, the image on the left represents the magnetic flux distribution for a Nb thin

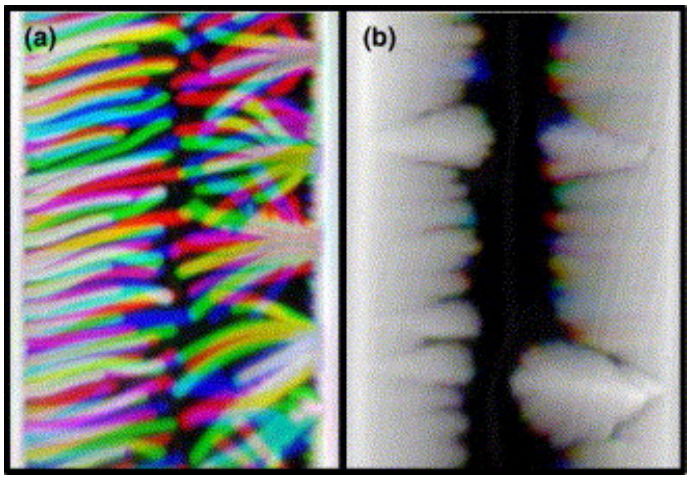

Figure 1.10: a) Overlapping images related to different experiments in the same sample at 4.2 K and 20 mT, which show that the instability does not depend trivially on defects and inhomogeneities (see for a color version Physica C **411**, 11 (2004)). b) At 6.7 K the magnetic flux distribution presents a more complex structure with dendrites. After [14].

film of 0.5 μm on a sapphire substrate after zero-field cooling and for a magnetic field of 40 mT and different temperatures. The white areas represent the Shubnikov mixed state with vortices, while the dark area stand for the superconducting Meissner state.

As one can observe, with increasing the temperature, the structure of the domains of vortices becomes more irregular, presenting the morphology of dendritic patterns. The image on the right reproduces instead instantaneous bursts of magnetic flux with the well defined finger-like shapes at 4.2 K.

Fig. 1.10 represents overlapping images related to different experiments in the same sample at 4.2 K and 20 mT. The image clearly shows that the instability is intrinsic and does not depend trivially on defects and inhomogeneities. At 6.7 K the magnetic flux distribution presents a more complex structure with dendrites.

As we will show with our analysis in Chapter 2, the features of these

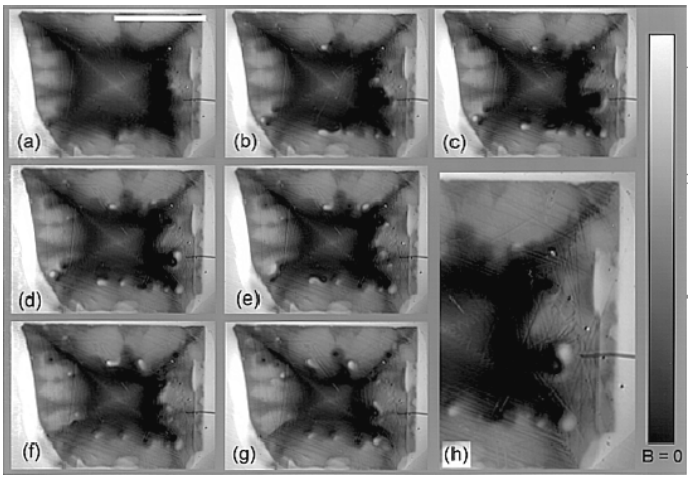

Figure 1.11: "Turbulent" behavior observed at the boundaries between vortices and antivortices in a $YBa_2Cu_3O_{7-\delta}$ single crystal at a temperature of 65 K. The sequence shows the time development after a) 10 s, b) 20 s, c) 30 s, d) 40 s, e) 60 s, f) 90 s and g) 150 s. After [24].

patterns can be studied in terms of an intrinsic instability due to the overheating of the sample. The thermo-magnetic nature of these instabilities due to the competition between the Joule heat released and the the relaxation to the substrate, that we have described in the previous section, has been proposed in [19–21]. We will show the importance of this mechanism in the selection of the patterns characteristics like the shape and the width of the fingers. In our analysis we will consider the approximation in which the density of vortices inside the domain is constant and we will therefore assume a non-zero current density only at the edge of the domain of vortices.

As we will also discuss in Chapter 2 these pattern have been shown to reproduce the temperature distribution of the sample. The interpretation that has been suggested for these phenomena [19, 20] is that the dissipation induced by the motion of vortices leads to an increase of the film temperature and thus to a lower pinning barrier and an enhanced mobility. As a consequence, a large scale flux invasion penetrates the material, giving rise

to avalanches. The condition of thermo-magnetic bistability that we have discussed in the previous section is crucial for the development of this mechanism. In this thesis we will support and confirm this argument by proposing a model in which the shape of the vortex fingers is strictly dependent on the temperature of the pattern.

While it is now generally accepted that the formation of finger-like and dendritic patterns is of thermo-magnetic origin, in the case which has been referred to as turbulent behavior of a front between vortices and antivortices, the origin of the instability is not well understood. Fig. 1.11 represents the "turbulent" state observed in a sample of $YBa_2Cu_3O_{7-\delta}$ crystal. After applying a reversed field to a previously remanent state, a new domain of antivortices entering the sample from the edges annihilates with the already existing state with vortices. The boundary between the flux and anti-flux exhibits an irregular "meandering" behavior, in a temperature window between 47 and 80 K. The image represents the time development of this instability [24]. We will discuss in Chapter 3 this type of behavior and examine if the in-plane anisotropy could play a role in this phenomenon.

Chapter 2

Finger-like patterns

In this chapter we will focus on the finger-like patterns that characterise the magnetic flux distribution in a Nb thin film [13] and that are represented in Fig. 1.9 and Fig. 1.10. These fingers of vortices, that we have described in Chapter 1, have a well defined shape and a characteristic width that varies between 20-50 μm. The physical mechanism that underlies the development of an instability of a flat front between the vortex and the superconducting states into these narrow structures has been studied in recent theoretical models [19–21]. However, while in these earlier work the thermo-magnetic origin of the instability has been pointed out, the remarkably well defined shape of the fingers could not be obtained explicitly. In this chapter we will concentrate particularly on this growth form.

2.1 The sharp interface limit

A detailed analysis for the shape of the fingers requires a more tractable mathematical model than the ones proposed previously. In particular, since we are interested in the dynamics of the front between two phases, we need to reduce the problem to an interfacial description, in order to determine an explicit equation for the pattern curvature. The formulation of a local growth model for the vortex front is an effective method to analyse the dynamics

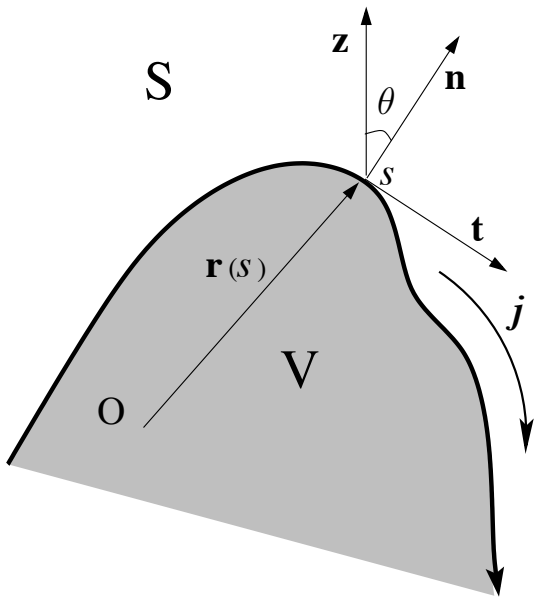

Figure 2.1: Schematic representation of a local growth model for an interface between a vortex and a superconducting phase (which are denoted by V and S respectively). Each point at the interface, that corresponds to the local arclength s, is defined by the angle θ between the normal vector $\mathbf{n}$ and a fixed direction $\mathbf{z}$ in the plane and the distance r from a fixed origin (O).

and the characteristics of the pattern in its essential features, without loosing the required accuracy for a realistic physical description.

Let us consider the general problem of a front propagation between two phases, in which we can define a continuous order parameter that vanishes in a relatively thin transition zone. In an interfacial formulation, or moving boundary approximation, the dynamics of the front is described by some boundary conditions for the physics at the interface, without taking into account explicitly the way in which the order parameter changes from one state to an other. This method is appropriate if the thickness of the interfacial region can be neglected in comparison to the typical length scale of the patterns. If this requirement is satisfied, the domain wall between the two phases is viewed as a sharp interface from the "outer" pattern forming length

scale, while the dynamics in the "inner" scale of the front is mapped into moving boundary conditions for the fields [54,55]. Local growth models have proven to be a useful tool to analyse front propagation in several physical systems, such as dendrites in crystal growth, viscous fingering, streamers, and also magnetic flux penetration in type I superconductors [31, 35–38, 56–58]. For example, in the case of dendrites at a solid-liquid interface, a boundary layer model is appropriate, since the width of the interface is of a few atomic distances, while the typical length scale at which the patterns form are of the order of microns. Therefore, the dynamics can be translated into some boundary conditions for the growth velocity of the front in terms of the local temperature [56].

In the case of a superconductor, we have already seen in the introduction that, according to the Ginzburg-Landau approach, the order parameter ψ vanishes at a normal-superconducting interface over a distance defined by the microscopic coherence length ξ. For a typical classical pure type I superconductor this is of the order of 0.1 μm. Therefore, there is a strong separation of scales between the domain size (typically of the order of 0.1 mm) and the width of the interface. This justifies the study of the front propagation through a moving boundary model in a type I superconductor, as was worked out by [35–38].

In the case of a type II superconductor, the transition zone between the vortex and superconducting state is of the order of the distance between vortices. For fields at which the experiments were performed, between 20 and 40 mT [13, 14], this is of the order of 0.3 μm, so it is much less than the typical scale of the patterns (0.1-1 mm). Moreover, for the fast-moving vortex fingers of [13], the thermal decay length can become quite significantly smaller than the width of the domain. We will give an explicit formula for this length in Section 2.2.3 (see 2.13). The vortex density and the temperature change rapidly in comparison with the radius of curvature of the front. As a consequence, the formulation of an interfacial description to describe finger-like patterns turns out to be an appropriate and accurate approach.

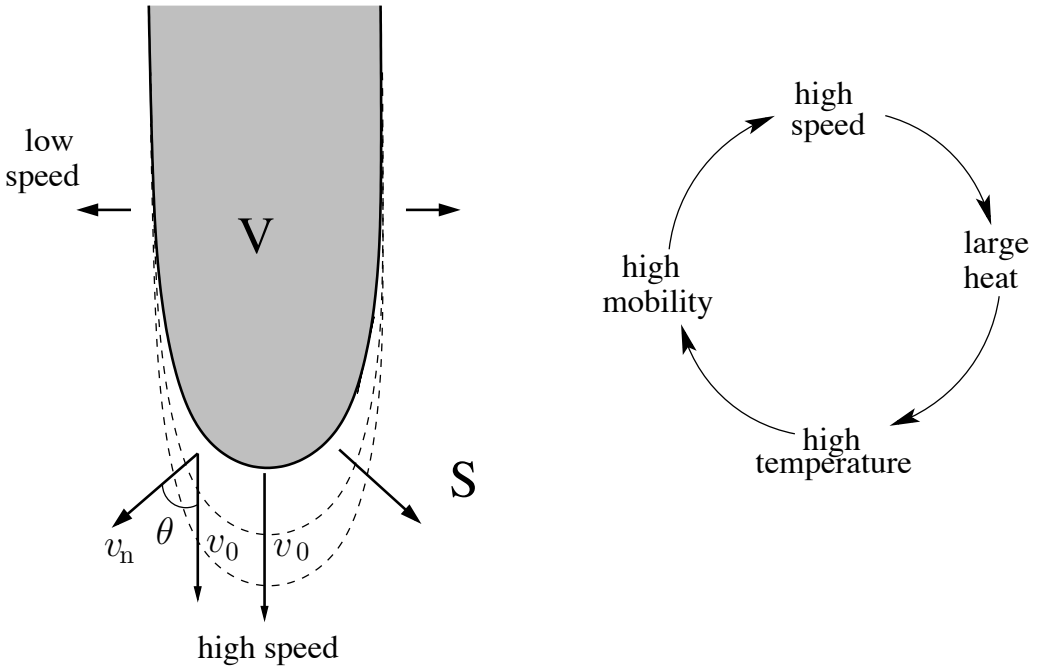

Figure 2.2: Scheme of the model that we propose: a finger-shaped domain of vortices (V) penetrating in a superconducting state (S) is characterised by a relatively high speed and mobility at the tip and low speed and mobility on the side. A higher speed gives rise to an enhanced mobility and therefore more heat is generated.

The physical picture that we propose for these finger-type patterns is that they are self-organised propagation shapes with a relatively higher speed and temperature at the tip and a lower speed and temperature on the sides, as schematised in Fig. 2.2. A higher speed leads to an enhanced mobility and therefore more heat is generated.

2.2 The model

2.2.1 The physical background and the geometry

We consider a thin film of thickness $d \approx \lambda$, which is in contact to a substrate at temperature T_0. The magnetic induction $\mathbf{B}$ is perpendicular to the plane of the film.

In our analysis we want to focus on vortex fronts that propagate with a shape-preserving form (as represented in Fig. 2.2) and, in particular, we aim to prove that there are solutions with finger-like shapes. Therefore, we concentrate on a situation in which a flat front has already developed into a non-uniform flux distribution. By assuming a domain of vortices with a constant density of magnetisation in the bulk (like in the droplet of Fig. 1.1(b)), the supercurrents that correspond to neighboring vortices cancel each other. We refer thus to a situation in which there is a macroscopic current j only along the edge of the domain, at the interface with the superconducting state, where the magnetic induction vanishes.

For a more realistic description one should account for a spatial dependent current that can be derived from the long range interaction between vortices, like in [11]. Since in successive experiments vortex fingers shoot into the sample at different positions, sample inhomogeneities do not appear to play an important role, so we ignore these here.

Figure 2.1 represents a scheme for a local growth model of a domain of vortices. In a sharp interface limit the front between the vortex and superconducting state is mapped into a one-dimensional curve. A point at the interface is defined by its arclength s, a position $\mathbf{r}(s)$ with respect to a fixed origin, the local Frenet-Serret frame of the tangent and normal vectors $(\mathbf{t}, \mathbf{n})$, and an angle $\theta(s)$ between the normal to the curve and the direction of propagation [31, 56]. The curvature of the interface is then defined by $\kappa(s) = \partial_s \theta$. We will adopt this geometrical construction as the starting point to develop our analysis of finger-like patterns in type II superconductors.

2.2.2 Basic equations for the front dynamics

For the dynamics of the vortices we consider a local dissipative motion with a viscosity η defined by the Bardeen-Stephen model that we have defined in (1.43) [50]. Vortices move in the direction normal to the interface with a normal velocity $v_{\rm n}(s) = \partial \mathbf{r}(s)/\partial t \cdot \mathbf{n}$ given by

$$\eta v_{\rm n}(s) = f(j, T_{\rm i}(s)) \frac{\phi_0 j}{c},\ \eta = \frac{B\phi_0}{\rho_{\rm f} c^2}, \tag{2.1}$$

where $T_{\rm i}$ is the temperature at the interface, $\rho_{\rm f} = \rho_{\rm n} B/B_{c2}$ is the flux flow resistivity and the function $f(j, T_{\rm i})$ gives the E-j characteristic through the the following dependence

$$E = \rho_{\rm f} f(j, T_{\rm i}) j. \tag{2.2}$$

We have generalised here the electric field-current density characteristic by considering a general function $f(j, T_{\rm i})$ that depends on the dynamical regime that one considers. The steepness of the electric field-current characteristic is an important feature in order to observe thermo-magnetic instabilities [9], as we have underlined in Sec. 1.7. Fingers and dendrites have indeed been observed as spontaneous phenomena only in a few materials such as Nb and MgB_2, contrary to $YBa_2Cu_3O_7$, where the application of a laser pulse is necessary to trigger the instability [16]. For the dynamics of vortices we take into account the two relevant regimes of flux flow and creep that we have described in Sec. 1.6. For $j \gg j_c$, in which the E-j characteristic becomes linear, $E \approx \rho_{\rm f}(j - j_c(T_{\rm i}))$. In the creep regime for $j < j_c$, the vortex motion is thermally activated, i.e. $E \approx \rho_{\rm f} \exp(U_0/T_{\rm i}(j/j_c(T_{\rm i}) - 1))$, with U_0 an activation barrier, as it is found by combining the relations (1.40) and (1.53) in the introductory chapter. We consider here the approximation used by [19] for the E-j relation: $E \approx \rho_{\rm f} \exp((j - j_c(T_{\rm i}))/j_1)$, with $j_1 \ll j_c$. In this expression the flux creep rate is independent on $T_{\rm i}$; as indicated in [53], the temperature independent j_1 is characteristic of low-T_c superconductors and depends mostly on pinning inhomogeneities.

The simplest approximation for the function $f(j, T_{\rm i})$ is thus to consider that vortices are pinned when j_c exceeds j. Thus $f(j, T_{\rm i})$ has a sharp break

at j_c as

$$f(j, T_\mathrm{i}) = 1 - \frac{j_c(T_\mathrm{i})}{j}, \text{ for } j \geq j_c(T_\mathrm{i}) \tag{2.3}$$

$$f(j, T_\mathrm{i}) = 0, \text{ for } j < j_c(T_\mathrm{i}). \tag{2.4}$$

We will refer to this as the discontinuous case. We consider a dependence of the pinning current on T_i as $j_c = j_0(1 - T_\mathrm{i}/T_c)$ where $j_0 = j_c(T_0)$. In reality the current-electric field characteristic is never so sharp, but instead continuous, thus a reasonable expression for the function $f(j, T_\mathrm{i})$, which interpolates between the two dynamical behaviors described above, is given by [19]

$$f(j, T_\mathrm{i}) = \frac{j_1}{j} \ln\left(1 + \exp\left(\frac{j - j_c(T_\mathrm{i})}{j_1}\right)\right). \tag{2.5}$$

In order to study the front dynamics, we have to take into account the coupling to the local temperature at the interface $T_\mathrm{i}(s)$, as given by (2.1). As we have already seen in the Section 1.7 related to thermomagnetic instabilities, the temperature $T(\mathbf{r})$ at a point $\mathbf{r}$ of the film is enhanced by the heat released due to joule effect; this is expressed by the product $\mathbf{E} \cdot \mathbf{j}$, as seen in (1.55). Moreover the system is coupled to a substrate kept at a temperature T_0, thus we also consider the relaxation of the temperature to T_0, as well as the diffusion process. Therefore, the temperature field $T(\mathbf{r})$ obeys the equation [19]

$$C\partial_t T(\mathbf{r}) = \nabla K \nabla T(\mathbf{r}) - (T(\mathbf{r}) - T_0)\frac{h}{d} + \mathbf{E}(j, T(\mathbf{r})) \cdot \mathbf{j}, \tag{2.6}$$

where C and K are the specific heat and thermal conductivity of the superconducting film, and h is an effective heat transfer coefficient for the heat loss to the substrate. The equation above considers the heat balance between the heat generation and loss like in (1.58) and, moreover, it takes into account the diffusion term. We consider a thin superconducting film, such that the temperature T varies slowly across the thickness, as we have already discussed in Chapter 1, in Sec. 1.7.

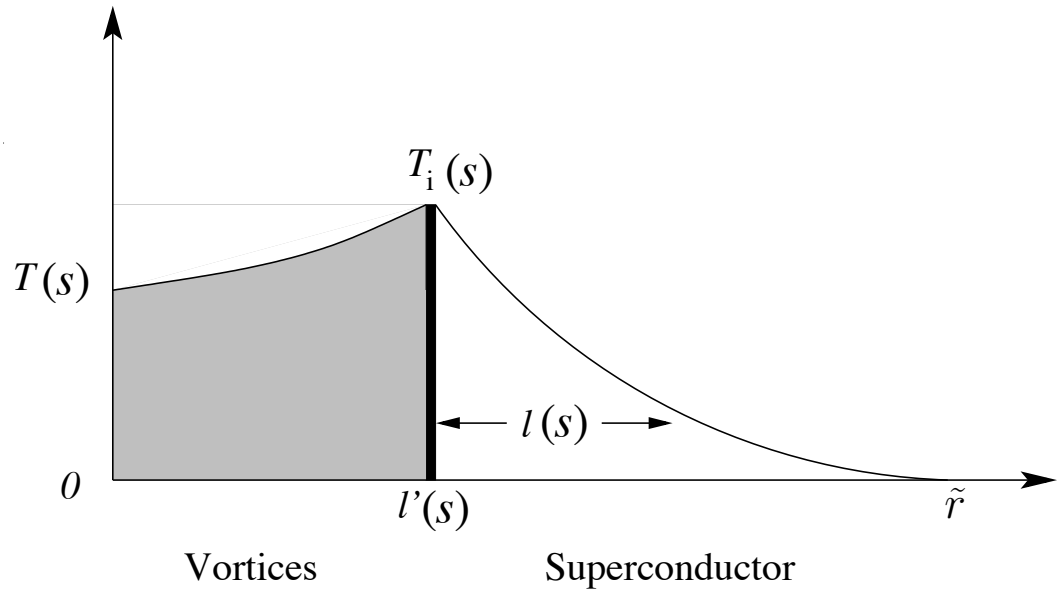

Figure 2.3: Scheme of the temperature $T(s, \tilde{r})$ versus the distance $\tilde{r}$ from the interface.

2.2.3 Interfacial formulation

The crux of our sharp interface approximation is the idea that we can characterise the temperature field in the system of local coordinates $(\mathbf{t}, \mathbf{n})$, $T(s, \tilde{r})$ with $\tilde{r}$ coordinate along the normal component, through an effective boundary layer thickness $l(s)$ with the following Ansatz [56]

$$T(s, \tilde{r}) = T_{\mathrm{i}}(s) \exp(-\tilde{r}/l(s)). \tag{2.7}$$

The integration Eq. (2.7) with respect to $\tilde{r}$ in the interval $[0, \infty]$ yields the heat content across the interface at a position s,

$$H(s) = \int_0^\infty T(s, \tilde{r}) d\tilde{r} = T_{\mathrm{i}}(s) l(s). \tag{2.8}$$

By expressing the diffusion term in the local coordinate system $(\mathbf{t}, \mathbf{n})$ and considering a co-moving frame, in the limit for a weakly curved interface $\kappa(s) \ll 1/l(s)$, Eq. (2.6) transforms into

$$C\partial_t T - v_{\mathrm{n}} \partial_{\tilde{r}} T = K(\partial_{\tilde{r}}^2 T + \kappa \partial_{\tilde{r}} T + \partial_s^2 T) - (T - T_0)\frac{h}{d} + \mathbf{E}(j, T) \cdot \mathbf{j}. \tag{2.9}$$

The term $\mathbf{E}(j, T(s,\tilde{r})) \cdot \mathbf{j}$ is non-zero only at the interface, for $\tilde{r} = 0$, where $T(s,\tilde{r}) = T_{\rm i}(s)$. The derivation of a moving boundary condition for the temperature at the interface $T_{\rm i}$ follows from the insertion of (2.7) into (2.9). Integrating (2.9) with respect to $\tilde{r}$ in the interval $[0, \infty[$, through the boundary layer leads to

$$\tau v_{\rm n}(s) = f(j, T(s))j \tag{2.10}$$

$$\begin{aligned}\partial_t(T(s)l(s)) = &-(v_{\rm n}(s) + \kappa(s))T(s) - T(s)l(s) \\ &+\alpha f(j,T)j^2 l(s) + \partial_s^2\left(l(s)T(s)\right).\end{aligned} \tag{2.11}$$

The first term on the right in the temperature equation derives from the co-moving frame and from the diffusion in the normal direction to the front, where the other terms represent respectively the relaxation to the substrate temperature, the heat due to dissipation, and the lateral diffusion. In the derivation of (2.11) we assumed that the partial derivative $\partial_{\tilde{r}} T(s,\tilde{r})$ vanishes both behind and ahead of the interface, as schematised in Fig. 2.3.

In this system of equations we have rescaled the variables by measuring the temperature $T_{\rm i}$ at the interface in units of $T = (T_{\rm i} - T_0)/(T_c - T_0)$, lengths in units of $L_{\rm h} = \sqrt{Kd/h}$, time in unit of $t_{\rm h} = Cd/h$, currents in units of of $j_c(0)$ and fields as $b \approx B/B_1$, $B_1 = (4\pi j_c(0) L_{\rm h})/c$. The only parameters that are left in the equations are thus the dimensionless number $\tau = 4\pi K/(\rho_{\rm n} c^2 C) b_{c2}$, which is essentially the ratio of the temperature diffusion constant and the vortex diffusion constant, and $\alpha = \rho_{\rm f} j_0^2 d/(h(T_c - T_0))$, which plays the role of a coupling constant for the heat source term. Let us estimate the units of our dimensionless variables and the constants that enter in the equations. Typical parameters for Nb thin films of [10], are $d \approx 0.5$ μm, while the resistance for the normal metal is $\rho_{\rm n} \approx 1.7 \times 10^{-6}\Omega$. Moreover, the electronic specific heat coefficient is $\gamma \approx 10^4$ ergs/cm^3 K ^{2}, thus the heat capacitance C is $C = \gamma T \approx 10^{-2}$ J/(cm$^3 K$) at a temperature $T_0 \approx 4K$. For the heat transfer coefficient h and conductivity K we can assume $h \approx 1$ W/(cm^2 K) and $K \approx 1$ W/(cm K). [9]. We thus estimate the characteristic length of our system as $L_{\rm h} \approx 70$ μm, and the time $t_{\rm h} \approx 10^{-6}$-$10^{-7}$ s.

The dimensionless constant α quantifies the ratio between the energy produced by joule dissipation and the heat loss to the substrate. In order to observe the instability, $\alpha \geq 1$ [9]. For a magnetic field $B \approx 20$ mT and $B_{c2} \approx 2$ T, a critical pinning current $j_c \approx 10^6$ A/cm^2 [10, 13], one finds $\alpha \approx 10\text{-}10^2$. As mentioned above, the parameter τ compares time scales for the magnetic field diffusion and the thermal diffusion. Using parameters estimated for a Nb thin film, we find $\tau \approx 10^{-1}\text{-}10^{-2}$, implying that the vortex flux density responds much faster to the inhomogeneities than the temperature. This justifies the picture of a sharp-edged domain of almost constant vortex density, whose motion is coupled to a temperature that decays within a boundary layer of thickness $l(s)$.

The boundary layer thickness is derived by solving the equation for the temperature in the direction normal to the front, in the approximation $\kappa(s) \ll l(s)^{-1}$. Since the temperature diffuses slowly in space with respect to the inner scale of the interface, we assume that the interfacial region $l'(s)$ where a sheet of current j is present is negligible with respect to the total boundary layer thickness related to the heat content. Therefore, in order to determine $l(s)$, we can use the equation for the temperature in the absence of the heat source $E \cdot j$. This idea is represented schematically in Fig. 2.3. By assuming a co-moving frame in which a point of the interface moves with a velocity $v_\mathrm{n}(s)$, the time derivative for $T(s, \tilde{r})$ transforms into $\partial_t T(s, \tilde{r}) = \partial_t T(s, \tilde{r})|_{\tilde{r}} - v_\mathrm{n}(s)\partial_{\tilde{r}} T(s, \tilde{r})$. For a straight front, the equation for the $T(s, \tilde{r})$ field is

$$-v_\mathrm{n}(s)\partial_{\tilde{r}} T(s, \tilde{r}) = \partial_{\tilde{r}}^2 T(s, \tilde{r}) - T(s, \tilde{r}). \tag{2.12}$$

The substitution of the Ansatz (2.7) leads finally to

$$l(s) = \frac{2}{v_\mathrm{n}(s) + \sqrt{v_\mathrm{n}(s)^2 + 4}}. \tag{2.13}$$

2.2.4 Equation for the shape-preserving front

Since we are interested in determining nontrivial finger-like front solutions, we concentrate on the problem of finding shape-preserving growth forms,

so that in time the whole shape simply translates with a velocity v_0 in the growth direction. This means that for any point on the interface we have (see Fig. 2.2)

$$v_{\mathrm{n}}(s) = v_0 \cos\theta(s). \tag{2.14}$$

For a finger-like domain of vortices, the velocity is largest at the tip, for $\theta = 0$, $v_{\mathrm{n}} = v_0$, where we assume that the normal Lorentz force has the same direction of the front propagation at the tip, whereas it vanishes on the side of the pattern for $\theta = \pi/2$. In the frame with a fixed angle θ we impose that the explicit time derivative vanishes, so that the fields are stationary,

$$\partial_t(T(s)l(s))|_\theta = 0. \tag{2.15}$$

The boundary layer approximation enables us to determine the shape of the uniformly translating finger shapes by reducing the problem into a single equation for the curvature of the front. Examining the relation between the time derivative in the coordinates system with respect to the normal front direction and the one with fixed angle θ and by inserting the expression above, we get

$$\begin{aligned} \partial_t(Tl)|_{\mathrm{n}} =& \partial_t(Tl)|_\theta - \kappa\partial_\theta v_{\mathrm{n}}\partial_\theta(Tl) \\ =& -\kappa\partial_\theta v_{\mathrm{n}}\partial_\theta(Tl). \end{aligned} \tag{2.16}$$

For the first equality in (2.16) we have used the fact that

$$\partial_t|_{\mathrm{n}} = \partial_t|_\theta + \partial_t\theta\partial_\theta, \quad \partial_t\theta = -\partial_\theta v_{\mathrm{n}}\partial_s\theta. \tag{2.17}$$

In the last equality for the time derivative of the angle θ in the equation we have used a relation from the theory of local growth models [59]. The combination of (2.16) together with (2.11, 2.13, and 2.14), leads to a non-linear second-order differential equation for the angle $\theta(s)$. We determine the solution both for the simplified form (2.4) for the function $f(j, T)$ and for the expression given by (2.5). In both cases the problem is reduced to solving a nonlinear equation of second order for $\theta(s)$. In analogy with the case of needle-crystal solutions in a solidification problem [56], we look for

a trajectory in the $\theta, \kappa, \zeta = \partial_s \kappa$ space, that starts at $\theta = 0$ with $\zeta = 0$, for symmetry, and moves to the fixed point $\theta = \pi/2$, $\kappa = 0$, $\zeta = 0$. Among all the trajectories, which correspond to different velocities v_0, and that flow to the fixed point, a steady-state solution with finger-shape is selected by imposing the proper boundary conditions based on physical considerations.

2.3 Solution for the sharp E-j characteristic

2.3.1 Derivation of the equation

In this section, we derive the solution for the simplified case with a discontinuous electric field-current characteristic. Let us consider the equation for the velocity of the front in (2.11) and $f(j, T)$ defined by (2.4)

$$\tau v_0 \cos(\theta(s)) = (j - (1 - T(s)), \quad j \geq (1 - T(s)), \tag{2.18}$$

$$\tau v_0 \cos(\theta(s)) = 0, \qquad j < (1 - T(s)). \tag{2.19}$$

From the last equation it follows that, for $j \leq (1 - T(s))$, $\theta(s) = \pi/2$. The form of $f(j, T)$ implies a discontinuity for the curvature $\kappa(s)$ of the interface, at a point s^* and a value $T(s^*) = 1 - j$, in the dimensionless variable for the temperature, such that $f(j, (T(s^*)) = 0$. This means that there is a sharp transition in the front dynamics at this point, since for $s > s^*$, vortices are pinned, and the curvature vanishes with $\theta = \pi/2$, whereas for $s \leq s^*$ the dynamical behavior is dominated by a flux flow regime. Therefore, we allow the curvature of the front to be discontinuous, but we have to impose the continuity of the physical temperature field together with its derivatives at s^*. From (2.18) we can derive $T(s)$ for $s \leq s^*$

$$T(s) = 1 - j + \tau v_0 \cos\theta(s), \tag{2.20}$$

and its derivatives

$$\partial_s T(s) = -v_0 \sin\theta(s)\kappa(s)\tau, \tag{2.21}$$

$$\partial_s^2 T(s) = -v_0 \cos\theta(s)\kappa(s)^2\tau - v_0 \sin\theta(s)\partial_s\kappa(s)\tau. \tag{2.22}$$

In the region in which the velocity of vortices vanishes ($j < (1 - T(s))$, in the absence of the heat source, from (2.11) we find that the temperature field decays exponentially to T_0. For $s > s^*$ thus the following relation holds

$$T(s) = T(s^*) \exp(s^* - s), \tag{2.23}$$

$$\partial_s^2 T(s) = \partial_s T(s) = T(s). \tag{2.24}$$

By combining the boundary conditions (2.24) with (2.21) and (2.22) at the matching point $s = s^*$, we derive two relations for the curvature κ and its derivative $\zeta = \partial_s \kappa$.

$$\kappa = \partial_s \kappa = \frac{1}{v_0 \tau}(1 - j). \tag{2.25}$$

Let us consider the different terms that enter in the equation (2.11). It is convenient to divide all terms by $l(s)$. The first contribution is therefore given by (see Eq. (2.16))

$$\frac{\kappa}{l} \partial_\theta v_\mathrm{n} \partial_\theta (Tl) = v_0 \sin\theta \left(\tau v_0 \kappa \sin\theta - \frac{v_0(1 - j + v_0 \tau \cos\theta)\kappa \sin\theta}{\sqrt{4 + v_0^2 \cos^2\theta}} \right). \tag{2.26}$$

The second term, which derives from the first term on the right in (2.11) (divided by l) is transformed into

$$(v_0 \cos\theta + \kappa)\frac{T}{l} = \frac{1}{2}(1 - j + \tau v_0 \cos\theta)\Big(v_0 \cos\theta + \sqrt{4 + v_0^2 \cos^2\theta} \Big)(v \cos\theta + \kappa). \tag{2.27}$$

A third term is given by the difference of the source heat term and the one related to the relaxation to the substrate temperature,

$$E \cdot j - T = \alpha v_0 \tau \cos\theta j - 1 + j - v_0 \tau \cos\theta. \tag{2.28}$$

Finally, the term related to the lateral diffusion gives

$$\frac{\partial_s^2(Tl)}{l} = \frac{\tau v_0}{(4+v_0^2\cos^2\theta)^{3/2}}\Bigg\{\Bigg[v_0^3\cos^4\theta - v_0^2\cos^3\theta + \Big(\tau^{-1}(j-1)+\sqrt{4+v_0^2\cos^2\theta}\Big) - v_0\Bigg(8+(\tau\sqrt{2})^{-1}(j-1) \sqrt{(8+v_0^2+v_0^2\cos(2\theta))}\Bigg)\sin^2\theta - v_0\cos^2\theta(-4+v_0^2\sin^2\theta) - \cos\theta\Bigg(4\Big(\tau^{-1}(j-1)+\sqrt{4+v_0^2\cos^2\theta}\Big) - v_0^2\Bigg(\tau^{-1}(1-j)+\sqrt{4+v_0^2\cos^2\theta}\Bigg)\sin^2\theta\Bigg)\Bigg](\partial_s\theta)^2 - \frac{1}{4}(8+v_0^2+v_0^2\cos(2\theta))\Big(2\tau^{-1}(j-1) - 2v_0\cos\theta+\sqrt{2(8+v_0^2+v_0^2\cos(2\theta))}\Big)\sin\theta\partial_s^2\theta\Bigg\}. \quad (2.29)$$

By substituting all the terms (2.26), (2.27), (2.28) and (2.29) into Eq. (2.11), one gets a nonlinear differential equation for the angle $\theta(s)$. The substitution of (2.25) into the equation for the angle θ yields also a relation for the current j as a function of v_0 and τ

$$\frac{1}{4v_0}(j-1)\left((j-1)^2v_0+4\tau^2v_0(v_0-2)+2\tau(j-1)(2+v_0+v_0^2)\right)=0. \quad (2.30)$$

This equation is satisfied for values of the current density j

$$j_0=1, j_\pm=\tau v_0^{-1}\left(-2-v_0+\tau^{-1}v_0-v_0^2\pm\sqrt{4+4v_0+13v_0^2-2v_0^3+v_0^4}\right). \quad (2.31)$$

The front solutions that we search are all the trajectories in the phase space defined by the angle θ, the curvature $\kappa=\partial_s\theta$, and its derivative $\zeta=\partial_s^2\theta$ and that satisfy the following system with the boundary conditions described

above

$$\begin{aligned}\kappa &= \frac{\partial\theta}{\partial s},\\ \zeta &= \frac{\partial\kappa}{\partial s},\\ \zeta &= F(\theta,\kappa,\zeta).\end{aligned} \tag{2.32}$$

The function $F(\theta,\kappa,\zeta)$ is reported in Appendix. Note that this equation indeed amounts to a highly nonlinear second order differential equation for θ, as it involves θ, $\partial_s\theta$, and $\partial_s^2\theta$. By restricting to the interval $[0,\pi/2]$, and shooting from $\theta = 0$, the relations (2.25) and (2.31) have to be satisfied. At $\theta = 0$ the prefactor of the highest derivative vanishes, and a second order equation for the curvature κ is determined

$$\begin{aligned}&\kappa^2 v_0\tau(4+v_0^2)^{-3/2}\left(-4v_0 - v_0^3 + 4\left(\tau^{-1}(j-1)+\sqrt{4+v_0^2}\right)\right.\\ &\left.+v_0^2\left(\tau^{-1}(j-1)+\sqrt{4+v_0^2}\right)\right) + \frac{1}{2}\big(1-j+v_0\tau\big)\big(v_0+\sqrt{4+v_0^2}\big)\kappa\\ &+\frac{1}{2}\big(1-j+v_0\tau\big)\big(v_0+\sqrt{4+v_0^2}\big)v_0 + 1 - j - \alpha j v_0\tau + v\tau = 0.\end{aligned} \tag{2.33}$$

The solution of (2.33) gives two different values for κ; there are therefore two possible trajectories for $\theta(s)$, but only one corresponds to a positive curvature. Moreover, only one of the three relations found for the current density gives a possible solution that matches with (2.25).

2.3.2 Results

By numerically solving the differential equations with a "shooting method" [61], in the interval $[0,\pi/2]$, through the imposition of the boundary conditions set above, a unique front velocity is selected.

Fig. 2.4, on the left, represents the profile of the angle $\theta(s)$ and of the interface temperature $T(s)$ as a function of the arclength s for the fixed parameters $\tau = 0.1$ and $\alpha = 3.7$. The value for the tip velocity, which is found with the shooting routine, is given by $v = 1.07$ in our dimensionless

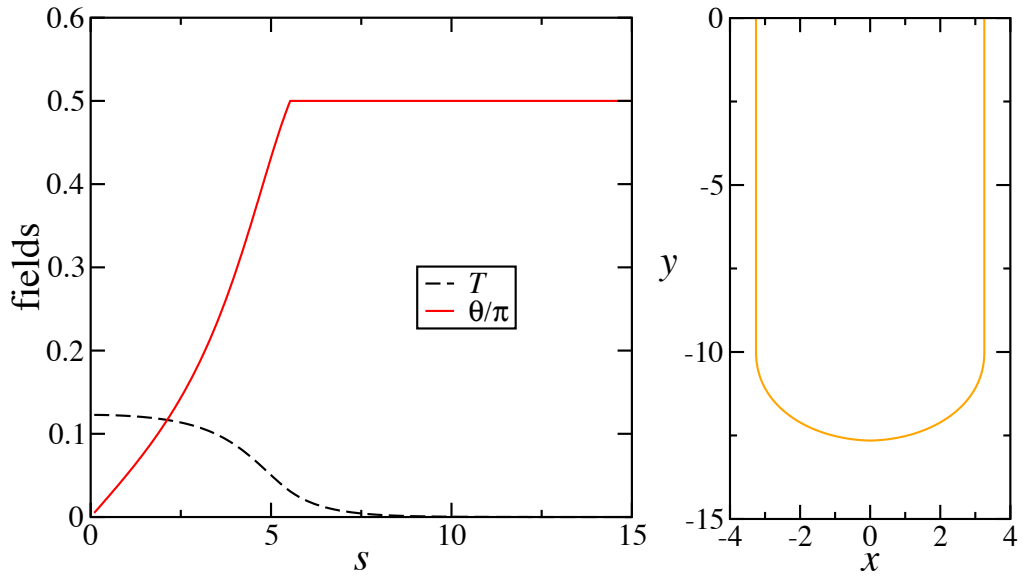

Figure 2.4: Plot of the profile of the angle θ and the temperature $T(s)$ as a function of the arclength s (on the left) and finger shape (on the right) for fixed parameters $\tau = 0.1$, $\alpha = 3.7$ and the value found for the tip velocity $v_0 = 1.07$.

units. As the figure shows, the temperature is larger at the tip of the front (for $\theta = 0$), where the mobility is maximal, whereas it decays to the substrate value on the side of the finger. We have found front solutions for a range between 2.8 and 4.2 for the dimensionless parameter α, and a fixed parameter $\tau = 0.1$. Fig. 2.4, on the right, represents the contour of the finger-like domain that corresponds to the profile $\theta(s)$.

In Fig. 2.5 we have plotted the values for the tip velocity v_0, as a function of α, which were derived from the shooting routine. The dependence of v_0 with respect to α is almost linear. The velocities that we have found are of the order of unity in our dimensionless coordinates, so of the order of $L_\mathrm{h}/t_\mathrm{h}$. By inserting our estimate for the units of length and time, L_h and t_h respectively, $L_\mathrm{h}/t_\mathrm{h} \approx 10^4$ cm/s. The experimental studies reveal that the dendritic and finger-shaped domains of vortices develop extremely fast, on a time scale that is even sometimes not accessible with the temporal resolution

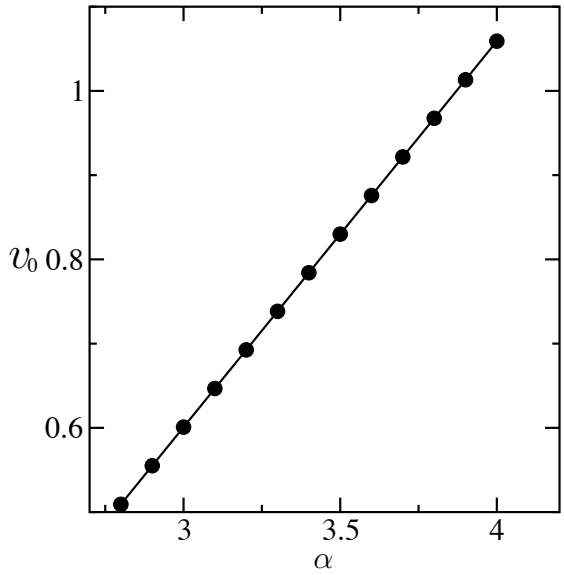

Figure 2.5: Plot of the values found for the tip velocity v_0 as a function of the coefficient α. The data refer to the result of the shooting routine.

of the technique. The velocity with which these patterns propagate, instead, is lower and could be measured in [16] for a sample of YBCO and in [12] for MgB_2. This was estimated as 10^4-10^5 cm/s. Our analytical estimate is thus of the same order of magnitude. Fig. 2.6 represents the shape of the fingers for different values of the coefficient α. In our geometrical model, each point at the interface is mapped into a one-dimensional curve in the x-y plane that represents the film, and is parametrised by the arclength s. The coordinates depend on the angle $\theta(s)$ through the formulas [60]

$$x(s) = \int_0^s \cos\theta(s')ds', \tag{2.34}$$

and

$$y(s) = y_0 - \int_0^s \sin\theta(s')ds', \tag{2.35}$$

where y_0 is chosen to ensure the origin of the center of the pattern.

As a conclusion of this section, we remark that, although the model with a sharp $f(j,T)$ that we have considered is based on a crude approximation

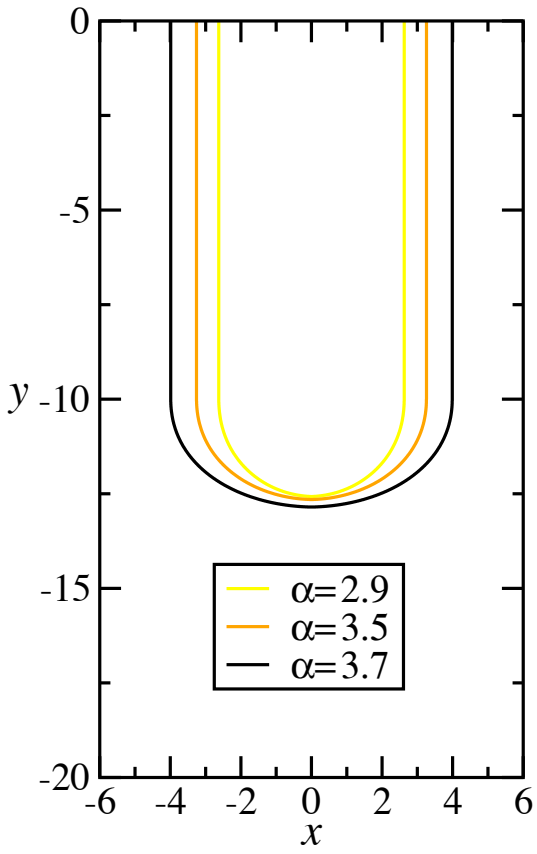

Figure 2.6: Finger shapes for different values of the coefficient α for the sharp E-j characteristics.

for the mobility of the vortices, it captures the characteristic shape of the fingers. Moreover, the front velocity in this case is uniquely selected, and was found in the typical range of the experiments. We could determine the solution only for a certain range of the parameter α. For this range we can give a first estimate of the width of the fingers; this, as one can see also from Fig. 2.4, in which the length scale is L_h, is larger than 4 $L_\mathrm{h} \sim 200$ μm. In the following section we will improve the model by considering the more realistic case with a smooth current-voltage characteristic.

2.4 Solution for the smooth E-j characteristic

2.4.1 Derivation of the equation

For the continuous function $f(j,T)$, which is defined in (2.5), the equation for the velocity in (2.11) transforms into

$$\tau v_0 \cos\theta = j_1 \ln\left[1+\exp\left(\frac{j-(1-T)}{j_1}\right)\right]. \tag{2.36}$$

From this equation, the following relation for T is derived

$$T = 1-j+j_1 \ln\Big[\exp\Big(\frac{\tau v_0\cos\theta}{j_1}\Big)-1\Big]. \tag{2.37}$$

It is easy to observe that, in the limit for $\theta \to \pi/2$, $T \to -\infty$. This divergence is a consequence of the description of the creep regime in terms of an activation barrier with a finite flux creep rate. This implies indeed that the velocity of the vortices at the boundary for $\theta \approx \pi/2$ vanishes exponentially as $v_0(\cos\theta) \approx \tau\exp((j-(1-T))/j_1)$. As a consequence, for a finite value of the flux creep rate, the vortex velocity becomes extremely small, but nonzero, so we integrate from $\theta = 0$ to $\theta = \theta_0 \approx \pi/2$.

In analogy with the case for the sharp mobility, an equation for θ is derived by computing all the terms in (2.11). The first contribution, that derives from the term on the left, is given by

$$\begin{aligned}\kappa\partial_\theta v_\mathrm{n}\frac{\partial_\theta(Tl)}{l} = &\frac{\tau\exp\left(\tau v_0\cos\theta/j_1\right)v_0^2\kappa\sin^2\theta}{\exp\left(\tau v_0\cos\theta/j_1\right)-1}\\ &-\frac{v_0^2\kappa\Big(1-j+j_1\ln\left(\exp\left(\tau v_0\cos\theta/j_1\right)-1\right)\Big)\sin^2\theta}{\sqrt{4+v_0^2\cos^2\theta}}.\end{aligned} \tag{2.38}$$

The other terms of Eq. (2.11) transform into the following expressions

$$\begin{aligned}(v_\mathrm{n}+\kappa)\frac{T}{l} = &\frac{1}{2}\Big(v_0\cos\theta+\sqrt{4+v_0^2\cos^2\theta}\Big)(v_0\cos\theta+\kappa)\\ &\left[1-j+j_1\ln\left(\exp\left(\frac{\tau v_0\cos\theta}{j_1}\right)-1\right)\right].\end{aligned} \tag{2.39}$$

$$Ej - T = \alpha j \tau v_0 \cos\theta - 1 + j - j_1 \ln\left(\exp\left(\frac{\tau v_0 \cos\theta}{j_1}\right) - 1\right). \qquad (2.40)$$

Finally, the last term which is related to the lateral diffusion is given by

$$\begin{aligned}
\frac{\partial_s^2(Tl)}{l} &= v_0\Bigg\{ - \frac{\tau \exp\left(\tau v_0 \cos\theta/j_1\right)}{\exp\left(\tau v_0 \cos\theta/j_1\right) - 1}\Bigg[(\partial_s\theta)^2\Bigg[\cos\theta + v_0 \sin^2\theta \\
&\left(\frac{\tau}{j_1\left(\exp\left(\tau v_0 \cos\theta/j_1\right) - 1\right)} + \frac{2}{\sqrt{4 + v_0^2\cos^2\theta}}\right)\Bigg] \\
&+ \sin\theta\partial_s^2\theta\Bigg] + 2v_0\Big(\frac{\sin^2\theta}{4 + v_0^2\cos^2\theta}\Big)(\partial_s\theta)^2 + \Bigg[1 - j \\
&+ j_1 \ln\left(\exp\left(\frac{\tau v_0 \cos\theta}{j_1}\right) - 1\right)\Bigg] - (4 + v_0^2\cos^2\theta)^{-3/2} \\
&\left[j - 1 - j_1 \ln\left(\exp\left(\frac{\tau v_0 \cos\theta}{j_1}\right) - 1\right)\right]\Big(v_0^2\cos^3\theta \\
&- v_0\sqrt{4 + v_0^2\cos^2\theta}\sin^2\theta + \cos\theta(4 + v_0^2\sin^2\theta)\Big)(\partial_s\theta)^2 \\
&- \big(4 + v_0^2\cos^2\theta\big)\sin\theta\partial_s^2\theta\Bigg\}. \qquad (2.41)
\end{aligned}$$

By substituting (2.38), (2.39), (2.40) and (2.41), in (2.11), a second-order nonlinear differential equation for θ is derived. The problem is now reduced to solving the system of equations

$$\begin{aligned}
\kappa &= \frac{\partial\theta}{\partial s}, \\
\zeta &= \frac{\partial\kappa}{\partial s}, \\
\zeta &= F_1(\theta, \kappa, \zeta). \qquad (2.42)
\end{aligned}$$

The function $F_1(\theta, \kappa, \zeta)$ is reported in Appendix. By following the same procedure for the case with a sharp $f(j, T)$, we integrate the equation from $\theta = 0$, where we impose for symmetry $\partial_s^2\theta = 0$. This boundary condition leads to a unique value for the curvature κ, that obeys the second order

differential equation

$$v_0\left(\frac{-j+1+j_1\ln\left(-1+\exp\left(\frac{\tau v_0}{j_1}\right)\right)}{\sqrt{4+v_0^2}}-\frac{\tau\exp\left(\frac{\tau v_0}{j_1}\right)}{\exp\left(\frac{\tau v_0}{j_1}\right)-1}\right)\kappa^2$$
$$+\frac{1}{2}\left[1-j+j_1\ln\left(-1+\exp\left(\frac{\tau v_0}{j_1}\right)\right)\right]\left(v_0+\sqrt{4+v_0^2}\right)(\kappa+v_0)$$
$$+1-j-\alpha j v_0\tau+j_1\ln\left(-1+\exp\left(\frac{\tau v_0}{j_1}\right)\right)=0. \tag{2.43}$$

From the two solutions for κ in the equation above, the positive value must be considered. By shooting in the space defined by the variables (θ,κ,ζ), from the point $(0,\kappa(0),0)$, the trajectory flows to the fixed point $(\pi/2,0,0)$. The fact that this is a fixed point for the system of equations (2.42) can be understood by expanding the last equation with respect to κ and $\omega=\cos\theta$. By retaining only linear terms in κ and ω, the last equation of (2.42) is expanded indeed as

$$\zeta=-\frac{\kappa^2}{w}-\kappa v. \tag{2.44}$$

If the first term on the right, κ^2/w converges to zero, in the limit for which ω and κ tend to zero, then $(\pi/2,0,0)$ is a fixed point for the original system (2.42). From our numerical analysis, the curvature κ vanishes linearly with ω, confirming that the results are consistent. Even if mathematically the trajectory flows to the fixed point, from the form of the equation, as we have already anticipated, we have to limit the range of integration up to angle θ_0 for which the temperature T is at the equilibrium value of the balance between the heat produced by joule effect and the one which is transferred to the substrate. Therefore, we impose the boundary condition that sets the angle θ_0

$$\alpha j\tau v_0\cos\theta_0-1+j-j_1\ln\left(\exp\left(\frac{\tau v_0\cos\theta_0}{j_1}\right)-1\right)=0. \tag{2.45}$$

Fig. 2.7 shows the dependence of the tip velocity v_0 as a function of the current density j, for a fixed value $j_1=10^{-2}$, $\theta_0=10^{-10}$, $\tau=10^{-1}$, as defined by the boundary condition above, in (2.45). The tip velocity v_0 depends strictly on the mobility of the front and thus to the temperature

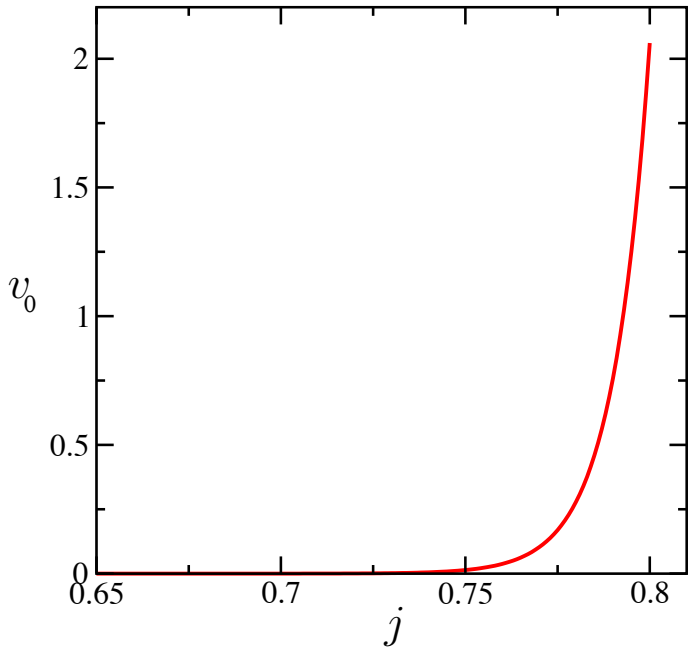

Figure 2.7: Plot of the tip velocity v_0 as a function of the density current j for a fixed value $\theta_0 = 10^{-10}$, $\tau = 10^{-1}$ and $j_1 = 10^{-2}$.

distribution. In particular, the temperature field is larger at the tip, for a lower pinning barrier. The tip velocity therefore has a much larger value than it would have at the substrate temperature (T$\sim$ 0). This can be derived easily from Eq. (2.36).

2.4.2 Results

Fig. 2.8 represents the comparison of the θ profile and the temperature distribution as a function of the arclength s, for the cases of discontinuous and continuous current-voltage characteristic respectively, with the same value of the tip velocity v_0 and current density j. As the plot shows, the curve related to the case with the smooth current-electric field relation $f(j, T_{\rm i})$ overlaps in the limit $j_1 \to 0$, with the one with a sharp function $f(j, T_{\rm i})$. The temperature field is larger at the tip, where vortices move faster and thus more heat is generated, whereas it vanishes as θ that approaches $\pi/2$.

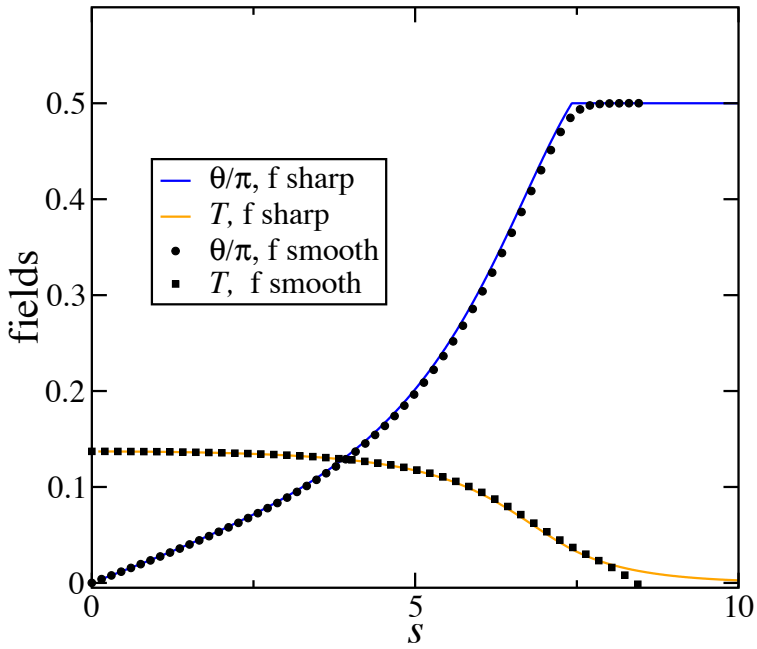

Figure 2.8: Comparison of the $\theta(s)$ and $T(s)$ fields profiles in the cases with discontinuous and continuous functions $f(j,T)$. The data correspond to the values $v_0 = 1.02$, flux creep rate $j_1 = 0.004$, $\alpha = 3.9$, $\tau = 0.1$, $j = 0.96$.

In Fig. 2.9 we represent instead the shape of the fingers for different parameters of the coefficient α and a fixed value of the velocity ($v_0 = 1.43$ in our units L_h/t_h) that corresponds to the typical order found in the experiments ($v_0 \approx 10^4 - 10^5$ cm/s). The width of the flux filaments for a correspondent current density $j \approx 0.92\ j_0$ varies in the range between $35 - 150$ μm for $\alpha = 9 - 20$, as it is shown in Fig. 2.10, in good agreement with the experimental studies for enough high values of α. According to the experiments, as the substrate temperature decreases, fingers get narrower. The dependence of the width on the coefficient α is consistent with this behavior. Indeed $j_c(T_0) = j_0(1 - T_0/T_c)$, implies that α is proportional to $(T_c - T_0)$. Thus, the fingers width decreases as α gets larger, in agreement with our results. Taking into account the physical mechanism that triggers the instability, we can interpret this behavior in these terms: for an enhanced heat dissipation,

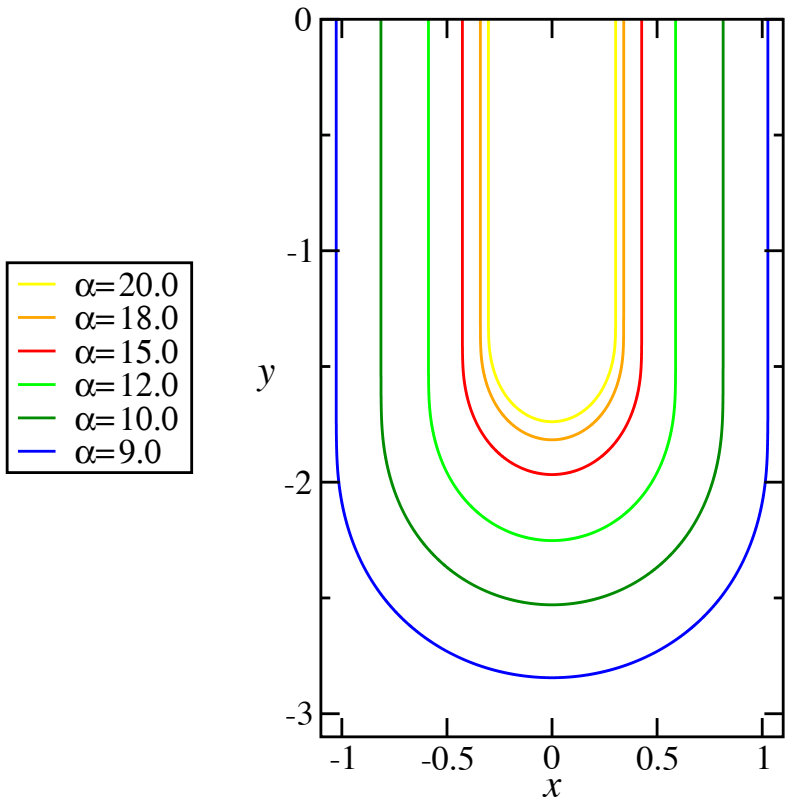

Figure 2.9: Fingers shapes in the case with smooth $f(j,T)$ for different values of the coefficient α for a velocity $v_0 = 1.43$ in our dimensionless variables, $j = 0.92$, $\tau = 10^{-1}$ and $j_1 = 0.004$.

vortices are driven faster due to the local thermo-magnetic instability in the direction in which the Lorentz force is maximal, thus, for the same amount of flux, the fingers are narrower. Too narrow fingers are however suppressed by thermal diffusion. This picture is also consistent with the linear stability calculations of [21].

Fig. 2.11 represents the data collapse of the profiles $\theta(s)$. Using the data of the width of the fingers with respect to the coefficient α, we have rescaled the arclength s. The curves almost overlap and this shows that the shape of the finger-like pattern is well defined. As α increases, the contour of the domain of vortices does not change significantely, but it maintains the same

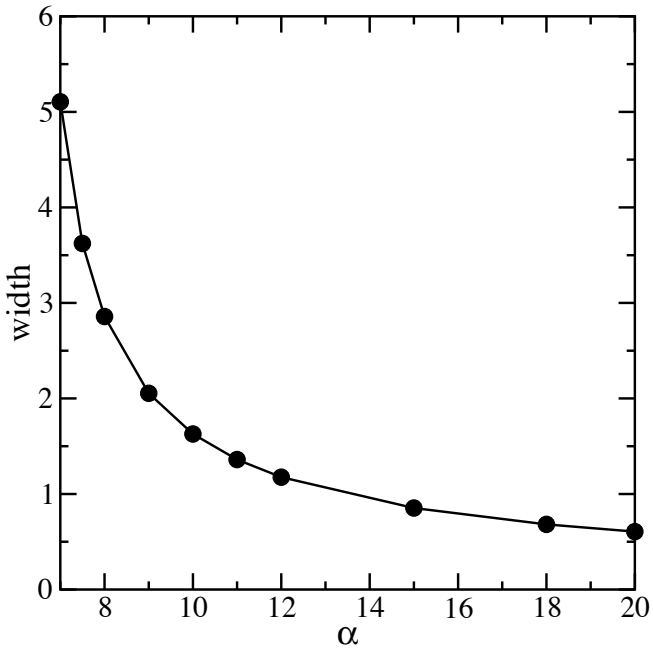

Figure 2.10: Plot of the width w of the fingers versus the coefficient α for parameter values of Fig. 2.9. The width is expressed in units of $L_{\rm h} \sim 70$ μm.

form.

2.5 Conclusions

In this work we have studied the finger-like shapes that were found in the recent experiments of [13]. The model that we have constructed is a novel type of approach to analyse these patterns and is based on the approximation of a sharp interface limit for the domain of vortices. A full analysis of the problem would require the treatment of the system of coupled equations (2.6) in a two-dimensional space, to show then that they admit a sharp-front behavior. In reality, this is impeded by the fact that the equations are too complicated to be studied analytically. In the previous work of [20, 21], the development and the dynamics of these patterns in the two-dimensional system of a thin film was examined numerically. The computations of [20] included also non-

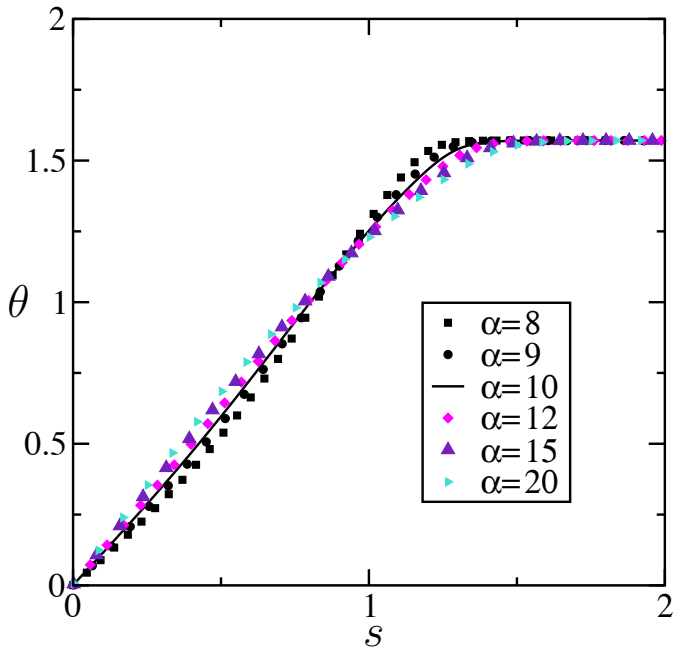

Figure 2.11: Data collapse of the $\theta(s)$ profiles in the case with smooth $f(j,T)$ for different values of the coefficient α for a velocity $v_0 = 1.43$ in our dimensionless variables, $j = 0.92$, $\tau = 10^{-1}$ and $j_1 = 0.004$.

local interactions, which we have instead neglected. Long-range forces are an important ingredient to study the interaction between the flux filaments. As observed in the experiments, fingers of vortices repel each other, as a consequence of the forces between the currents at the edge of the domains. We believe that, in analogy with the case of a type I superconductor [58], one could build up a model that takes into account the long-range forces between the current ribbons at the edge of each filament to analyse the dynamics of the magnetic flux distribution. Moreover, although it was observed experimentally that the patterns do not depend trivially on inhomogeneities, the presence of defects could play a role for the formation of dendrites. As it has been shown through the numerical simulations of [20], flux filaments can split and develop into branched-like structures in proximity of a defect.

We finally remark that for the smooth model we find a continuous family

of finger solutions, parametrised e.g. by v_0, the discontinuous model has only solutions for a particular velocity. This discrepancy can be interpreted as a consequence of the fact that a discontinuous function $f(j,T)$ implies a "fictitious" constraint for the velocity of the T field. From a more mathematical perspective, we expect that the introduction of a surface-tension type term in Eq. (2.1) could lead to the "selection" of a unique shape and velocity from the family of solutions in the smooth model, in analogy with the dendrites in crystal growth or viscous fingering. However, we believe it is a delicate open issue whether such surface tension type term would make sense for the vortex problem. First of all, the finger propagation is an extreme "out of equilibrium" problem. Secondly, even if could define a positive surface tension at the interface in analogy with the case between the solid and liquid phases [62], the long range repulsive interaction between vortices would indeed play the major role in the front dynamics. We will leave this issue for the future.

In conclusion, even if our approximate model could be improved by adding long-range forces or pinning defects, as we have discussed above, it captures the essence of the formation and characteristics of the thermo-magnetic instabilities with finger-like shape. By considering a sharp-interface limit for the vortex-front, we have proved that the shape of the fingers is well defined and we could estimate the scale of the width and show the qualitative dependence with respect to the substrate temperature. In addition, this is the first example of a boundary-layer model for a study of patterns of vortices in type II superconductors, and can be considered as a original contribution towards the understanding of these types of instabilities.

Chapter 3

Vortex-antivortex front

3.1 Introduction

3.1.1 Motivation

While the nucleation of finger-like patterns, as studied in Chapter 2, is clearly of thermo-magnetic nature, the origin of the "turbulent" behavior at the boundary between domains of magnetic flux and antiflux in a crystal of $YBa_2Cu_3O_{7-\delta}$, as represented in Fig. 1.11 in the introductory Chapter, is poorly understood. As we have introduced in Chapter 1, when the external magnetic field is reversed in a remanent state, vortices with flux of opposite sign, with respect to the already existing ones, penetrate in the superconducting material. In a certain temperature window, the boundaries between magnetic flux and antiflux corrugate and exhibit an irregular "meandering" behavior similar to the "turbulence" in a fluid.

An attempt to explain this phenomenon was made by Bass and coworkers [26] with a model based on a hydrodynamical approach for the fields related to the density of vortices and antivortices. In this work the dynamics was described essentially by a system of continuity equations, that involved also an annihilation term between vortices of opposite sign. Moreover, the coupling to the temperature field was included in the model and the instabil-

ity was attributed to the heat generated from the process of annihilation. The corrugation of an initially planar front was found to develop above a critical velocity, as a consequence of the core energy dissipated with the annihilation of a vortex-antivortex pair.

On the other hand, as was pointed out by Fisher *et al.* [27,28], in addition to the heat released in the process of annihilation, one should take into account also the heat due to the magnetic energy dissipated while vortices move. As we have seen in the previous chapters, this could play a relevant role in the front dynamics and induce an instability of thermo-magnetic origin.

Furthermore, while annihilation takes place only at the boundary of flux with opposite sign, the heat released by the dissipation of the magnetic energy is present in all the region where the magnetic flux has penetrated.

Fisher *et al.* [27, 28] propose an alternative interpretation, according to which the instability was not induced by a thermal effect but by the in-plane anisotropy of the sample [27, 28]. In this analysis, the hypothesis of a turbulent behavior induced by a Kelvin-Helmholtz type of effect was proposed. The Kelvin-Helmholtz instability is observed generally between two adjacent layers of fluids that are experiencing a different shear rate. Due to the shear at the boundaries, the flow can become unstable to small perturbations and convective patterns are formed [66].

The development of electromagnetic instabilities in the critical and resistive states due to the anisotropy of the material was already studied in [67,68]. In this analysis, it was shown that the non-collinearity between the electromagnetic field and the current could induce an unstable behavior of a front of vortices and lead to the formation of macrovortices. This study, however, does not apply specifically to the problem that we want to analyse, since we are considering the coexistence of vortices and anti-vortices and thus referring to a different system.

For a material with an *a-b* anisotropy, the lattice properties like the coherence length ξ and the penetration depth λ depend on the direction with respect to the principal axes of the crystal. Therefore also the mobility of

the vortices depends strictly on the direction of propagation. In a flux flow regime, this is indeed inversely proportional to the viscosity in the Bardeen-Stephen formula (1.43), which depends on ξ through the upper critical field H_{c2}. According to the experiments of [25], the crystal of $YBa_2Cu_3O_{7-\delta}$ in which the macroturbulence between flux of opposite sign was observed exhibits a small in-plane anisotropy and this was therefore suggested as the cause for the instability. In this Chapter we will concentrate on the issue whether this unstable behavior could arise in an anisotropic medium even in the absence of the coupling with the temperature of the sample.

There are several reasons to carefully reinvestigate the idea of an anisotropy-induced instability of propagating vortex-antivortex fronts. First of all, even though this mechanism was claimed to be relevant for the "turbulent" behavior at the boundaries of opposite flux regions, the critical anisotropy coefficients found on the basis of an approximation [27, 28] correspond to an anisotropy too high to describe a realistic situation, even when a nonlinear relation between the current and the electric field was considered [63–65]. Secondly, the calculation was effectively done for a symmetric stationary interface, rather than a moving one. Thirdly, even if the physical picture that has been advanced [27] for the anisotropy-induced instability is that of a shear-induced Kelvin-Helmholtz instability, it is not clear how far the analogy with the Kelvin-Helmholtz instability actually extends.

In order to try to settle the mechanism that underlines such phenomena, we will here investigate the linear stability of the interface between vortices and antivortices in the case where the front of vortices propagates with a *finite* velocity. We will perform an explicit linear stability analysis which shows that, in the presence of an in-plane anisotropy, vortex fronts with sufficiently large speed *are* stable in the absence of the coupling to the temperature. We shall see that the issue of the stability of fronts between vortices and antivortices is surprisingly subtle and rich: while we confirm the finding of Fisher *et al.* [27, 28] that stationary fronts have an instability to a modulated state, our moving fronts are found to be stable for all anisotropies. More-

over, our calculations indicate that the stability of such fronts depends very sensitively on the distribution of antivortices in the domain into which the front propagates, so it is difficult to draw general conclusions.

Besides the intrinsic motivation to understand this anisotropy issue, there is a second important motivation for this work. Our coarse-grained dynamics of the vortex densities is reminiscent of reaction-diffusion equations with nonlinear diffusion. More fundamentally, the dynamically relevant fronts in such equations with nonlinear diffusion are usually associated with nonanalytic (singular) behavior of the vortex densities; such singular behavior has been studied in depth for the so-called porous medium equation [69–71], which has a similar nonlinear diffusion. In the case we will study, the front corresponds to a line on one side of which one of the vortex densities is nonzero, while on the other side it vanishes identically. In the regime on which we will concentrate, this vortex density vanishes linearly near the singular line. But for other cases encountered in the literature [28, 72], even more complicated nonlinear dynamical equations arise that are reminiscent of reaction-diffusion type models in other physical systems. The case of bacterial growth models [73, 74] illustrates that the nonlinearity of the diffusion process can have a dramatic effect on the front stability, so a careful analysis is called for. In particular, in these cases, the proportionality of the diffusion coefficient to the gradient of the fields that propagate leads to an instability. A protrusion at the interface is indeed enhanced and grows larger and larger as a consequence of the increased diffusion, in analogy with the Mullins-Sekerka instability for crystal growth [29]. Nevertheless, in our case nonlinear diffusion by itself does not lead to an instability of the front, unlike in the bacterial growth case [74] or viscous fingering [31].

From a broader perspective, we see this work as a first step towards a systematic analysis of moving vortex fronts. The linear stability analysis which we will develop can equally well be applied to dynamical models which include the coupling to the temperature or in which the current-voltage characteristic is nonlinear, i.e. to continuum equations for the vortex density and

temperature which in the sharp interface limit should reduce to models like the one of Chapter 2. For this reason, we present the analysis in some detail for the relatively simple case where the vortex velocity is linear with respect to the magnetic field gradient and the current. Even then, as we shall see, the basic uniformly translating front solutions can still have surprisingly complicated behavior. We find that the density of vortices which penetrate the sample vanishes linearly for large enough front velocities, but with a fractional exponent for front velocities below some threshold value [75]. Since the latter regime appears to be physically less relevant, and since we do not want to overburden the study with mathematical technicalities, we will focus our analysis on the first regime. As stated before, in this regime we find that an anisotropy in the mobility without coupling to the temperature does not give rise to an instability of the flux fronts.

Our analysis will be aimed at performing the full stability analysis of the fronts in the coupled continuum equations for the vortex densities. Our procedure thus differs from the one of [27,28] in which a sharp interface limit was used.

As we have already seen in the previous chapters for the case of finger-like patterns, it is sometimes advantageous to map the equations onto a moving boundary effective interface problem, in which the width of the transition zone for the fields is neglected. One can in principle derive the proper moving boundary approximation from the continuum equations with the aid of singular perturbation theory. The analogous case of the bacterial growth fronts [74] indicates, however, that such a derivation can be quite subtle for nonlinear diffusion problems. Indeed it is not entirely clear whether the assumptions used in the sharp interface limit of [27,28] are fully justified. Also for this reason, we develop here an alternative and more rigorous stability analysis which allows for a systematic study on fronts in vortex dynamics.

3.1.2 The model

The physical situation that we have in mind refers to a semi-infinite slab in which there is an initial uniform distribution of vortices due to an external field **H** applied along the $\hat{z}$ direction. By reversing and increasing the field, a front of vortices of opposite sign penetrates from the edge of the slab. We will refer to the original vortices as antivortices with density n^-, and to the ones penetrating in after the field reversal as vortices with density n^+. In the region of coexistence of vortices and antivortices, annihilation takes place. Vortices are driven into the interior of the superconducting sample by a macroscopic supercurrent density **J** along the $\hat{y}$ direction due to the gradient in the density of the internal magnetic field. Flux lines then tend to move along the direction $\hat{x}$ transverse to the current under the influence of the Lorentz force on each vortex (1.39). We consider the regime of pure flux flow in which pinning can be neglected, while the viscous damping then gives rise to a finite vortex mobility. The inclusion of pinning in this model would lead to additional nonlinearities in the equations, e.g. through a nonlinear current-voltage characteristic of the form used in Chapter 2. Nevertheless, if the temperature changes are not taken into account, at the coarse-grained continuum level, these would still translate into equations with nonlinear diffusion of the same type as considered here. However, since we are mainly interested in capturing the essence of the instability, and verifying if a planar front is stable in the presence of an in-plane anisotropy, we limit our analysis to a regime, where the relation between the velocity and the current is linear. We believe, however, that most of our results do carry over to the more general case.

We follow a coarse-grained hydrodynamic approach in which the fields vary on a scale much larger than the distance between vortices. Since the magnetic flux penetrates in the form of quantized vortices, the total magnetic field in the interior of the slab can be expressed in a coarse graining procedure through the difference in the density of vortices and antivortices,

$$\mathbf{B} = (n^+ - n^-)\,\phi_0\,\mathbf{e_z}. \tag{3.1}$$

The dynamical equations for the fields of vortices and antivortices are simply the continuity equations

$$\begin{aligned}\frac{\partial n^+}{\partial t} &= -\nabla\cdot(n^+\,\mathbf{v}^+) - \frac{n^+n^-}{\gamma},\\ \frac{\partial n^-}{\partial t} &= -\nabla\cdot(n^-\,\mathbf{v}^-) - \frac{n^+n^-}{\gamma},\end{aligned} \tag{3.2}$$

where the second term on the right represents the annihilation between vortices of opposite sign. Since vortices annihilate in pairs, the total magnetic field B is conserved in the annihilation process. The velocity $\mathbf{v}$ is determined with the phenomenological formula for the flux flow regime according to (1.41)

$$\eta\mathbf{v}^{\pm} = \pm\,\mathbf{J}\times\frac{\phi_0}{c}\,\mathbf{e_z}, \tag{3.3}$$

where the Hall term has been neglected with good approximation for a case of a dirty superconductor [3]. The drag coefficient η is given by the Bardeen-Stephen model [50] that we have presented in the introduction and generally depends on the temperature of the sample. In this work we neglect the coupling to the temperature, but we will allow the mobility (the inverse of the drag) to be anisotropic. In passing, we also note that the above linear relation between the current density $\mathbf{J}$ and the flow velocity $\mathbf{v}^{\pm}$ is often generalized to a nonlinear dependence [28]. For simplicity, we do not consider this case here, but our method can be extended to such situations.

We can estimate the recombination rate γ^{-1} in (3.2) between vortices and antivortices as follows. Let us consider that we have a density n^- of antivortices in a background of vortices with density n^+. Near the interface where vortices and antivortices coexist, $n^+ \sim n^- \sim a^{-2}$, where a is the distance between vortices. Vortices and antivortices attract each other with a force given by $F = -\partial_r\mathcal{E}_{12}$, where $\mathcal{E}_{12}$ is the opposite of the energy calculated in (1.33), for vortices of the same sign. As we have seen in Chapter 1, in a slab, the interaction between vortices is screened at large distance r, and behaves as as $1/\sqrt{r}\exp(-r/\lambda)$ for $r > \lambda$, whereas, for $\xi \ll r < \lambda$, it has a logarithmic dependence. For large enough densities, $a < \lambda$. At a distance

$r \lesssim \lambda$, we can write the following equation,

$$\eta \frac{dr}{dt} = \frac{2\phi_0^2}{8\pi^2\lambda^2 r}, \quad r \lesssim \lambda. \tag{3.4}$$

By considering that an antivortex has then a vortex at a distance $a \sim (n^+)^{1/2}$ away, upon integrating the equation above for $r(t)$, between $r(0) = a$ and $r(\tau_{\rm ann}) = \xi$, we then get for the annihilation time

$$\tau_{\rm ann}^{-1} = \frac{\phi_0^2}{2\pi^2\lambda^2\eta(a^2 - \xi^2)} \sim \frac{\phi_0^2 n^+}{2\pi^2\lambda^2\eta}. \tag{3.5}$$

In the last equality above we have considered $a \gg \xi$. Since the last term in (3.2), represents the loss of vortices and antivortices due to the annihilation, this equivalence holds

$$\frac{n^-}{\tau_{\rm ann}} = \frac{n^+ n^-}{\gamma}. \tag{3.6}$$

Therefore, we can estimate the coefficient γ from (3.5) as

$$\gamma = \frac{2\pi^2\lambda^2\eta}{\phi_0^2}. \tag{3.7}$$

We stress that the above estimate is only correct for sufficiently large vortex densities, $n^{\pm}\lambda^2 \gtrsim 1$. For much lower densities, typically vortices and antivortices will annihilate much slower because of the exponential cutoff in the interaction. For low densities, the effective vortex annihilation rate $\tau_{\rm ann}^{-1}$ is therefore strongly suppressed. Secondly, one should keep in mind that vortices and antivortices move in opposite directions and the vortex annihilation time can become dominated by collision effects. However, for a continuum description, the densities of vortices can not be very low, so we can assume $a < \lambda$.

For a type II superconducting material with a Ginzburg-Landau parameter $\kappa \gg 1/\sqrt{2}$, the magnetization of the sample can be neglected, so that $\mathbf{B} \approx \mathbf{H}$. Then, by using the Maxwell equation (in which the term related to the displacement currents has been neglected with good approximation)

$$\mathbf{J} = \frac{c}{4\pi} \nabla \times \mathbf{B}, \tag{3.8}$$

together with (3.1) and (3.3), and substituting into (3.2), we get

$$\frac{\partial n^+}{\partial t} = D\,\nabla\cdot(n^+\,\nabla(n^+ - n^-)) - \frac{n^+ n^-}{\gamma}, \tag{3.9}$$

$$\frac{\partial n^-}{\partial t} = D\,\nabla\cdot(n^-\,\nabla(n^- - n^+)) - \frac{n^+ n^-}{\gamma}. \tag{3.10}$$

where the coefficient D is given by $D = \phi_0^2/(4\pi\eta)$. The situation that we will study in our analysis is the following. We consider a front of vortices which propagates into the superconducting slab from the left edge at $x = -L_x$ in the positive x direction. At $x = -L_x$, we impose the boundary condition that the density of vortices n^+ is ramped up linearly in time, $n^+(-L_x, t) = Rt$. This corresponds to the field going up linearly, just as in the Bean critical state [7]. We impose also that far right at $x \to \infty$, n^+ vanishes while n^- approaches a constant value n_∞. Through a rescaling of time and length variables, the coefficients of the equations (3.9) and (3.10) can be set to unity. In particular, it is convenient to rescale the time and length variables according to the following transformation

$$x \to \frac{x}{l_0}, \quad t \to \frac{t}{t_0} \quad n \to \frac{n}{n_\infty}, \tag{3.11}$$

where the length scale l_0 and the time scale t_0 are given by

$$l_0 = \sqrt{\frac{\phi_0^2\gamma}{4\pi\eta}} = \sqrt{\frac{\pi}{2}}\lambda, \tag{3.12}$$

$$t_0 = \frac{\gamma}{n_\infty} = \frac{2\pi^2\lambda^2\eta}{\phi_0^2 n_\infty} = \left(\frac{\lambda}{\xi}\right)^2 \pi\frac{a_\infty^2}{\rho_{\rm n}c^2}. \tag{3.13}$$

In the second equation above, we have substituted the viscosity coefficient which we have defined in (1.43) and we have expressed the upper critical field as $H_{c2} = \phi_0/2\pi\xi^2$. As one can see from (3.12), we measure variations in the densities at a scale of the order of the penetration depth λ. The unit of time t_0 is of the same order of the annihilation time in (3.5). By considering, for a sample of $YBa_2Cu_3O_{7-\delta}$, a resistivity of 10^{-16} s^{-1}, in Gaussian units, a penetration depth $\lambda \sim 20$ nm, a coherence length $\xi \sim 2$ nm and a initial uniform density for antivortices $n_\infty \sim a_\infty^{-2} \sim 10\ \lambda^{-2}$ for low fields, the unit

of time t_0 is estimated as $t_0 \sim \tau_{\rm ann} \sim 10^{-9}$-$10^{-10}$ s. As noted before, at very low vortex densities the effective annihilation time is strongly enhanced and thus the time scale becomes much larger than the value estimated above.

We will henceforth analyse the equations (3.9) and (3.10) with D= 1 and $\gamma = 1$. As we already mentioned before, and as we shall see in detail below, the above continuum equations have a mathematical singularity at the point where n^+ vanishes. Of course, in reality there can not be such a true singularity and our continuum coarse-grained model breaks down at scales of the order of the penetration depth. In particular, the derivative of the magnetic field and thus the current density $\mathbf{J}$ are not discontinuous with respect to the space variable, but they decrease continuosly at a scale given by the coherence length ξ. Effects which are neglected in the London approximation all play a role there, and the Ginzburg-Landau equation would provide a more appropriate starting point. Clearly, if the dynamical behavior of our continuum model would be very sensitively dependent on the nature of the singularity, then this would be a sign that the physics at this cutoff scale would really strongly affect the dynamically relevant long-wavelength dynamics. In practice, however, this is not the case. First of all, our method to do the linear stability analysis is precisely aimed at making sure that the singularities at the level of the continuum equations does not mix with the behavior or perturbations of the front region. Secondly, as we shall see, there are no instabilities on scales of the order of the microscopic cutoff provided by the coherence length ξ.

3.1.3 Outline

In our analysis, we first study a planar front which propagates with a steady velocity $\mathbf{v}$ along the x direction. By considering the propagation of the front in the co-moving frame, we get a system of ODE's for the vortex and antivortex density fields. The derivation of the uniformly translating solution is discussed in Section 3.2.1. As we will see, the profile that corresponds to the planar front for the density of vortices is singular. In particular, in the regime

on which we will focus, the derivative of the vortex density is discontinuous at the point where the field vanishes, while in the low-velocity regime there are higher order singularities. As a consequence of this nonanalytic behavior, the numerical integration of the equations has to be done with care near the singular point.

In Section 3.3, we perform a linear stability analysis of the planar solution. A proper Ansatz consists here of two contributions: a perturbation in the line of the singular front and a perturbation of the density field. As we will see, the presence of an in-plane anisotropy means that the (anti)vortex flow velocity is no longer in the same direction as the driving force acting on the (anti)vortices. Hence, contrary to the isotropic case, we have to consider a component of the velocity perpendicular to the driving force. The viscosity is thus represented by a non-diagonal tensor and depends on the angle between the direction of propagation of the front and the fast growth direction given by the anisotropy. By applying a linear stability analysis we get a system of equations for the fields representing the perturbation. Through a shooting method, and by matching the proper boundary conditions, we are then able to determine a unique dispersion relation for the growth rate of the perturbation. In Section 3.4 we treat the case of a stationary front, with a velocity $v = 0$. Contrary to the case of a moving front, no singularity in the profiles of the fields is present and the analysis can be carried out in the standard way.

3.2 The planar front

3.2.1 The equations and boundary conditions

In this section we analyse the planar uniformly translating front solutions $n^+ = n_0^+(x - vt)$, $n^- = n_0^-(x - vt)$ which are the starting point for the linear stability analysis in the next section. We refer to the system in a co-moving frame in which the new coordinate is traveling with the velocity v of the front, $\tilde{x} = x - vt$. The temporal derivative then transforms into $\partial_t|_x = \partial_t|_{\tilde{x}} - v\partial_{\tilde{x}}$.

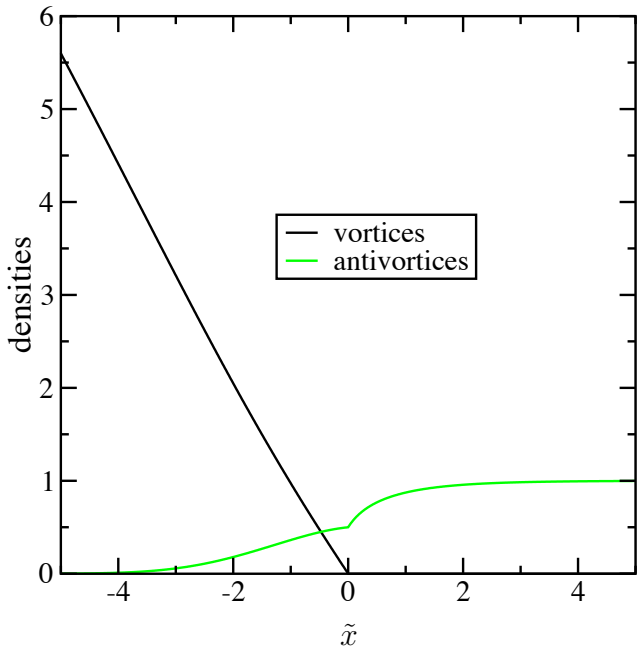

Figure 3.1: Profile of the planar front for the density of the vortices (n^+) and antivortices (n^-) for the case $v = 1$. Vortices and antivortices coexist in a thin transition region of the order of 4 $l_0 \sim 4\lambda$.

Since the front is uniformly translating with velocity v, the explicit time derivative vanishes. In the co-moving frame system, we consider $\tilde{x}$ to vary in the spatial interval $[-L, +\infty]$. The equations (3.9) and (3.10) become

$$-v\frac{dn_0^+}{d\tilde{x}} = \frac{d}{d\tilde{x}}n_0^+ \frac{d}{d\tilde{x}}(n_0^+ - n_0^-) - n_0^+ n_0^-, \tag{3.14}$$

$$-v\frac{dn_0^-}{d\tilde{x}} = \frac{d}{d\tilde{x}}n_0^- \frac{d}{d\tilde{x}}(n_0^- - n_0^+) - n_0^+ n_0^-. \tag{3.15}$$

This is a system of two ODE's of second order. Motivated by the physical problem we wish to analyse, the relevant uniformly translating front solutions obey the following boundary conditions at infinity

$$\begin{aligned} \lim_{\tilde{x}\to+\infty} n_0^- &= 1, & \lim_{\tilde{x}\to+\infty} \frac{dn_0^-}{d\tilde{x}} &= 0, \\ \lim_{\tilde{x}\to+\infty} n_0^+ &= 0, & \lim_{\tilde{x}\to+\infty} \frac{dn_0^+}{d\tilde{x}} &= 0. \end{aligned} \tag{3.16}$$

On the left, the density of vortices n^+ increases linearly with time with sweeping rate R. After a transient time, because of the annihilation process, the field n_0^- and its derivative vanish. The dynamical equation (3.14) for the n^+ field then yields

$$\frac{dn_0^+}{d\tilde{x}} = -v + \mathcal{O}\left(\frac{1}{n_0^+}\right), \quad \tilde{x} \to -\infty \tag{3.17}$$

i.e., we recover the well known critical state result [7] that in the absence of antivortices the penetrating n^+ field varies linearly with slope $-v$. Requiring that this matches the boundary condition $n^+(-L_x, t) = Rt$ for large times at $\tilde{x} = -L$ then immediately yields that $R = v^2$. One can easily derive that the density of antivortices decays with a Gaussian behavior on the left. By using indeed the relation (3.17) for large distances and substituting it in (3.15), we get

$$-2v\frac{dn_0^-}{d\tilde{x}} = \left(\frac{dn_0^-}{d\tilde{x}}\right)^2 + n_0^-\frac{dn_0^-}{d\tilde{x}} + n_0^-\left(v\tilde{x}\right). \tag{3.18}$$

Assuming that n_0^- and its derivatives are small, the first two terms on the right can be neglected and therefore this equation yields

$$n_0^- \approx Ae^{-\tilde{x}^2/4}. \tag{3.19}$$

Since the analysis of the planar front profiles and of their stability is naturally done in the co-moving $\tilde{x}$ frame, we will in practice use a semi-infinite system in the $\tilde{x}$ frame, and impose as boundary conditions at $\tilde{x} = -L$

$$\begin{aligned} &\lim_{\tilde{x}\to -L} n_0^- = 0, && \lim_{\tilde{x}\to -L} \frac{dn_0^-}{d\tilde{x}} = 0, \\ &\lim_{\tilde{x}\to -L} n_0^+ = \text{const} \gg 1, && \lim_{\tilde{x}\to -L} \frac{dn_0^+}{d\tilde{x}} = -v. \end{aligned} \tag{3.20}$$

Of course, in any calculation we have to make sure that L is taken large enough that the profiles $n_0^\pm$ have converged to their asymptotic shapes.

3.2.2 Singular behavior of the fronts

Effectively, Eqs. (3.9-3.10) and (3.14-3.15) have the form of diffusion equations whose diffusion coefficient vanishes linearly in the densities n^+ and n^-.

As already mentioned before, it is well known, from e.g. the porous medium equation [69–71], that such behavior induces singular behavior at the point where a density field vanishes (see e.g. Ref. [54]). Because we are looking at fronts moving into the region where $n^+ = 0$, in our case the singularity is at the point where the n^+ density vanishes. Let us choose this point as the origin $\tilde{x} = 0$. Then the relevant front solutions have $n^+(\tilde{x}) = 0$ for all $\tilde{x} > 0$, see Fig. 3.1, so the fields n^+ has compact support.

Because $n_0^-(0) \neq 0$, the prefactor of the highest derivative in the n^- equation does not vanish at $\tilde{x} = 0$, and hence one might naively think that n^- is nonsingular at this point. However, because of the coupling through the diffusion terms, this is not so. By integrating Eq. (3.15) over an interval centered around $\tilde{x} = 0$ and using that the field values n_0^+ and n_0^- are continuous, one immediately obtains that

$$\lim_{\Delta\tilde{x}\to 0} \left(\frac{dn_0^+}{d\tilde{x}} - \frac{dn_0^-}{d\tilde{x}} \right) \Bigg|_{-\Delta\tilde{x}}^{\Delta\tilde{x}} = 0. \tag{3.21}$$

Physically, this constraint expresses the continuity of the derivative of the coarse-grained magnetic field (3.1). Mathematically, it shows that any singularity in n_0^+ induces precisely the same singularity in n_0^-: to lowest order the two singularities cancel. Fig. 3.1 illustrates this: one can clearly discern a jump in the derivative of n_0^- at the point where n_0^+ vanishes with finite slope.

Before we analyse the nature of the singularity in more detail, we note that because of the nonanalytic behavior at $\tilde{x} = 0$, it is necessary to analyse the region $\tilde{x} < 0$ where $n_0^+ \neq 0$ separately from the one at $\tilde{x} > 0$ where $n_0^+ = 0$. In the latter regions, the equations simplify enormously, as the remaining terms in Eq. (3.15) can be integrated immediately. Upon imposing the boundary conditions (3.16) at infinity, this yields

$$\frac{dn_0^-}{d\tilde{x}} = -v\frac{(n_0^- - 1)}{n_0^-}, \quad \tilde{x} > 0. \tag{3.22}$$

Let us now analyse the nature of the singularity at $\tilde{x} = 0$. As the effective diffusion coefficient of the n^+-equation is linear in n^+, analogous situations

in the porous medium equation suggest that the field n^+ vanishes linearly. This motivates us to write for $-1 \ll \tilde{x} < 0$

$$\begin{aligned} n_0^+(\tilde{x}) &= A_1^+\tilde{x} + A_2^+\tilde{x}^2 + \cdots, \\ n_0^-(\tilde{x}) &= A_1^-\tilde{x} + A_2^-\tilde{x}^2 + \cdots + n_{\rm an}^-(\tilde{x}), \end{aligned} \tag{3.23}$$

where $n_{\rm an}^-(\tilde{x})$ is the analytic function which obeys Eq. (3.22) for *all* $\tilde{x}$. Clearly, the continuity condition (3.21) immediately implies

$$A_1^+ = A_1^-. \tag{3.24}$$

If we now substitute the expansion (3.23) with (3.24) into Eq. (3.14) for n_0^+ we get by comparing terms of the same order

$$\begin{aligned} \mathcal{O}(1): &\quad A_1^+(v - n_{\rm an}^{-\prime}) = 0, \\ \mathcal{O}(\tilde{x}): &\quad 4(A_2^+ - A_2^-) - 2n_{\rm an}^{-\prime\prime} - n_{\rm an}^- = 0. \end{aligned} \tag{3.25}$$

Here $n_{\rm an}^{-\prime} = dn_{\rm an}^-/d\tilde{x}|_{\tilde{x}=0}$, etc. Likewise, if we substitute the expansion into Eq. (3.15) for n_0^-, we get

$$\mathcal{O}(1): \quad 2vA_1^- - 2n_{\rm an}^-(A_2^+ - A_2^-) = 0, \tag{3.26}$$

since the term of order unity involving $n_{\rm an}^-$ cancels in view of (3.22). Higher order terms in the expansion determine the coefficients A_2^+ and A_2^-, and other terms like $A_3^\pm$ separately, but are not needed here. Together with (3.22), the above equations (3.25-3.26) immediately yield

$$\begin{aligned} n_{\rm an}^{-\prime} &= v, \\ n_{\rm an}^-(0) &= 1/2, \\ A_1^+ = A_1^- &= -v + \frac{1}{16v}. \end{aligned} \tag{3.27}$$

There are two curious features to note about the above result. First of all, n_0^+ always vanishes at the point where n_0^- is half of the asymptotic value n_∞ at infinity. Secondly, note that A_1^+ is negative for $v \geq 1/4$ and positive for $v < 1/4$. Since the vortex density n^+ has to be positive, we see that

these uniformly translating front solutions can only be physically relevant for $v \geq 1/4$.

Since the front velocity in this problem is not dynamically selected but *imposed* by the ramping rate $R = v^2$ at the boundary, we do expect physically realistic solutions with $v < 1/4$ to exist. In fact, it does turn out that in this regime the nature of the singularity changes: instead of vanishing linearly, n_0^+ vanishes with a v-dependent exponent. Indeed, if we write for $-1 \ll \tilde{x} < 0$

$$n_0^+(\tilde{x}) = |\tilde{x}|^\alpha (A_1^+ + A_2^+ \tilde{x} + \cdots), \tag{3.28}$$

$$n_0^-(\tilde{x}) = |\tilde{x}|^\alpha (A_1^- + A_2^- \tilde{x} + \cdots) + n_{\text{an}}^-(\tilde{x}), \tag{3.29}$$

and substitute this into the equations, then, in analogy with the result above, we find

$$\begin{aligned} n_{\text{an}}^{-\prime} &= v, \\ n_{\text{an}}^-(0) &= 1/2, \\ A_1^+ &= A_1^-, \\ \alpha &= \frac{1}{8v^2} - 1 > 1, \quad (v < 1/4), \end{aligned} \tag{3.30}$$

while again for $\tilde{x} > 0$ n_0^+ vanishes. A singular behavior with exponent depending on the front velocity v is actually quite surprising for such an equation [75]. However, one should keep in mind that this behavior is intimately connected with the initial condition for the n^- vortices. If one starts with a case where n^- does not approach a constant asymptotic limit on the far right, but instead increases indefinitely, one will obtain solutions where n^+ vanishes linearly. For this reason, and in order not to overburden the analysis with mathematical technicalities, we will from here on concentrate the analysis on the regime $v \geq 1/4$.

Since our study will limit the stability analysis to fronts with velocity $v \geq 1/4$ in our dimensionless variables, let us check how the scale that we consider relates with the realistic values of flux flow velocities. By considering

relations (3.11) the velocities are measured in units of

$$v_0 = \frac{l_0}{t_0} = \sqrt{\frac{1}{2\pi}}\lambda \left(\frac{\xi}{\lambda}\right)^2 \frac{\rho_{\rm n} c^2}{a_\infty^2}. \tag{3.31}$$

where we have expressed the viscosity η in terms of the upper critical field $H_{c2} = \phi_0/2\pi\xi^2$, and the normal state resistivity $\rho_{\rm n}$ using [50]. Inserting the estimated values that we have calculated for l_0 and t_0 in Sec. 3.1.2, we measure velocities in units of 10^4 cm/s. Therefore our model is valid at high flux flow velocities, for a scale of the order or larger than 10^4 cm/s. This is consistent with the fact that we have used a linear current-voltage relation, for large currents and large velocities in the regime of flux flow.

3.2.3 Planar front profile

At first glance, the equations look like two coupled second order equations. However, there is more underlying structure due to the fact that the annihilation term does not affect the difference $n^+ - n^-$. In order to integrate the set of equations (3.14-3.15), it is convenient to consider the following transformations in the variables related to the sum and difference of the density fields

$$\begin{aligned} D =& n^+ - n^-, \\ S =& n^+ + n^-. \end{aligned} \tag{3.32}$$

In these variables, the equations for the planar front become

$$-v\frac{dD_0}{d\tilde{x}} = \frac{d}{d\tilde{x}} S_0 \frac{dD_0}{d\tilde{x}}, \tag{3.33}$$

$$-v\frac{dS_0}{d\tilde{x}} = \frac{d}{d\tilde{x}} D_0 \frac{dD_0}{d\tilde{x}} - \frac{S_0^2 - D_0^2}{2}. \tag{3.34}$$

By numerically integrating (3.33-3.34) and looking for the solutions which satisfy the boundary conditions above, we obtained the uniformly translating front solutions. Fig. 3.1 illustrates the planar profile for $v = 1$. As one can observe, the region where vortices and antivortices coexist is a thin transition

zone of the order of $\Delta x \sim 4\ \lambda$, thus of the order the penetration depth. The fact that vortices and antivortices coexist is due to the finite annihilation time, as we have seen in Sec. 3.1.2. As one can observe, the profile is singular at the point where the density of the n^+ field vanishes linearly, in agreement with the earlier analysis.

Because of this singularity, the numerical integration of the set (3.33-3.34) is quite nontrivial. In particular, because of the discontinuity in the derivative of the n^+ field, the system (3.33-3.34) effectively needs to be solved only in the interval $[-L, 0[$, as the matching to the behavior for $\tilde{x} > 0$ has already been translated into the boundary conditions (3.27). The first equation can be straightforwardly integrated and by combining it with the second, the set reduces to

$$\begin{aligned}\frac{dD_0}{d\tilde{x}} =& \frac{-v(D_0+1)}{S_0},\\ \frac{dS_0}{d\tilde{x}} =& \frac{S_0(v(2D_0+1))\dfrac{dD_0}{d\tilde{x}} + (S_0^4 - S_0^2 D_0^2)/2}{vS_0^2 + (v(D_0^2+D_0))}.\end{aligned} \tag{3.35}$$

One can easily verify that in this formulation, the expression on the right hand side is indefinite at the singular point $\tilde{x} = 0$, as both the terms in the numerator and denominator vanish. In order to evaluate the expression, it is then necessary to perform an expansion of the numerator and denominator around the critical point values $S_0 = -D_0 = n_\infty/2$. From such an analysis one can then recover the relations (3.27) which we previously obtained from a straightforward expansion of the original equations. Numerically, we integrate the equations by starting slightly away from the singular point with the help of the results from the analytic expansion.

3.3 Dynamics in the presence of anisotropy

3.3.1 Dynamical equations

As mentioned before, we are interested in the effect that an anisotropy in the vortex mobility could have on the stability of the front.

In a material characterised by an in-plane anisotropy, the effective viscous drag coefficient depends on the direction of propagation of the front. More precisely, the mobility defined in (3.3) then becomes a non-diagonal tensor. This leads to a non-zero component of the velocity v perpendicular to the driving Lorentz force. We want to investigate whether the non-collinearity between the velocity and the force is responsible for an instability of the flux-antiflux interface. In the presence of anisotropy, the phenomenological formula (3.3) then has to be replaced by

$$\mathbf{v} = \hat{\eta}^{-1}\mathbf{F} = \Gamma\, R^{-1} \begin{pmatrix} 1 & 0 \\ 0 & \alpha \end{pmatrix} R\,\mathbf{F}, \tag{3.36}$$

where Γ is a constant, α represents the anisotropy coefficient and R is the rotation matrix corresponding to an angle θ between the direction of propagation of the front x and the principal axes x' of the sample. The coefficient α varies in the range [0,1] with the limiting case of infinite anisotropy corresponding to $\alpha \to 0$. For $\alpha = 1$ the isotropic case is recovered. The matrix $\hat{\eta}^{-1}$ is given in particular by

$$\hat{\eta}^{-1} = \Gamma \begin{pmatrix} \cos^2\theta + \alpha \sin^2\theta & \cos\theta \sin\theta(1-\alpha) \\ \cos\theta \sin\theta(1-\alpha) & \alpha\cos^2\theta + \sin^2\theta \end{pmatrix}, \tag{3.37}$$

The dynamical equations for the fields n^+ and n^- in the presence of anisotropy generalize to

$$\begin{aligned} \frac{\partial n^\pm}{\partial t} =& \frac{\partial}{\partial x}\left(n^\pm \frac{\partial}{\partial x}\left(n^\pm - n^\mp\right)\right) + p\frac{\partial}{\partial y}\left(n^\pm \frac{\partial}{\partial y}\left(n^\pm - n^\mp\right)\right) \\ &+ k\frac{\partial}{\partial x}\left(n^\pm \frac{\partial}{\partial y}\left(n^\pm - n^\mp\right)\right) + k\frac{\partial}{\partial y}\left(n^\pm \frac{\partial}{\partial x}\left(n^\pm - n^\mp\right)\right) - n^+ n^-, \end{aligned} \tag{3.38}$$

where the length and time variables have been rescaled and the elements k and p depend on the angle θ through the formulas

$$k = \frac{\cos\theta \sin\theta(1-\alpha)}{\cos^2\theta + \alpha \sin^2\theta}, \quad p = \frac{\alpha\cos^2\theta + \sin^2\theta}{\cos^2\theta + \alpha\sin^2\theta}. \tag{3.39}$$

Starting from an initially planar profile derived in Section 3.2.1, we want to study the dynamics of the front of vortices and antivortices by performing an explicit linear stability analysis on equation (3.38).

3.3.2 The linear stability analysis

As we have already mentioned in earlier sections, our linear stability analysis differs from the standard one, due to the presence of a singularity. The type of perturbation that we want to consider should not only involve the profile in the region where n^+ vanishes, but should also in particular involve the geometry of the front. In other words, as Fig. 3.2 illustrates, we want to perturb also the location of the singular line at which the density n^+ vanishes. As discussed in more detail in [74], the proper way to implement this idea is to introduce a modulated variable

$$\zeta(\tilde{x}, y, t) = \tilde{x} + \epsilon e^{iqy+\omega t+i\Omega t}, \tag{3.40}$$

and then to write the densities in terms of this "co-moving" modulated variable. Of course, the proper coordinate is the real variable $\mathrm{Re}\,\zeta$. However, when we expand the functions in Fourier modes and linearize the dynamical equations in the amplitude ε, each Fourier mode can be treated separately. Thus, we can focus on the single mode with wavenumber q and amplitude ϵ and then take the real part at the end of the calculation. The profiles of the fields n^+ and n^- are now perturbed by writing

$$n^+(\zeta, y, t) = n_0^+(\zeta) + \epsilon(n_1^+ + in_2^+)(\zeta)e^{iqy+\omega t+i\Omega t}, \tag{3.41}$$

$$n^-(\zeta, y, t) = n_0^-(\zeta) + \epsilon(n_1^- + in_2^-)(\zeta)e^{iqy+\omega t+i\Omega t}, \tag{3.42}$$

where n_0^+ and n_0^- are simply the planar front profiles determined before. Note that since we write these solutions as a function of the modulated variable ζ,

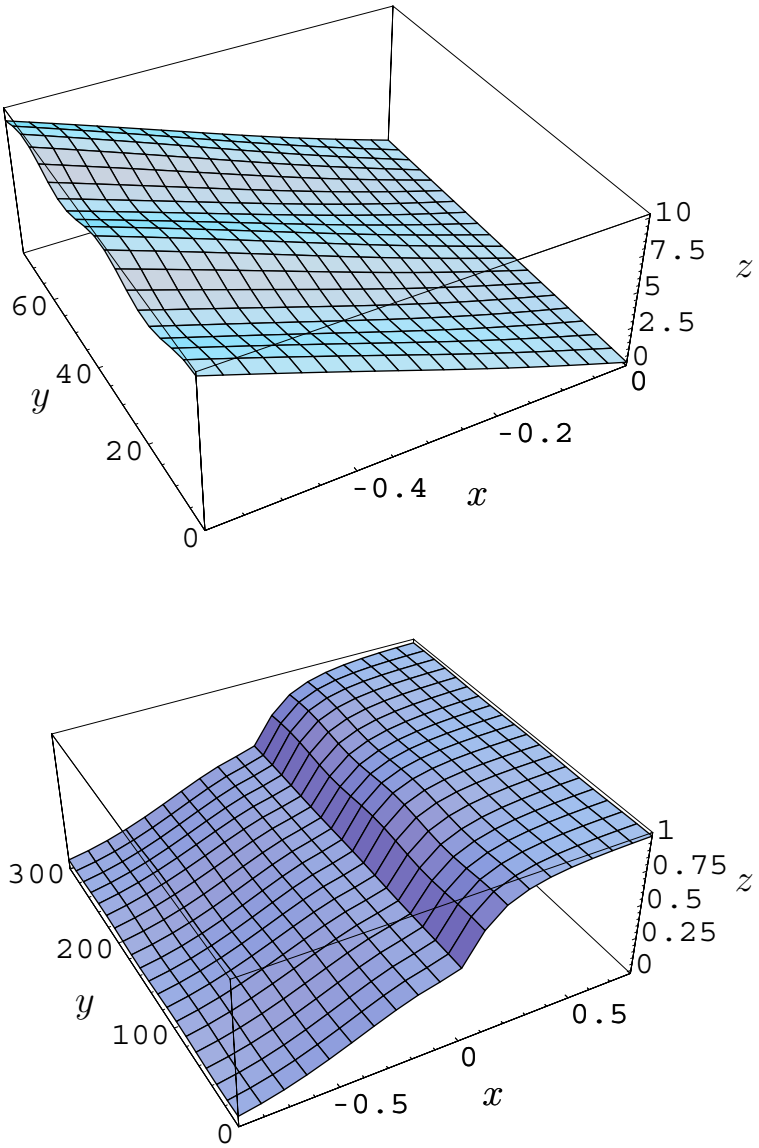

Figure 3.2: Perturbed front profile for the vortex and antivortex density field. The fronts propagate in the x direction and has a sinusoidal modulation in the y direction.

even the first term already implies a modulation of the singular line. Indeed, the standard perturbation Ansatz would fail for our problem because of the singular behavior of the front. The usual Ansatz of a stability calculation

$$n^+(\tilde{x}, y, t) = n_0^+(\tilde{x}) + \epsilon(n_1^+ + in_2^+)(\tilde{x})e^{iqy+\omega t+i\Omega t}, \tag{3.43}$$

only works if the unperturbed profiles are smooth enough and not vanishing in a semi-infinite region. If we impose on our corrected linear stability analysis the conditions

$$\frac{n_1^+ + in_2^+}{n_0^+} \quad \text{bounded} \quad \text{and} \quad \frac{n_1^- + in_2^-}{n_0^-} \quad \text{bounded}, \tag{3.44}$$

then as $\varepsilon \to 0$ the perturbations can be considered small everywhere, while we allow for a modulation of the singular line [74].

We next linearize the equations (3.38) around the uniformly translating solution according to (3.41-3.42). We obtain a set of four linearized ODE's for the variables D_1, D_2, S_1, S_2, which correspond, respectively, to the real and imaginary parts of the difference and sum variables introduced in (3.32). These equations, which are reported in the Appendix, depend also on the unperturbed profiles D_0, S_0, which are known from the derivation in Section 3.2.1. Moreover, there is an explicit dependence on the parameters q, ω, Ω.

In order to analyse the stability of the front of vortices and antivortices, the dispersion relation $\omega(q), \Omega(q)$ must be derived. This can be determined with a shooting method: for every wavenumber q there is a unique value of the growth rate ω and frequency Ω which satisfies the boundary conditions related to the perturbed front. If the growth rate is positive, a small perturbation will grow in time, thus leading to an instability.

3.3.3 The shooting method

The singularity of the front makes the numerical integration difficult to handle, as in the case of the planar front. In view of the relations (3.44), the

boundary conditions

$$n_1^+ = 0, \qquad n_2^+ = 0,$$

have to be imposed for $\zeta = 0$. These yield the boundary conditions for the variables D_1, S_1, D_2, S_2

$$S_1 = -D_1, \qquad S_2 = -D_2. \tag{3.45}$$

Moreover, by substituting these boundary conditions and the relations (3.27) for the unperturbed fields in the linearized equations for D_1, D_2, S_1, S_2, the following relations can be derived for ζ vanishing from the left

$$\left.\frac{dD_1}{d\zeta}\right|_{0^-} = \omega + qkD_2(0), \tag{3.46}$$

$$\left.\frac{dD_2}{d\zeta}\right|_{0^-} = \Omega - qkD_1(0) - 2qk\left.\frac{dD_0}{d\zeta}\right|_{0^-}. \tag{3.47}$$

Since the jump in the derivative of the n^+ field is equal to the jump in the derivative of the n^- field, the relations above for the derivatives of D_1 and D_2 are continuous at $\zeta = 0$. The derivatives related to S_1 and S_2 have a jump, however. An explicit expression for the derivative of the sum of the real and imaginary part of the perturbations S_1, S_2 can also be derived from the equations reported in the Appendix. In particular, these have the following generic form

$$\frac{dS_1(\zeta)}{d\zeta} = \frac{\mathcal{N}_1(\zeta)}{\mathcal{D}_1(\zeta)}, \qquad \frac{dS_2}{d\zeta} = \frac{\mathcal{N}_2(\zeta)}{\mathcal{D}_2(\zeta)}, \tag{3.48}$$

which is similar in structure to Eqs. (3.35): $\mathcal{N}_1, \mathcal{D}_1, \mathcal{N}_2, \mathcal{D}_2$ depend on ζ through the set of functions

$$\left(D_0, S_0, \frac{dD_0}{d\zeta}, \frac{dS_0}{d\zeta}, D_1, S_1, \frac{dD_1}{d\zeta}, D_2, S_2, \frac{dD_2}{d\zeta}\right),$$

and on the parameters q, ω, Ω.

The equations (3.48) are not defined at the singular point. By substituting the boundary conditions given by (3.45-3.47), both the numerators $\mathcal{N}_1, \mathcal{N}_2$ and the denominators $\mathcal{D}_1, \mathcal{D}_2$ vanish. Again, as with (3.35), we encounter the problem of dealing with the singularity at $\zeta = 0$. This difficulty

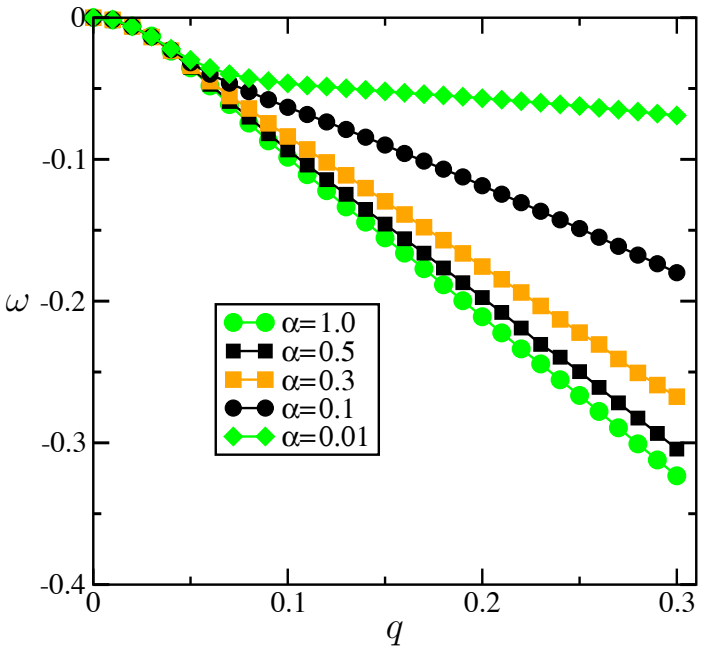

Figure 3.3: Dispersion relation $\omega(q)$ for different values of anisotropy coefficient α and a velocity $v = 1.0$.

can be overcome in the same way as in Section 3.2.2 for the derivation of the planar front profile. In particular, we can not start the integration at the singular point, but we have to start the backwards integration at some small distance on the left of $\zeta = 0$. We do so by first obtaining the derivatives of the fields S_1 and S_2 analytically through the expansion of the equations (3.48) around the critical point. In the limit $\zeta \to 0$, this yields the following self-consistency condition for the derivatives,

$$\left.\frac{dS_1}{d\zeta}\right|_{0^-} = \frac{\mathcal{N}_1'|_{0^-}}{\mathcal{D}_1'|_{0^-}}, \qquad \left.\frac{dS_2}{d\zeta}\right|_{0^-} = \frac{\mathcal{N}_2'|_{0^-}}{\mathcal{D}_2'|_{0^-}}, \tag{3.49}$$

where $\mathcal{N}_1', \mathcal{N}_2', \mathcal{D}_1', \mathcal{D}_2'$ denote the derivatives of the corresponding functions evaluated at the singular point. Once these are solved and used in the numerics, the integration can be carried out smoothly. Because of the singularity at the point $\zeta = 0$, the derivative of the perturbed fields are not continuous there and a relationship for the discontinuity in the derivatives can be de-

rived as was the case for the unperturbed fields. In particular the expression (3.21) is generalized for the perturbed field. This implies that the derivative of the total magnetic field is again continuous even at the singularity.

From the equations for the perturbed fields given in the Appendix, the boundary conditions at $\zeta = -L$ can be derived. Just like the unperturbed field for the antivortex density vanishes on the left with a Gaussian behavior according to (3.19), also the perturbations n_1^- and n_2^- vanish as a Gaussian, i.e. faster then an exponential.

Moreover, since the density of vortices increases linearly asymptotically, we can retain in the equations only terms which are proportional to the density of vortices n_0^+. From this we get the following equation for the density of the perturbation $\delta n^+ = n_1^+ + i n_2^+$ for $\zeta \ll -1$

$$\frac{d^2\delta n^+}{d^2\zeta} + 2iqk\frac{d\delta n^+}{d\zeta} - pq^2\delta n^+ = pq^2\frac{dn_0^+}{d\zeta}. \tag{3.50}$$

The solutions of this equation which do not diverge are of the form

$$\delta n^+ = -\frac{dn_0^+}{d\zeta} + Ce^{\lambda\zeta}, \;\; \lambda = iqk + \sqrt{(q^2(p-k^2))}, \tag{3.51}$$

where C is an arbitrary constant and k and p represent the coefficients of anisotropy defined in (3.39). Thus, the perturbations decay on the left of the sample with a decay length ζ, such that

$$\frac{1}{\zeta} = q\sqrt{p-k^2}. \tag{3.52}$$

Note that the decay length becomes very large for small q; this type of behavior is of course found generically in diffusion limited growth models. Technically it means that we need to be careful to take large enough systems to study the small-q behavior. From the numerical integration it was verified that Eqs. (3.51) and (3.52) describe correctly the behavior of δn^+ at large distance.

Furthermore, since vortices are absent in the positive region, we have to impose that the density of the perturbation related to the n^+ field, and its derivative in space, have to vanish there. Similarly we get a second ODE

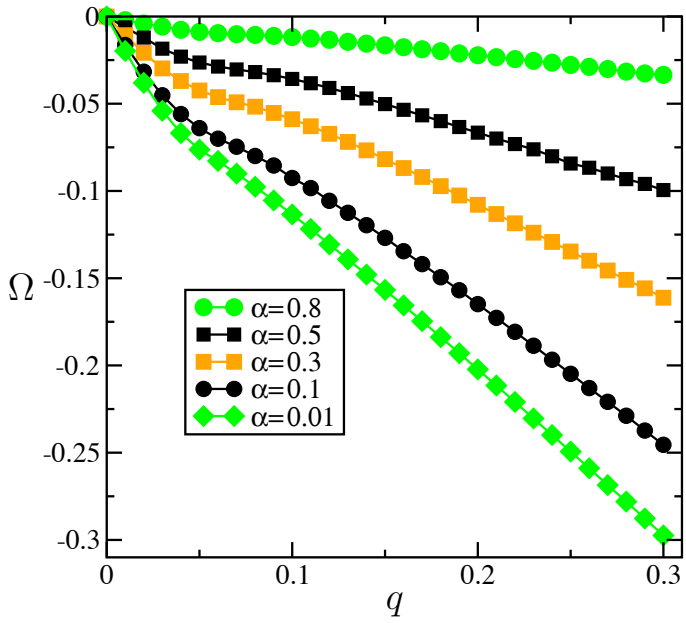

Figure 3.4: Imaginary part of the growth rate $\Omega(q)$ for different values of the anisotropy coefficient α, with velocity $v = 1.0$.

with constant coefficients by considering that the density of antivortices is constant at large positive distances. For $\zeta \gg 1$

$$\frac{d^2\delta n^-}{d^2\zeta} + (v + 2iqk)\frac{d\delta n^-}{d\zeta} - (pq^2 + \omega + i\Omega)\delta n^- = 0. \tag{3.53}$$

In order to satisfy the boundary condition, we must consider the solution which vanishes exponentially. The solution of this equation which does not diverge is of the form

$$\delta n^- = C_1 e^{\bar{\lambda}\zeta} \ , Re(\bar{\lambda}) < 0. \tag{3.54}$$

We applied the shooting method in a 4-dimensional space defined by the free parameters $D_1(0), D_2(0), \omega$ and Ω, by integrating backward in the interval $[-L, 0]$ and then in $[0, +\infty[$, looking for solutions of the type (3.51,3.54).

By matching the solutions to the boundary conditions

$$\begin{array}{ll} \lim_{\zeta\to -L} n_1^+ = -\dfrac{dn_0^+}{d\zeta}. & \lim_{\zeta\to -L} n_2^+ = 0, \\ \lim_{\zeta\to +\infty} n_1^- = 0, & \lim_{\zeta\to +\infty} n_2^- = 0, \end{array} \tag{3.55}$$

we then obtain a unique dispersion relation for the real part of the growth rate $\omega(q)$.

3.3.4 Results

Fig. 3.3 represents the dispersion relation for an angle $\theta = \pi/4$ and different coefficients of anisotropy α. The front is always stable, even in the presence of very strong anisotropy, for very low values of α. As the anisotropic coefficient α is lowered from above, for fixed wavenumber q, the growth rate $\omega(q)$ increases, but it is always negative. For small q a quadratic behavior of $\omega(q)$ is found

$$\omega \approx cq^2, \;\; q \ll 1, \tag{3.56}$$

where the (negative) coefficient c depends on the anisotropy of the sample. In Fig. 3.4 we have plotted the frequency Ω as a function of the wavenumber q. One observes from (3.40) that Ω/q is the velocity with which the perturbation of the front shifts along the direction transverse to the propagation direction. The behavior of $\Omega(q)$ is linear for low wavenumber q and is proportional to the non-diagonal element of the mobility tensor k,

$$\Omega(q) \propto kq, \;\; q \ll 1. \tag{3.57}$$

For an anisotropy coefficient equal to one the isotropic case is recovered and then $\Omega(q)$ vanishes identically for all wavenumbers.

As we have already mentioned, the equations that we have used are valid at scales larger than the cutoff represented by the penetration depth. Anyway, since our results clearly show a stability in the large q behavior, our model provides a good description for the dynamics of the front.

In Fig. 3.5 we plot the growth rate ω as a function of q^2 for different values

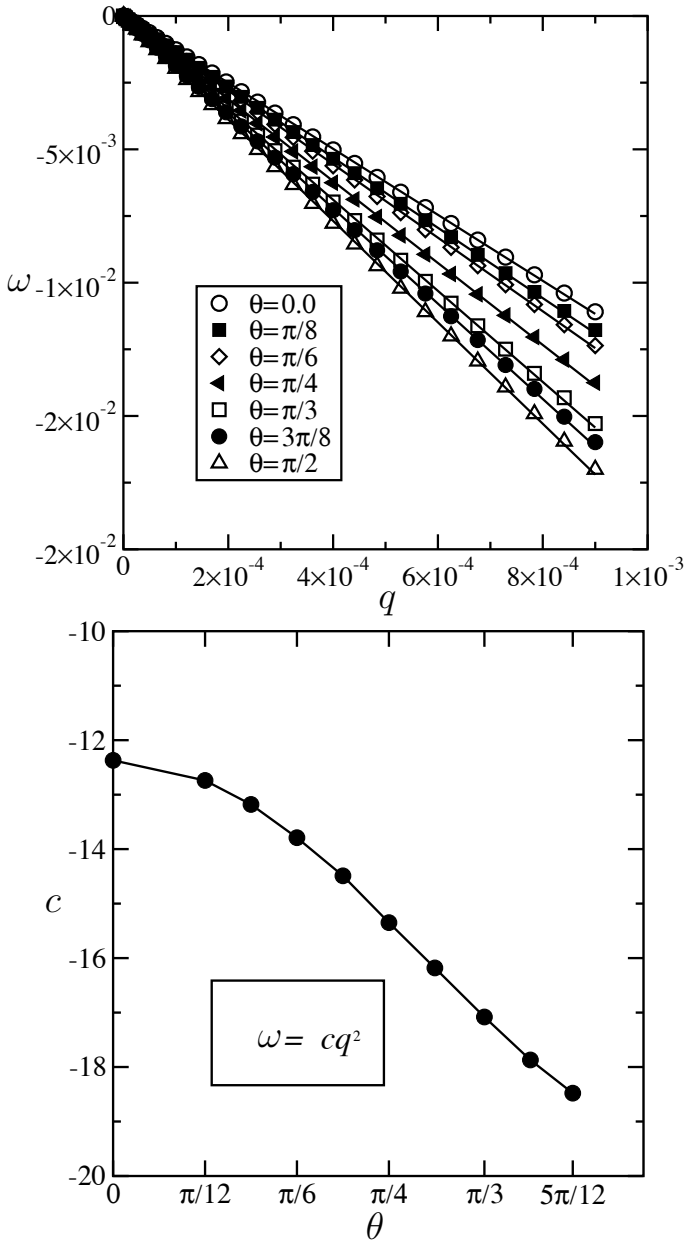

Figure 3.5: (a) Plot of $\omega(q^2)$ as a function of the angle θ. (b) For a coefficient of anisotropy $\alpha = 0.8$ and a velocity $v = 1.0$, the results from linear regression for the slope evaluated at $q = 0$, $c = d\omega/d(q^2)$, are plotted as a function of θ.

of the angle θ. Linear regression then gives a slope corresponding to the constant c in (3.56), which is half the second derivative of the growth rate ω with respect the wavenumber at $q = 0$. The dependence of c as a function of the angle θ is shown in the lower plot. As the angle θ increases, the front becomes more and more stable. This behavior can be understood directly from the form of the equations. By applying the transformation

$$\theta \to \frac{\pi}{2} - \theta, \;\; 0 < \theta < \pi/4, \tag{3.58}$$

the elements of the mobility tensor transform into

$$p \to \frac{1}{p}, \quad k \to \frac{k}{p}. \tag{3.59}$$

By considering the quadratic relation of $\omega(q)$ for small q and the fact that the equations are invariant under the transformations $\tilde{q} = pq$ and (3.59), it is easy to derive

$$\omega(q)|_\theta = p^2 \omega(q)|_{\pi/2-\theta}, \;\; 0 < p < 1, \tag{3.60}$$

which proves that the dispersion relation becomes more negative as θ increases. When the direction of propagation is that of the fast growth direction the isotropic case is recovered. In Fig. 3.6 we show the dependence of the coefficient c as a function of the velocity of the front. The front is stable for velocities for which n_0^+ vanishes linearly ($v \geq 1/4$). Furthermore the front becomes more stable with increasing v. As one can easily understand from the form of the unperturbed front, the vortex density profile becomes steeper with increasing the velocity. The limit of infinitely large v corresponds to the case of a front of vortices propagating in the absence of antivortices. Thus, the results confirm the stability of the front without an opposing flux of antivortices.

3.4 Stationary front

We will analyse here also the case of a stationary front, with $v = 0$. In this case it is easy to derive the unperturbed profiles for the densities of

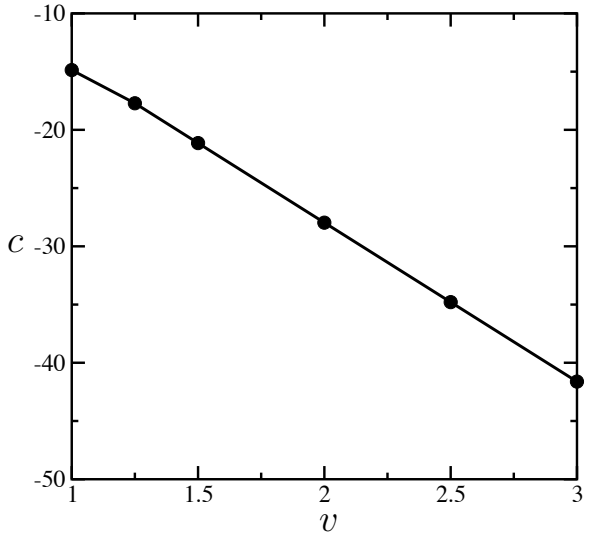

Figure 3.6: Velocity dependence of half the second derivative of $\omega(q)$ with respect to q evaluated at $q = 0$. As the velocity increases the front becomes more and more stable.

vortices and antivortices, since they are continuous and do not present any singularities. This case was previously studied in ([27]) and treated in terms of a sharp interface limit. Equations (3.14,3.15) in this case simplify to

$$\frac{d}{d\tilde{x}} n_0^+ \frac{d}{d\tilde{x}}(n_0^+ - n_0^-) - n_0^+ n_0^- = 0, \tag{3.61}$$

$$\frac{d}{d\tilde{x}} n_0^- \frac{d}{d\tilde{x}}(n_0^- - n_0^+) - n_0^+ n_0^- = 0. \tag{3.62}$$

The profiles of vortices and antivortices are symmetric in this case, and outside the interfacial zone the density fields can be easily derived analytically. By neglecting the annihilation term, the profiles of vortices and antivortices have a dependence on the coordinate $\tilde{x}$ of the type

$$n_0^{\pm} = \sqrt{N^2 \mp 2C(\tilde{x} \pm \tilde{x}_1)}, \tag{3.63}$$

where $]-\tilde{x}_1, \tilde{x}_1[$ denotes the region where vortices and antivortices overlap, N is the density at $(\pm\tilde{x}_1)$ and C a constant. The density of vortices and

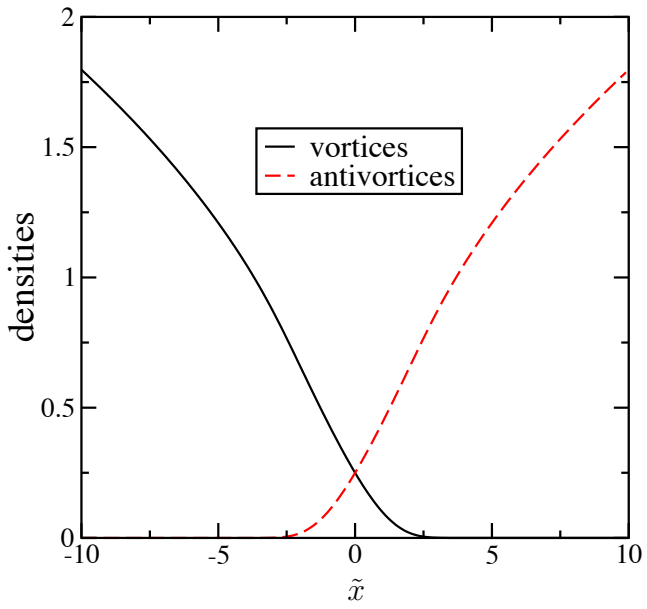

Figure 3.7: Density profiles for vortices and antivortices in the stationary case ($v = 0$). The profiles are smooth and are not characterised by singularities, as was the case for fronts propagating with finite velocity.

antivortices decays with a Gaussian tail, as can easily be calculated from equations (3.61 and 3.62). For Eq. (3.61), by considering that n_0^+ assumes a Gaussian-like dependence, and from the form of (3.63), we get the following equation

$$-\frac{dn_0^+}{d\tilde{x}}\frac{dn_0^-}{d\tilde{x}} = n_0^+ n_0^- . \tag{3.64}$$

This yields in a self-consistent way a Gaussian behavior for n^+

$$n_0^+ \approx Ae^{-\tilde{x}^2 - \tilde{x}(N^2/C - 2\tilde{x}_1)}, \tag{3.65}$$

where A is a constant. The stability of the front was studied by following a similar procedure as for the moving front. Because of the regular profiles, the Ansatz (3.40) that we have applied for the case of a finite velocity is not required. Thus the linear stability analysis can be carried out in the standard way and the linearised equations for the perturbation can easily be integrated. We do not explain here the procedure in detail, since it is a

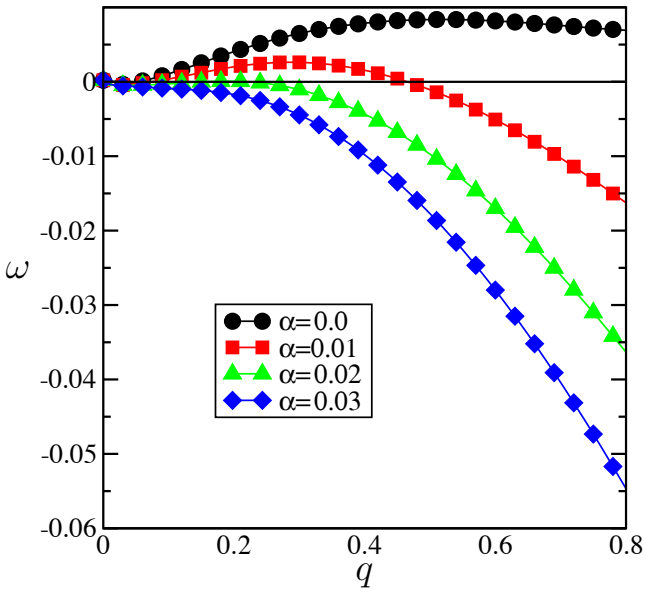

Figure 3.8: Dispersion relation $\omega(q)$ in the case of a stationary front. An instability is found for a critical anisotropy coefficient $\alpha_c \approx 0.02$.

simplified version of the one discussed in the previous section. As Fig. 3.8 shows, an instability is found below a critical coefficient of anisotropy $\alpha_c \approx 0.02$. These results confirm previous approximate calculations [27], but, as we have already underlined, this coefficient would correspond to an extremely high in-plane anisotropy which is not found in any type of superconducting material [63–65]. Typical values for the in-plane anisotropy of YBCO are for example $1/\alpha_c \approx 1.15$, while the inverse of the critical coefficient that we have found is one order of magnitude higher. We conclude that this model of a stationary front in the presence of anisotropy is insufficient to explain the turbulent behavior that has been found experimentally at the flux-antiflux boundary.

3.5 Conclusions

From our analysis it follows that the planar front of vortices moving with a sufficiently large velocity v in a superconducting sample is stable even in the presence of strong in-plane anisotropy. For stationary fronts, on the other hand, our stability analysis is in agreement with the earlier approximate analysis of [27], confirming that such fronts show an instability to a modulated state in the limit of very strong anisotropy. From an experimental point of view, the critical anisotropy of this instability is extremely high when compared with real values that can be found for materials with both tetragonal and orthorhombic structure [63–65], even when a nonlinear current-electric field characteristic is considered [28]. From a theoretical point of view, the behavior in the limit of small but finite v is still open as we have not investigated the range $0 < v < 1/4$ where the profiles have a noninteger power law singularity. It could be that the instability gradually becomes suppressed as v increases from zero, or it could be that the limit $v \to 0$ is singular, and that moving fronts are stable for any nonzero v. Only further study can answer this question.

Our calculations differ markedly from previous work in that we focus on moving fronts from the start, where our results follow from a straightforward application of linear stability analysis to our model. Taken together, these results lead to the conclusion that a model which includes a realistic in-plane anisotropy, but which neglects the coupling with the temperature, cannot explain the formation of an instability at a vortex-antivortex boundary for sufficiently large front velocities. At the same time, our calculations show that the issue of the stability of vortex fronts is surprisingly subtle and rich. For example, we note the fact that for any front velocity, the value n_0^- at the singular line is exactly $n_\infty/2$ for any v. One question is whether this is simply a mathematical curiosity or if the absence of instabilities is related to this unexpected feature through the boundary conditions at infinity. Moreover, we have not investigated if the presence of a gradient in the antivortex distribution far ahead of the front could generate a long-wavelength

front instability. These are all still open issues, so clearly it is difficult to make general statements about the (transient) stability of such fronts in less idealized situations.

One possible interpretation of the results is that when one has a finite slab into which vortices penetrate from one side, and antivortices from the other side, a stationary modulated front (annihilation zone) forms in the middle for extremely large anisotropies. However, a moving front never has a true Mullins-Sekerka type instability, since a protrusion of the front into the region of antivortices is always damped as a result of the increased annihilation.

The fact that the "turbulent" behavior at the interface between vortices of opposite sign was found in a temperature window [24], suggests that the coupling with the local temperature in the sample could be important. It appears that it is necessary to include both the heat transport and dissipation in the model. In analogy with the finger-like patterns that we have analysed in the Chapter 2 of this thesis, the local over-heating of the sample could play a role. The question is why the instability is observed only at the boundaries between vortices and antivortices and does not affect the vortices behind the front. On the other hand, to our knowledge, this type of turbulent behavior has been observed specifically for a sample of $YBa_2Cu_3O_{7-x}$ with an in-plane anisotropy and not for other type of materials. This suggests a possible explanation of the unstable behavior at the interface in terms of the combined effect of the in-plane anisotropy together with the local temperature variations in the sample. Applying an appropriate stability analysis to an extended model that takes into account this coupling is clearly an important issue for the future.

Chapter 4

Concluding remarks

In this thesis we have described and analysed some out-of-equilibrium patterns in type II superconductors. The main issue on which this work focused was the propagation of fronts separating two different coexisting phases. We explored in particular the dynamics of an interface between the intermediate and the superconducting state as a first example (Chapter 2), and the dynamics of an interface between flux of opposite sign as a second case (Chapter 3).

The central theme of this thesis is the *collective behavior* of vortices and their final distribution into domains whose shape is not trivially dependent on the material inhomogeneities, but determined extrinsically by an instability. We have seen that flux penetration can occur through the development of vortex domains, which have a well defined shape and propagate very rapidly. A first question that arises towards the understanding of this pattern formation is which physical factors play a fundamental role in the development of these phenomena. Moreover, a second issue is the study of the pattern features, like the shape and the characteristic size.

An important characteristic of systems of vortices is that they are *dissipative*: as we have described in Chapter 1, vortex motion is always accompanied by dissipation, due to the normal nature of the cores. The heat released because of the coupling between the induced electro-magnetic field and the

currents certainly has dramatic effect on the stability of the material. A temperature increment continues to grow if the amount of heat that is generated in this process can not be transfered to the substrate with a fast enough rate. Since, expecially in the creep regime, the dynamics of vortices is driven by a thermal activation over the pinning barriers, as a consequence of the overheating, a large amount of flux penetrates, leading to avalanches. In this thesis we have underlined the importance of this interplay on the selection of the pattern shape and of the dynamics of the front. While in the Chapter 2 we have strengthened these ideas by proposing a model with a self-organized finger-like domains dependent on the temperature distribution, in Chapter 3 we have pointed out the limitation of a model that does not include this dependence.

Beside the relevance of the temperature for the dynamics of vortices, a fundamental characteristic for their collective behavior is that, contrary to the particles of other pattern-forming systems, they do not attract but *repel* each other. This has an immediate consequence for the properties of a finite-size domain of vortices, since the absence of a stabilizing factor like the surface tension e.g. at the interface between a solid and a liquid makes the study of the final pattern selection non-conventional.

On the other hand, in Chapter 3 we have considered a system of vortices of opposite sign that attract each other and annihilate by dissipating the core energy.

In both examples of vortex front dynamics that we have investigated, we have adopted a *coarse-grained* picture for the magnetic flux distribution, in which we have neglected the finite core size and the non-local relations ignored by the London approximation. A more accurate analysis beyond this cutoff scale, would be provided by the Ginzburg-Landau equations. For the first case of propagating front (Chapter 2), this macroscopic continuum description implies a picture with a domain of constant density of magnetic flux and a sharp transition zone at the interface with the superconducting state. In the second case (Chapter 3), instead, the continuity involves a

singularly vanishing front at the boundaries with vortices and antivortices. This approach, however, is justified in both cases since it does not affect the *relevant* dynamics of the front. In the first case we are interested indeed in the contour dynamics of the domain of vortices, for which a one-dimensional description is quite appropriate, as we have seen, whereas in the second one we concentrate on the long-wavelength behavior of the front and the interface dynamics is not affected by the singularity.

4.1 Finger-like patterns.

In Chapter 2 we have studied finger-like domains of vortices in Nb thin films and investigated their characteristic shape and width. We have proposed and built a novel-type of model for the front dynamics based on a *boundary-layer approximation*. This approach, which has extensively been used for other pattern-forming systems to describe phenomena like dendrites at the solid-liquid interface or viscous fingering, had never been used for systems of vortices. Even if our formulation has some limitations, like e.g. the neglected non-locality of the current response or long-ranges forces, it captures, however, the essence of the phenomenon and provides a proof for the well-defined shape of finger-like patterns. In our model, by supporting the theory of a thermo-magnetic instability, we suggested the picture of propagating fingers with a self-organized shape, with a relatively higher mobility and velocity at the tip and a lower mobility and velocity on the side. A higher speed leads to an enhanced mobility and therefore more heat is generated. From our analysis we could estimate the fingers width and its dependence on the substrate temperature. In order to understand more complex structures than the flux filaments with finger-like shape, the long-range interactions between current ribbons at the edge of the domain should be included. Moreover, to study dendritic patterns one should take into account also inhomogeneities. As supported by previous numerical simulations, indeed, flux filaments can split and evolve into patterns with a branched-like morphology when they

encounter a defect.

In Chapter 2 we could determine the finger-like contour of shape-preserving vortex domains. However, as we have already pointed out, the solutions that we have found belong to a continuous family. An open question is whether and how a unique solution, that corresponds to a determined value of the velocity, is selected. In some pattern-forming system, like in the case of dendrites in crystal growth, the velocity is uniquely selected and determined by solving the problem of stability in the presence of a surface tension type term, but in other pattern forming systems (like front propagation), a unique solution is dynamically selected [34]. Because of the absence of a surface tension at the interface, the problem of the stability of vortex fronts is quite subtle. However, one useful way of examining the stability of the finger-like patterns is studying the contour dynamics of the domain of vortices by using the system of partial differential equations, defined in (2.10) and (2.11). In the frame of our local growth model, as we have seen, the dynamics of the front can be described in terms of the arclength s, the curvature $\kappa(s)$ and the angle $\theta(s)$ between the normal direction $\hat{n}$ and a fixed direction $\hat{z}$. Although an exhaustive study of the vortex finger dynamics is beyond the scope of this thesis, we would like to present here the first preliminary results of such studies.

4.1.1 Contour dynamics

The contour dynamics of a domain of vortices can be studied by starting from an initial shape for the domain of vortices, and using the following system of equations (4.1),

$$\begin{aligned}
\frac{\partial\theta}{\partial t} &= -\frac{1}{s_T}\frac{\partial v_{\mathrm{n}}(\theta)}{\partial\sigma} - s_T\kappa(\sigma)\left(\int_0^\sigma \kappa v_{\mathrm{n}}(\theta)\,d\sigma' - \sigma\int_0^1 \kappa v_{\mathrm{n}}(\theta)\,d\sigma'\right), \\
\frac{\partial s_T}{\partial t} &= s_T\int_0^1 \kappa v_{\mathrm{n}}(\theta)\,d\sigma,
\end{aligned} \tag{4.1}$$

where s_T is the total arclength of the curve and σ the parametrisation. The equations above describe the interface evolution in a geometrical model like

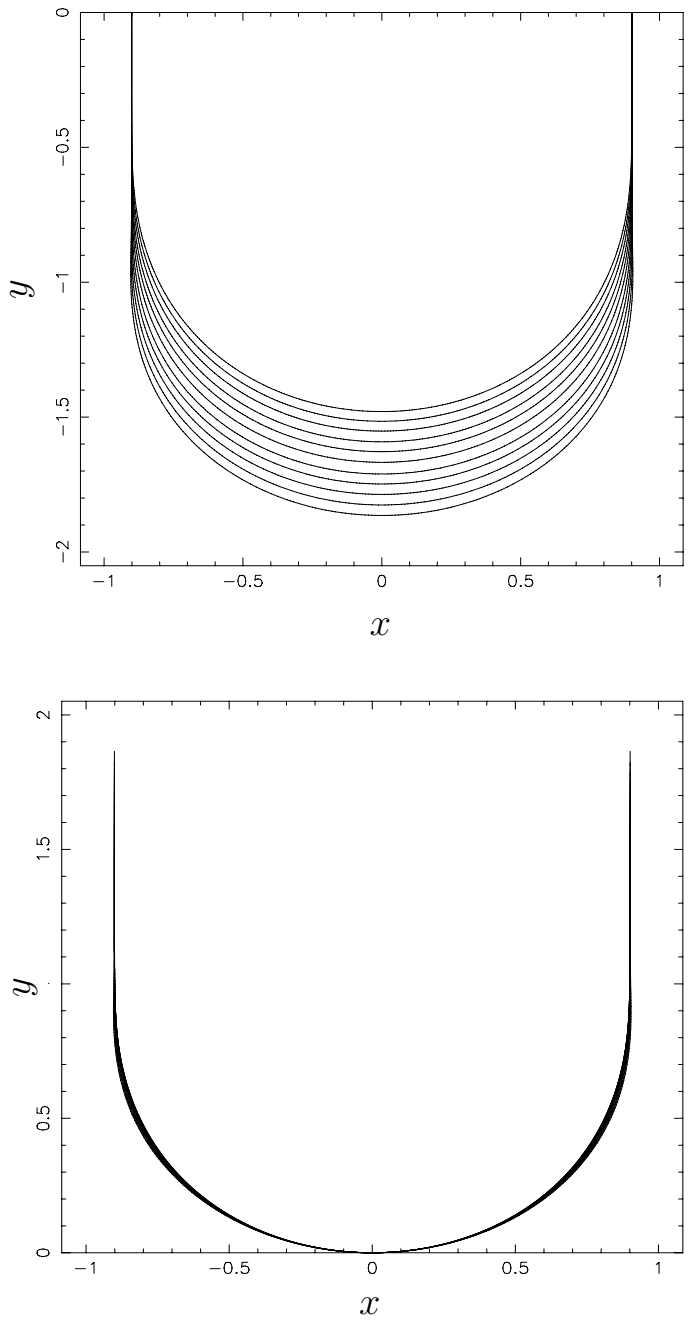

Figure 4.1: In the image above: countour dynamics of the finger-shape domain of vortices for a time $t = 0.2$ in our units, for $v_0 = 1.04$ and $\alpha = 7.0$. In the plot below the finger shapes of the domain at different time have been superposed.

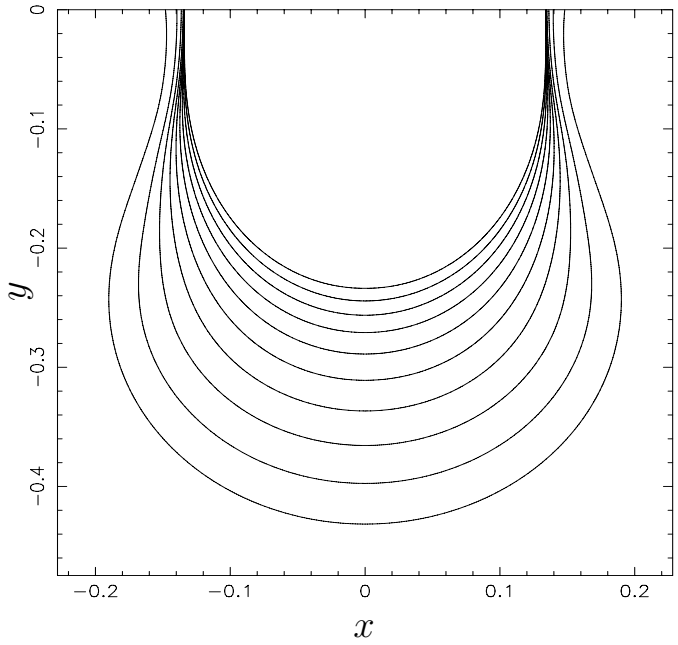

Figure 4.2: Contour dynamics of the domain for $\alpha = 50.0$ and $v_0 = 1.4$ after a time $t = 0.08$.

the one that we have considered in Chapter 2; the derivation of such equations can be found in [59, 60]. In addition, one has to couple the equations above with the ones introduced in Chapter 2 for the normal velocity of the interface and the time derivative of the heat content, (2.10) and (2.11).

4.1.2 Preliminary results of the simulations

We have performed some numerical simulations and directly solved the system of (4.1) together with (2.10) and (2.11), to study the evolution of the solutions found in Chapter 2. We discretised the arclength of the curve with a finite numbers of points parametrised by $\sigma_i = 1/n$, $i = 1, n$ and we integrated the equations by employing a Runge-Kutta routine with an stepsize control [61]. Figure 4.1 illustrates the dynamics of the domain contour for a Stekly parameter defined in (1.66) $\alpha = 7.0$ and for a velocity $v = 1.04$ in the

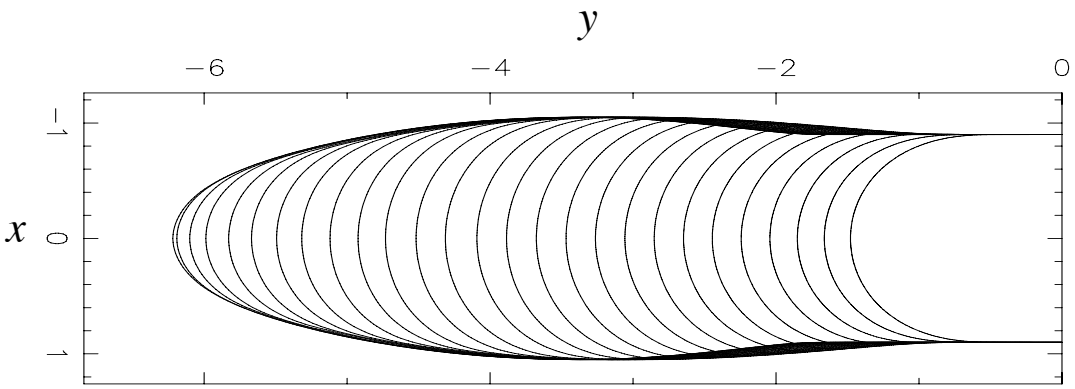

Figure 4.3: Contour dynamics of the domain for the same parameters as in Fig 4.1, after a time $t = 2.6$.

dimensionless coordinates of Chapter 2, for the smooth $f(j, T)$ characteristic. As one can observe from the superposed curves related to the contour at different time (although there is a slight evolution halfway between the tip and the sides), the domain maintains the same shape for a time interval $t \lesssim 0.2$. This confirms that the finger-like patterns which we have determined in Chapter 2 are indeed shape-preserving.

As we have already stressed previously, besides the problem of determining the shape-preserving growth forms, an other issue for the complete understanding of these patterns is the stability of the solutions. The solutions that we have found are shape-preserving, but we have not investigated which ones are stable among the continuous family, parametrised e.g. by the velocity v_0 of the tip. While Fig. 4.1 illustrates that some solutions are stable for short times, Fig. 4.2 shows that the domain contour for an initial different configuration can become unstable and evolve into other shapes. This image represents the contour dynamics of the fingers for a parameter $\alpha = 50.0$ and a tip velocity $v_0 = 1.4$. The different curves reproduce the shape of the pattern at different time and consecutive configurations differ for a time step $\Delta t = 0.01$. As one can observe from e.g. the space interval Δy at the tip between two consecutive configurations, the velocity with which the pattern

propagate increases rapidly. Fig. 4.3 also shows that the initial finger-like shape of Fig. 4.1 can evolve into a different structure.

In analogy with the case of dendrites in crystal growth, we encounter in our analysis the problem of the velocity selection. However, as we have underlined, this issue turns to be quite subtle for the case of vortex patterns. The examples that we have just described from the first results of our numerical simulations, show that the scenario of the vortex domain dynamics can be quite rich and that it requires a deeper study for a complete understanding of the front stability. The use of numerical simulations is only the first step towards such an analysis.

As we have discussed while describing the experiments on vortex-patterns in Chapter 1, the domain shapes can change, depending on the temperature of the sample, and the structure becomes more complex. Therefore an other issue for a future study is whether the finger shape could indeed converge to such forms, like dendrites with branch-like structures. The analysis of the time evolution of the contour in the sharp interface approximation could be also useful for possible future investigations about these different morphologies.

4.2 Stability of a vortex-antivortex front

In Chapter 3 we have analyzed the stability of an interface between vortices of opposite sign. The aim of our investigation was to understand the mechanism that leads to the unstable "turbulent" behavior observed at the boundaries of a $YBa_2Cu_3O_{7-\delta}$ crystal. In particular we examined whether such an instability originates from the in-plane anisotropy of the sample, in analogy with the Kelvin-Helmholtz effect between to adjacent layers of fluids. An in-plane anisotropy, indeed, generates in fact a shear between the two regions of flux of opposite sign, due to a velocity component along the interface. From our analysis it has emerged that an instability is never observed for a moving vortex-front, if the coupling with the temperature in not taken into account.

Even though our analysis is based on the limit for a linear current-voltage characteristic, it could be extended to the case with a highly nonlinear relation. In the case with a symmetric stationary interface, instead, we have found an instability for extremely high coefficients of in-plane anisotropy, confirming previous analysis. However, the critical anisotropy coefficient, has a value much too high when compared with experimental measurements for an $YBa_2Cu_3O_{7-\delta}$ sample. We conclude therefore that only a model that takes in account the coupling of the temperature, including a dissipative term and a temperature-dependent viscosity in the flux flow regime, could capture the essence of the instability.

Appendix

We introduce here the function $F(\theta, \kappa, \zeta)$ that follows from the calculations of 2.3.1 and enters in the system of equations for the sharp current-electric field relation,

$$
\begin{aligned}
F(\theta,\kappa,\zeta) = &-\frac{4(4+v_0^2\cos^2\theta)^{3/2}}{v_0\tau\sin\theta}(8+v_0^2+v_0^2\cos(2\theta))^{-1} \\
&\Big(2\tau^{-1}(1-j)+2v_0\cos\theta-\sqrt{2(8+v_0^2+v_0^2\cos(2\theta))}\Big)^{-1} \\
&\Bigg\{\frac{\tau}{(4+v_0^2\cos^2\theta)^{3/2}}\Bigg[v_0\Bigg(v_0^3\cos^4\theta-v_0^2\cos^3\theta \\
&\Big(\tau^{-1}(j-1)+\sqrt{4+v_0^2\cos^2\theta}\Big)-v_0\Bigg(8+(\sqrt{2}\tau)^{-1}(j-1) \\
&\sqrt{(8+v_0^2+v_0^2\cos(2\theta))}\Bigg)\sin^2\theta-v_0\cos^2\theta(-4+v_0^2\sin^2\theta) \\
&-\cos\theta\Bigg(4\Big(\tau^{-1}(j-1)+\sqrt{4+v_0^2\cos^2\theta}\Big) \\
&+v_0^2\Big(\tau^{-1}(1-j)+\sqrt{4+v_0^2\cos^2\theta}\Big)\sin^2\theta\Bigg)\Bigg)\kappa^2\Bigg] \\
&+\alpha v_0\tau\cos\theta j+j-1-v_0\tau\cos\theta-\frac{1}{2}(1-j+\tau v_0\cos\theta) \\
&\Big(v_0\cos\theta+\sqrt{4+v_0^2\cos^2\theta}\Big)(v\cos\theta+\kappa) \\
&+v_0\sin\theta\left(\tau v_0\kappa\sin\theta-\frac{v_0(1-j+v_0\tau\cos\theta)\kappa(s)\sin\theta}{\sqrt{4+v_0^2\cos^2\theta}}\right)\Bigg\}.
\end{aligned}
$$

Appendix

For the function $F_1(\theta, \kappa, \zeta)$ in (2.42), for the smooth current-electric field relation we get,

$$
\begin{aligned}
F_1(\theta,\kappa,\zeta) = \Bigg\{ & v_0 \Bigg[\frac{\tau \exp\left(\frac{\tau v_0 \cos\theta}{j_1}\right)}{\exp\left(\frac{\tau v_0 \cos\theta}{j_1}\right) - 1} \Bigg[\kappa^2 \Bigg(- \cos\theta - v_0 \sin^2\theta \\
& + \left(\frac{\tau}{j_1 \left(\exp\left(\frac{\tau v_0 \cos\theta}{j_1}\right) - 1 \right)} + \frac{2}{\sqrt{4 + v_0^2 \cos^2\theta}} \right) \Bigg) \Bigg] \\
& + 2v_0 \Big(\frac{\sin^2\theta}{4 + v_0^2 \cos^2\theta} \Big) \kappa^2 \left[1 - j + j_1 \ln \left(\exp\left(\frac{\tau v_0 \cos\theta}{j_1}\right) - 1 \right) \right] \\
& - (4 + v_0^2 \cos\theta^2)^{-3/2} \left[j - 1 - j_1 \ln \left(\exp\left(\frac{\tau v_0 \cos\theta}{j_1}\right) - 1 \right) \right] \\
& \Big(v_0^2 \cos^3\theta - v_0 \sqrt{4 + v_0^2 \cos^2\theta} \sin^2\theta + \cos\theta (4 + v_0^2 \sin^2\theta) \Big) \kappa^2 \Bigg] \\
& + \alpha j \tau v_0 \cos\theta - 1 + j - j_1 \ln \left(\exp\left(\frac{\tau v_0 \cos\theta}{j_1}\right) - 1 \right) \\
& - \frac{1}{2} \Big(v_0 \cos\theta + \sqrt{4 + v_0^2 \cos^2\theta} \Big) (v_0 \cos\theta + \kappa) + \Big[1 - j \\
& + j_1 \ln \left(\exp\left(\frac{\tau v_0 \cos\theta}{j_1}\right) - 1 \right) \Big] + \frac{\tau \exp\left(\frac{\tau v_0 \cos\theta}{j_1}\right) v_0^2 \kappa \sin^2\theta}{1 - \exp\left(\frac{\tau v_0 \cos\theta}{j_1}\right)} \\
& - \frac{v_0^2 \kappa \Big(1 - j + j_1 \ln \left(\exp\left(\frac{\tau v_0 \cos\theta}{j_1}\right) - 1 \right) \Big) \sin^2\theta}{\sqrt{4 + v_0^2 \cos^2\theta}} \Bigg\} \Bigg\{ v_0 \sin\theta \\
& \left(\frac{\tau \exp\left(\frac{\tau v_0 \cos\theta}{j_1}\right)}{\left(\exp\left(\frac{\tau v_0 \cos\theta}{j_1}\right) - 1 \right)} + \frac{\left(j - 1 - j_1 \ln \left(\exp\left(\frac{\tau v_0 \cos\theta}{j_1}\right) - 1 \right) \right)}{\sqrt{4 + v_0^2 \cos^2\theta}} \right) \Bigg\}^{-1}.
\end{aligned}
$$

Appendix

From the linear stability analysis of the vortex-antivortex front in Chapter 3, we get the linearized equations for the variables D and S,

$$\omega\left(D_1+\frac{dD_0}{d\zeta}\right)-\Omega D_2+pq^2S_0\left(D_1+\frac{dD_0}{d\zeta}\right)= \\ +v\frac{dD_1}{d\zeta}+\left(\frac{dS_0}{d\zeta}\right)\left(\frac{dD_1}{d\zeta}\right)+\left(\frac{dD_0}{d\zeta}\right)\left(\frac{dS_1}{d\zeta}\right) \\ +S_0\frac{d^2D_1}{d\zeta^2}+S_1\frac{d^2D_0}{d\zeta^2}-qk\left[2S_0\frac{dD_2}{d\zeta}+\frac{dS_0}{d\zeta}D_2+\frac{dD_0}{d\zeta}S_2\right],$$

$$\omega D_2+\Omega\left(D_1+\frac{dD_0}{d\zeta}\right)+pq^2S_0D_2= \\ +v\frac{dD_2}{d\zeta}+\left(\frac{dS_0}{d\zeta}\right)\left(\frac{dD_2}{d\zeta}\right)+\left(\frac{dD_0}{d\zeta}\right)\left(\frac{dS_2}{d\zeta}\right) \\ +S_0\frac{d^2D_2}{d\zeta^2}+S_2\frac{d^2D_0}{d\zeta^2}+qk\left[2S_0\left(\frac{dD_1}{d\zeta}+\frac{d^2D_0}{d\zeta^2}\right)\right. \\ \left.+\frac{dS_0}{d\zeta}\left(D_1+\frac{dD_0}{d\zeta}\right)+\frac{dD_0}{d\zeta}\left(S_1+\frac{dS_0}{d\zeta}\right)\right],$$

$$\omega\left(S_1+\frac{dS_0}{d\zeta}\right)-\Omega S_2+pq^2D_0\left(D_1+\frac{dD_0}{d\zeta}\right)= \\ +v\frac{dS_1}{d\zeta}+2\left(\frac{dD_0}{d\zeta}\right)\left(\frac{dD_1}{d\zeta}\right)+D_0\frac{d^2D_1}{d\zeta^2} \\ +D_1\frac{d^2D_0}{d\zeta^2}-qk\left[2D_0\frac{dD_2}{d\zeta}+2\frac{dD_0}{d\zeta}D_2\right]-S_0S_1+D_0D_1,$$

$$\omega S_2+\Omega\left(S_1+\frac{dS_0}{d\zeta}\right)+pq^2D_0D_2= \\ +v\frac{dS_2}{d\zeta}+2\left(\frac{dD_0}{d\zeta}\right)\left(\frac{dD_2}{d\zeta}\right)+D_0\frac{d^2D_2}{d\zeta^2}+D_2\frac{d^2D_0}{d\zeta^2} \\ +qk\left[2D_0\left(\frac{dD_1}{d\zeta}+\frac{d^2D_0}{d^2\zeta}\right)+2\frac{dD_0}{d\zeta}\left(D_1+\frac{dD_0}{d\zeta}\right)\right]-S_0S_2+D_0D_2.$$

Appendix

Bibliography

[1] W. Meissner and R. Ochsenfeld, *Naturwissenshaften* **21**, 787 (1933).

[2] A. A. Abrikosov, *Soviet. Phys.* JETP **5**, 1174 (1957).

[3] G. Blatter and V. B. Geshkenbein, *Vortex matter*, *The physics of Superconductors*, vol. 1, pp. 726-936, eds. K. H. Bennemann and K. Emerson (Springer, Berlin, 2003).

[4] G. Blatter, M. V. Feigel'man, V. B. Geshkenbein, A. I. Larkin and V. M. Vinokur, Rev. Mod. Phys. **66**, 1125 (1994).

[5] M. Tinkham, *Introduction to superconductivity* (McGraw-Hill international editions, 1996).

[6] P. G. De Gennes, *Superconductivity of Metals and Alloys* (Addison-Wesley, Reading, Massachussets, 1966/1989).

[7] C. P. Bean, Rev. Mod. Phys. **36**, 31 (1964).

[8] A. Gurevich and R. G. Mints, Rev. Mod. Phys. **59**, 941 (1987).

[9] G. R. Mints and A. L. Rakhmanov, Rev. Mod. Phys. **53**, 551 (1981).

[10] C. A. Duran, P. L. Gammel, R. E. Miller, and D. J. Bishop, Phys. Rev. B **52**, 75 (1995).

[11] T. H. Johansen, M. Baziljevich, D. V. Shantsev, P. E. Goa, Y. M. Galperin, W. N. Kang, H. J. Kim, E. M. Choi, M.-S. Kim, S. I. Lee, Europhys. Lett. **59**, 599 (2002).

[12] F. L. Barkov, D. V. Shantsev, T. H. Johansen, P. E. Goa, W. N. Kang, H. J. Kim, E. M. Choi and S.I. Lee, Phys. Rev. B **67**, 064513 (2003).

[13] M. S. Welling, R. J. Westerwaal, W. Lohstroh, R. J. Wijngaarden, Physica C **411**, 11 (2004).

[14] M. S. Welling, *Vortex landscapes: manipulation, avalanches and roughening*, Ph.D. thesis (2004).

[15] M. Menghini, R. J. Wijngaarden, A. V. Silhanek, S. Raedts and V. V. Moshchalkov, Phys. Rev. B **71**, 104506, (2005).

[16] P. Leiderer, J. Boneberg, P. Brüll, V. Bujok and S. Herminghaus, Phys. Rev. Lett. **71**, 2646 (1993).

[17] M. Marchevsky, L. A. Gurevich, P. H. Kes, and J. Aarts, Phys. Rev. Lett. **75**, 2400 (1995).

[18] M. V. Marchevsky, *Magnetic decoration study of the vortex lattice in superconductors*, Ph.D. thesis (1997).

[19] I. Aranson, A. Gurevich, and V. Vinokur, Phys. Rev. Lett. **87**, 067003 (2001).

[20] I. Aranson, A. Gurevich, M. S. Welling, R. J. Wijngaarden, V. K. Vlasko-Vlasov, V. Vinokur, U. Welp, Phys. Rev. Lett. **94**, 037002 (2004).

[21] A. L. Rakhmanov, D. V. Shantsev, Y. M. Galperin, T. H. Johansen, Phys. Rev. B **70**, 224502 (2004).

[22] T. Frello, M. Baziljevich, T. H. Johansen, N. H. Andersen, Th. Wolf, and M. R. Koblischka, Phys. Rev B **59** (1999).

[23] M. V. Indebom, H. Kronmüller, P. Kes and A. A. Menovsky, Physica C **209**, 259 (1993).

[24] M. R. Koblischka, T. H. Johansen, M. Baziljevich, H. Hauglin, H. Bratsberg and B. Y.Shapiro, Europhys. Lett. **41**, 419 (1998).

[25] V. K. Vlasko-Vlasov, V. I. Nikitenko, A. A. Polyanskii, G. V. Crabtree, U. Welp and B. W. Veal, Physica C **222**, 361 (1994).

[26] F. Bass, B. Ya. Shapiro, and M. Shvartser, Phys. Rev. Lett **80**, 2441 (1998).

[27] L. M. Fisher, P. E. Goa, M. Baziljevich, T. H. Johansen, A. L. Rakhmanov and V. A. Yampol'skii, Phys. Rev. Lett. **87**, 247005 (2001).

[28] A. L. Rakhmanov, L. M. Fisher, A. A. Levchenko, V. A. Yampol'skii, M. Baziljevich, and T. H. Johansen, JETP Letters **76**, 291 (2002).

[29] W. W. Mullins and R. F. Sekerka, J. Appl. Phys. **34**, 323 (1963).

[30] A. Dorsey and O. Martin, Phys. Rev. A **35**, 3989 (1987).

[31] D. A. Kessler, J. Koplik, H. Levine, Adv. Phys. **37**, 255 (1998); E.A. Brener, V. I. Mel'nikov, Adv. Phys. **40**, 53 (1991).

[32] V. L. Ginzburg, and L. D. Landau, Zh. Eksp. Teor. Fiz. **20**, 1064 (1950).

[33] M. Cross and P. C. Hohenberg, Rev. Mod. Phys. **65**, 851 (1993).

[34] W. van Saarloos, *Front propagation into unstable states*, Phys. Rep. **386**, 29-222 (2003).

[35] J. C. Osborn and A. T. Dorsey, Phys. Rev. B **50**, 961 (1994).

[36] H. Frahm, S. Ullah, and A. T. Dorsey, Phys. Rev. Lett. **66**, 3067 (1991).

[37] A. Dolgert, T. Blum, A. T. Dorsey, and M. Fowler, Phys. Rev. B, **57**, 5432 (1998).

[38] F. Liu, M. Mondello, and N. Goldenfeld, Phys. Rev. Lett. **66**, 3071 (1991).

[39] I. Aranson, B. Ya. Shapiro, and V. Vinokur, Phys. Rev. Lett. **76**, 142 (1996).

[40] J. Bardeen, L. N. Cooper, and R. J. Schrieffer, Phys. Rev. **108**, 1175 (1957).

[41] L. P. Gor'kov and N. B. Kopnin, Usp. Fiz. Nauk **116**, 413 (1975).

[42] F. and H. London, Proc. Roy. Soc. (London) **A19**, 71 (1935).

[43] F. London, *Superfluids*, vol. I, Wiley, New York, 152 (1950).

[44] W. H. Kleiner, L. M. Roth, and S. H. Autler, Phys. Rev. **133**, A1226 (1964).

[45] K. Huang, *Statistical Mechanics*, Wiley, New York (1987-2004).

[46] R. Surdeanu, R. J. Wijngaarden, E. Visser, J. M. Huijbregtse, J. Rector, B. Dam and R. Griessen, Phys. Rev. Lett. **83**, 2054 (1999).

[47] J. Pearl, Appl. Phys. Lett. **5**, 65 (1964).

[48] J. R. Clem, Phys. Rev. B **43**, 7837 (1991).

[49] J. S. Rowlinson and B. Widom, *Molecular theory of capillarity*, Oxford University Press, New York (1984).

[50] J. Bardeen and M. J. Stephen, Phys. Rev. **140**, A1197 (1965).

[51] Y. B. Kim, C. F. Hempstead, and A. R. Strnad, Phys. Rev. Lett. **9**, 306 (1962).

[52] P. W. Anderson, Phys. Rev. Lett. **9**, 309 (1962).

[53] A. M. Cambpell and J. E. Evetts, Adv. Phys. **21**, 199 (1972).

[54] C. M. Bender, S. A. Orszag, Advanced Mathematical Methods for Scientists and Engineers, McGraw-Hill, New York (1978).

[55] W. van Saarloos, Phys. Rep. **301**, 9 (1998).

[56] E. Ben-Jacob, N. Goldenfeld, J. S. Langer and G. Schön, Phys. Rev. A **29**, 330 (1984).

[57] U. Ebert, W. van Saarloos and C. Caroli, Phys. Rev. Lett. **77**, 4178 (1996).

[58] A. T. Dorsey, R. E. Goldstein, Phys. Rev. B **57**, 3058 (1998).

[59] R. C. Brower, D. A. Kessler, J. K. Koplik and H. Levine, Phys. Rev. A **29**, 1335 (1984).

[60] D. A. Kessler, J. Koplik and H. Levine, Phys. Rev. A **30**, 3161 (1984).

[61] W. H. Press, S. A. Teukolsky, W. T. Vetterling, B. P. Flannery and M. Metcalf, *Numerical Recipes in Fortran 90*, Cambridge University Press (1986/1996).

[62] A. Soibel, E. Zeldov, M. Rappaport, Y. Myasoedov., T. Tamegai, S. Ooi, M. Konczykowsky and V. B. Geshkenbein, Nature **406**, 282 (2000).

[63] G. J. Dolan, F. Holtzberg, C. Feild, and T. R. Dinger, Phys. Rev. Lett. **62**, 2184 (1989).

[64] K. Zhang, D. A. Bonn, S. Kamal, R. Liang, D. J. Baar, W. N. Hardy, D. Basov, and T. Timusk, Phys. Rev. Lett. **73**, 2484 (1994).

[65] C. A. Murray, P. L. Gammel, D. J. Bishop, D. B. Mitzi and A. Kapitulnik, Phys. Rev. Lett. **64**, 2312 (1990).

[66] P. G. Drazin and W. H. Reid, *Hydrodynamic stability*, Cambridge University Press, Cambridge (1981).

[67] A. Gurevich, Phys. Rev. B, **46**, 3638 (1991).

[68] A. Gurevich, Phys. Rev. Lett. **65**, 3197 (1990).

[69] J. Bear, *Dynamics of Fluids in Porous Media* (Elsevier, New York, 1972).

[70] L. A. Peletier, in *Application of Nonlinear Analysis in the Physical Sciences*, H. Amman, N. Bazley and K. Kirchgaessner, eds. (Pitman, London, 1981).

[71] The similarity between the nonlinear diffusion equation of vortices and the porous medium equation was pointed out in particular by J. Gilchrist and C. J. van den Beek, Physica C **231**, 147 (1994).

[72] V. M. Vinokur, M. V. Feigel'man and V. B. Geshkenbein, Phys. Rev. Lett. **67** 915 (1991); H. G. Schnack and R. Griessen, Phys. Rev. Lett. **68** 2706 (1992); V. M. Vinokur and V.B. Geshkenbein, Phys. Rev. Lett. **68** 2707 (1992).

[73] I. Golding, Y. Kozlovsky, I. Cohen, and E. Ben-Jacob, Physica **260**, 510 (1998).

[74] J. Müller and W. van Saarloos, Phys. Rev. E **65**, 061111 (2002).

[75] In the nomenclature of G. I. Barenblatt, *Similarity, Self-Similarity and Intermediate Asymptotics* (Consultants Bureau, New York, 1979), this corresponds to a transition from self-similarity of the first kind to self-similarity of the second kind as a function of the front velocity.

Samenvatting

In dit proefschrift beschrijven en analyseren we enige niet-evenwichtspatronen in type-II supergeleiders. Dit werk richt zich in hoofdzaak op de voortplanting van fronten die de scheiding vormen tussen twee verschillende, coëxisterende fasen. We onderzoeken in het bijzonder de dynamica van een grensvlak tussen de gemengde en de supergeleidende toestand als eerste voorbeeld (hoofdstuk 2) en de dynamica van een grensvlak tussen supergeleidende flux van tegengesteld teken als tweede geval (hoofdstuk 3).

Het hoofdthema van dit proefschrift is het collectieve gedrag van vortices en hun uiteindelijke verdeling over domeinen. De vorm van deze domeinen hangt niet op een simpele manier af van oneffenheden in het materiaal, maar wordt van buitenaf bepaald door een instabiliteit. We zien dat het indringen van flux kan plaatsvinden door het ontstaan van domeinen met vortices, die een duidelijk bepaalde vorm hebben en zich zeer snel voortplanten. Een eerste vraag die opkomt met betrekking tot deze patroonvorming is welke fysische factoren een fundamentele rol spelen in het optreden van deze verschijnselen. Een tweede onderwerp is bovendien het bestuderen van de eigenschappen van deze patronen, zoals de vorm en de karakteristieke grootte.

Een belangrijke eigenschap van systemen van vortices is dat ze dissipatief zijn. Zoals beschreven in hoofdstuk 1, gaat beweging van vortices altijd gepaard met dissipatie, doordat het binnenste van de vortices niet supergeleidend is. De warmte die vrijkomt door de koppeling tussen het geïnduceerde elektromagnetische veld en de stromen heeft dramatische gevolgen voor de stabiliteit van het materiaal. Een verhoging van de temperatuur

blijft doorgroeien als de door dit proces opgewekte warmte niet snel genoeg kan worden afgevoerd naar het substraat. Met name als er sprake is van *creep* wordt de dynamica van de vortices bepaald door thermische activering over de pinning-barrière heen. Zodoende kan door oververhitting een grote hoeveelheid flux in het materiaal doordringen, wat tot "flux-lawines" leidt. In dit proefschrift onderstrepen we de invloed van deze wisselwerking op de selectie van de vorm van de patronen en op de dynamica van het front. In hoofdstuk 2 onderbouwen we dit idee door een model voor te stellen met zelfgeorganiseerde vingervormige domeinen, die afhangen van de temperatuurverdeling. In hoofdstuk 3 benadrukken we juist de beperkingen van een model dat deze afhankelijkheid niet bevat.

Naast het belang van de temperatuur voor de dynamica van de vortices is een belangrijke eigenschap voor hun collectieve gedrag dat ze — in tegenstelling tot de deeltjes van andere patroonvormende systemen — elkaar niet aantrekken maar afstoten. Dit heeft direct gevolgen voor de eigenschappen van een vortexdomein van eindige grootte, omdat de afwezigheid van een stabiliserende factor (zoals bijvoorbeeld de oppervlaktespanning tussen een vloeistof en een vaste stof) een onconventionele beschouwing van de selectie van het uiteindelijke patroon noodzakelijk maakt. Aan de andere kant beschouwen we in hoofdstuk 3 een systeem van vortices met tegengesteld teken die elkaar aantrekken en annihileren door de energie van de kernen van de vortices te doen dissiperen.

In beide voorbeelden van de dynamica van vortexfronten die we hebben onderzocht, nemen we een grofkorrelige beschrijving voor de verdeling van de magnetische flux aan, waarin we de eindige afmetingen van de kern van de vortices verwaarlozen, alsmede de niet-lokale afhankelijkheden die in de benadering van London worden verwaarloosd. Een nauwkeuriger beschrijving voorbij deze "cut-off"-schaal zou door de Ginzburg-Landauvergelijkingen worden gegeven. Voor het eerste geval van een bewegend front (hoofdstuk 2) impliceert deze macroscopische continuümbeschrijving het beeld van een domein met constante magnetische fluxdichtheid en een scherpe overgang

aan het grensvlak met de supergeleidende fase. In het tweede geval (hoofdstuk 3) daarentegen, behelst de continuïteit een singulier naar nul afvallend front aan de randen tussen vortices en antivortices. Deze aanpak is echter in beide gevallen gerechtvaardigd omdat deze de *relevante* dynamica van het front niet beïnvloedt. In het eerste geval zijn we namelijk geïnteresserd in de contourdynamica van het vortexdomein, waar een ééndimensionale beschrijving goed voldoet, terwijl we ons in het tweede geval concentreren op het gedrag van het front voor grote golflengte, en de dynamica niet wordt beïnvloed door de singulariteit.

In hoofdstuk 2 beschouwen we vingervormige domeinen van vortices in dunne niobiumlagen en hun karakteristieke vorm en breedte. We construeren een nieuw soort model, gebaseerd op een grenslaag-benadering. Deze aanpak, die uitgebreid toegepast is om andere patroonvormende systemen te beschrijven, zoals dendrieten aan een grensvlak tussen vloeistof en vaste stof of *viscous fingering*, is nog nooit gebruikt voor systemen van vortices. Hoewel onze formulering enige beprekingen heeft, bijvoorbeeld door het verwaarlozen van de niet-lokaliteit van de stroomrespons en van krachten met lange dracht, bevat het wel de essentiële eigenschappen van het verschijnsel en biedt het een bewijs voor de duidelijk bepaalde vorm van de vingerachtige patronen. Door de theorie van een thermo-magnetische instabiliteit te ondersteunen, suggereren we in ons model het beeld van zich voortplantende vingers, met een verhoudingsgewijs hogere snelheid en mobiliteit aan de punt, en lagere snelheid en mobiliteit aan de zijkanten. Een hogere snelheid leidt tot een grotere mobiliteit, zodat meer warmte wordt opgewekt. Uit onze analyse kunnen we de breedte van de vingers schatten, alsmede hoe deze afhangt van de temperatuur van het substraat. Om complexere structuren te begrijpen dan de vingervormige fluxdraden zouden ook de interacties met lange dracht tussen de stroomlinten aan de randen van het domein moeten worden meegenomen. Bovendien zou men om dendritische patronen te bestuderen ook rekening moeten houden met oneffenheden in het materiaal. Zoals door eerdere numerieke simulaties wordt ondersteund, kunnen fluxdraden inder-

daad opsplitsen en zich ontwikkelen tot patronen met vertakte structuren, wanneer zij een defect tegenkomen.

In hoofdstuk 3 analyseren we de stabiliteit van een grensvlak tussen vortices met tegengesteld teken. Het doel van ons onderzoek was om het mechanisme te begrijpen dat leidt tot het instabiele "turbulente" gedrag dat wordt waargenomen aan de randen van een $YBa_2Cu_3O_{7-\delta}$-kristal. In het bijzonder onderzoeken we of zo'n instabiliteit haar oorsprong vindt in de anisotropie in het vlak van het materiaal, analoog aan het Kelvin-Helmholtzeffect tussen twee vloeistoflagen. Een anisotropie in de richting van het vlak genereert inderdaad een afschuifspanning tussen de twee gebieden met tegengestelde flux, vanwege een snelheidscomponent die langs het grensvlak gericht is. Uit onze analyse komt naar voren dat er nooit een instabiliteit wordt waargenomen voor een bewegend vortexfront, wanneer de wisselwerking met de temperatuur niet wordt meegenomen. In het geval van een symmetrisch, stationair grensvlak daarentegen, vinden we een instabiliteit voor extreem hoge waarden van de anisotropie in de richting van het vlak, wat een bevestiging is van eerdere analyses. Echter, de kritische anisotropiecoëfficiënt heeft een veel te hoge waarde in vergelijking met experimentele waarnemingen aan een $YBa_2Cu_3O_{7-\delta}$-laag. We concluderen daarom dat alleen een model dat rekening houdt met de wisselwerking met de temperatuur en een dissipatieve term bevat, alsmede een temperatuurafhankelijke viscositeit in het regime van fluxstroming, de essentie van de instabiliteit kan beschrijven.

Curriculum vitæ

I was born on the 5th January 1978 in Italy in Bassano del Grappa. In this city I attended also the secondary school "Liceo scientifico J. Da Ponte" from 1991 to 1996.

In 1996 I enrolled as an undergraduate student in the course of physics at the University of Padova. In the academic year 2000/2001 I participated to the Erasmus program as an exchange student at the "Imperial College" of London, where I worked on my master thesis under the supervision of of Prof. dr. D. D. Vvedensky. The theme of my project was about stochastic equations of motions for discrete models of epitaxial growth. I graduated in physics cum laude in Padova on the 19th July 2001.

In October 2001 I was employed by FOM (Stichting voor Fundamenteel Onderzoek der Materie) to work in the University of Leiden as a PhD student under the supervision of Prof. dr. ir. W. van Saarloos at the University of Leiden (Netherlands). The theme of my Phd study is the dynamics of vortex fronts in type II superconductors; the main results of my work are described in this thesis.

During the four years of Phd I have attended several meetings and conferences and I have presented my work in Lunteren, Peyresq (France), San Feliu (Spain) and Ischia (Italy). Moreover, I have attended summer schools in Nijmegen and Les Houches (France). From July to October 2004 I have also worked in the group of Prof. R. E. Goldstein in Tucson (Arizona, U.S.). During my time at the University of Leiden I have taught as well as an assistant in the courses of "Quantum theory" and "Statistical Dynamics I".

List of publications

- C. Baggio, R. Vardavas, and D. D. Vvedensky, *Fokker-Planck equation for lattice deposition models*, Phys. Rev. E (Rapid Communications) **64**, 045103 (2001).

- D. D. Vvedensky, C. Baggio, A. Chua, C. Haselwandter, and R. Vardavas, *Stochastic Differential Equations for Driven Lattice Systems*, Contemporary mathematics **330** (2003).

- C. Baggio, M. Howard, and W. van Saarloos, *Dynamics and stability of vortex-antivortex fronts in type II superconductors*, Phys. Rev. E **70**, 026209 (2004).

- A. L.-S. Chua, C. A. Haselwandter, C. Baggio, and D. D. Vvedensky, *Langevin Equations for Fluctuating Surfaces*, accepted in Phys. Rev. E (2005).

- C. Baggio, R. E. Goldstein, A. I. Pesci, and W. van Saarloos, *Boundary layer model for vortex fingers in type II superconductors*, Phys. Rev. B (Rapid Communications) **72**, 060503 (2005).

ITHAKA

As you set out for Ithaka
hope the voyage is a long one,
full of adventure, full of discovery.
Laistrygonians and Cyclops,
angry Poseidon–and don't be afraid of them:
you'll never find things like that on your way
as long as you keep your thoughts raised high,
as long as a rare excitement
stirs your spirit and your body.
Laistrygonians and Cyclops,
wild Poseidon–you won't encounter them
unless you bring them along inside your soul,
unless your soul sets them up in front of you.

Hope the voyage is a long one.
May there be many a summer morning when,
with what pleasure, what joy,
you come into harbors seen for the first time;
may you stop at Phoenician trading stations
to buy fine things
mother of pearl and coral, amber and ebony,
sensual perfume of every kind–
as many sensual perfumes as you can;
and may you visit many Egyptian cities
to gather stores of knowledge from their scholars.

Keep Ithaka always in your mind.
Arriving there is what you are destined for.
But do not hurry the journey at all.
Better if it lasts for years
so you are old by the time you reach the island,
wealthy with all you have gained on the way,
not expecting Ithaka to make you rich.

Ithaka gave you the marvelous journey.
Without her you would not have set out.
She has nothing left to give you now.

And if you find her poor, Ithaka won't have fooled you.
wise as you will have become, so full of experience,
you will have understood by then what these Ithakas mean.

C. P. Cavafy 1911